

**LA-9835-PR**  
**Progress Report**

Los Alamos National Laboratory is operated by the University of California for the United States Department of Energy under contract W-7405-ENG-36.

DEL 87-U-0016

19980309 280

*White Horse Program Review FY 82*

**PLEASE RETURN TO:**

**BMD TECHNICAL INFORMATION CENTER  
BALLISTIC MISSILE DEFENSE ORGANIZATION  
7100 DEFENSE PENTAGON  
WASHINGTON D.C. 20301-7100**

**DIC QUALITY INSPECTED 4**

**Los Alamos** Los Alamos National Laboratory  
Los Alamos, New Mexico 87545

**DISTRIBUTION STATEMENT A**

Approved for public release;  
Distribution Unlimited

LL4024

This work was supported by the US Department of the Army, Ballistic Missile Defense Advanced Technology Center, and the Defense Advanced Research Projects Agency.

Edited by Louise Taylor, AT Division

The views and conclusions contained in this document are those of the author(s) and should not be interpreted as necessarily representing the official policies, either expressed or implied, of the Defense Advanced Research Projects Agency or the US Government.

**DISCLAIMER**

This report was prepared as an account of work sponsored by an agency of the United States Government. Neither the United States Government nor any agency thereof, nor any of their employees, makes any warranty, express or implied, or assumes any legal liability or responsibility for the accuracy, completeness, or usefulness of any information, apparatus, product, or process disclosed, or represents that its use would not infringe privately owned rights. Reference herein to any specific commercial product, process, or service by trade name, trademark, manufacturer, or otherwise, does not necessarily constitute or imply its endorsement, recommendation, or favoring by the United States Government or any agency thereof. The views and opinions of authors expressed herein do not necessarily state or reflect those of the United States Government or any agency thereof.

Accession Number: 4024

Publication Date: Sep 01, 1983

Title: White Horse Program Review FY 82

Personal Author: Dogliani, H.O.; Farrell, J.A.

Corporate Author Or Publisher: Los Alamos National Laboratory, Los Alamos, NM 87545 Report  
Number: LA-9835-PR; UC-28 Report Number Assigned by Contract Monitor: DEL 87-U-0016

Comments on Document: Archive, RRI, DEW.

Descriptors, Keywords: White Horse Accelerator Test Stand Ion Source Circle Aperture Scaling Current  
Radio Frequency Quadrupole Azimuth Asymmetry Beam Dynamics Drift Tube Linac Engineering Slug  
Tuner Fabrication Manifold Data Acqu

Pages: 00137

Cataloged Date: Dec 07, 1992

Document Type: HC

Number of Copies In Library: 000001

Record ID: 25505

Source of Document: DEW

**LA-9835-PR**  
**Progress Report**

**UC-28**  
**Issued: September 1983**

## **White Horse Program Review FY 82**

H. O. Dogliani  
J. A. Farrell

## CONTENTS

ABSTRACT . . . . .	1
EXECUTIVE SUMMARY . . . . .	1
I.    INTRODUCTION . . . . .	1
II.   ACCELERATOR TEST STAND OVERVIEW . . . . .	3
ATS EXPERIMENTAL PROGRAM . . . . .	6
I.    SUMMARY . . . . .	6
II.   HARDWARE DEVELOPMENT . . . . .	6
III.  SOFTWARE DEVELOPMENT . . . . .	11
ION SOURCE AND ATS INJECTOR . . . . .	16
I.    ATS INJECTOR . . . . .	16
II.   CIRCULAR-APERTURE SOURCE DESIGN . . . . .	27
III.  CIRCULAR-APERTURE SOURCE SCALING . . . . .	36
IV.   ION SOURCE TEST STAND . . . . .	37
V.    HIGH-CURRENT TEST STAND . . . . .	42
VI.   CONSIDERATIONS FOR A dc SOURCE . . . . .	47
REFERENCES . . . . .	48
RFQ TUNING . . . . .	50
I.    INTRODUCTION . . . . .	50
II.   RFQ DESIGN PRINCIPLES AND TUNING GOALS . . . . .	50
III.  ERROR ANALYSIS . . . . .	51
A.  The Transmission-Line Model . . . . .	51
B.  Predicting Field Distributions . . . . .	55
IV.   DATA ANALYSIS . . . . .	58
A.  Data Acquisition . . . . .	61
B.  Azimuthal Asymmetry . . . . .	62
V.    THE 2N-PORT NETWORKS . . . . .	66
VI.   ATS RFQ DATA . . . . .	72

VII.	TECHNIQUES FOR IMPROVING LONG RFQ STRUCTURES . . . . .	75
	A. Shorter Structures . . . . .	75
	B. Modified Structures . . . . .	76
VIII.	THE BOTTOM LINE . . . . .	79
RFQ	BEAM DYNAMICS . . . . .	80
	I. INTRODUCTION . . . . .	80
	II. GENERAL PROPERTIES OF THE RFQ . . . . .	81
	III. BEAM-DYNAMICS ANALYSIS AND POLE-TIP DESIGN . . . . .	81
	IV. BEAM-DYNAMICS DESIGN PROCEDURES FOR RFQ SYSTEMS . . . . .	82
	V. RFQ EXPERIMENTAL TEST . . . . .	85
	VI. RFQ DESIGN FOR THE ATS . . . . .	85
	REFERENCES . . . . .	87
DTL	BEAM DYNAMICS . . . . .	89
	I. INTRODUCTION . . . . .	89
	II. DESIGN SUMMARY . . . . .	89
	III. TRANSPORT DESIGN . . . . .	91
	IV. DYNAMICS SIMULATIONS . . . . .	92
	REFERENCES . . . . .	95
ATS	DRIFT-TUBE LINAC ENGINEERING DESIGN CONCEPTS . . . . .	96
	I. INTRODUCTION . . . . .	96
	II. ENGINEERING DESIGN CRITERIA . . . . .	96
	III. PRINCIPAL MECHANICAL FEATURES . . . . .	96
	IV. TANK-DRIFT ASSEMBLY . . . . .	98
	V. DRIFT-TUBE ASSEMBLIES . . . . .	102
	VI. PERMANENT-MAGNET QUADRUPOLES . . . . .	102
	VII. SLUG TUNERS . . . . .	107
	VIII. POST COUPLERS . . . . .	107
	IX. ASSEMBLY, ALIGNMENT, AND HANDLING . . . . .	107
RFQ	DESIGN AND FABRICATION . . . . .	111
	I. BACKGROUND . . . . .	111
	II. DETAIL DESIGN . . . . .	111

III.	FABRICATION . . . . .	115
	A. Vane Fabrication . . . . .	115
	B. Vane-Cavity Cylinder . . . . .	116
	C. The rf Manifold . . . . .	116
	D. C-Seals . . . . .	116
	E. Other Components . . . . .	116
	F. Vane Installation . . . . .	117
IV.	RFQ INSTALLATION ON ATS . . . . .	118
V.	MANIFOLD/VANE-CAVITY INTEGRATION AND TUNING . . . . .	118
THE ACCELERATOR TEST STAND rf SYSTEM . . . . .		119
ATS COMPUTER CONTROL AND DATA ACQUISITION SOFTWARE . . . . .		120
I.	STATUS . . . . .	120
II.	CODE DEVELOPMENT FOR BEAM-DYNAMICS CALCULATIONS . . . . .	121
III.	FORTRAN PROGRAM AND SUBROUTINE SPECIFICATIONS . . . . .	123
IV.	FORTRAN RULES . . . . .	124
	REFERENCES . . . . .	127
ATS DATA BASE AND EDITOR . . . . .		128
ATS THEORETICAL SUPPORT . . . . .		130
I.	ATS RFQ SIMULATION-CODE IMPROVEMENTS . . . . .	130
II.	RESULTS OF SIMULATIONS . . . . .	131
III.	INVERSE-PROBLEM CALCULATIONS . . . . .	131
IV.	FAST RFQ SIMULATION CODE FOR DESIGN WORK . . . . .	132
	REFERENCES . . . . .	132
TECHNOLOGY DEMONSTRATION ACCELERATOR . . . . .		133
GLOSSARY . . . . .		137

## WHITE HORSE PROGRAM REVIEW FY 82

Compiled by

H. O. Dogliani and J. A. Farrell

### ABSTRACT

A review of major achievements in the White Horse Program is provided. Most efforts in FY 82 involved completion of the 2-MeV accelerator test stand culminating in installation of the RFQ, on-line in September 1982. Numerous experiments were conducted, resulting in a significant understanding of beam dynamics and rf structures.

---

### EXECUTIVE SUMMARY

#### I. INTRODUCTION

We will review our accomplishments with ion source development, the accelerator test stand (ATS), radio-frequency quadrupole (RFQ), ATS experiments, and technology demonstration accelerator (TDA) preconceptual design studies. The ATS ion source and injector operates in a reliable manner, allowing quality low-energy beam transport (LEBT) experiments to proceed. We feel that we understand the ion source/injector emittance growths previously observed. Although construction of a dc, high-power ion source test stand (ISTS) was begun, construction was discontinued because of lack of funding. The high-power stand is vital to the development of a dc ion source. Furthermore, circular-aperture studies were initiated to begin scoping for an upgraded LEBT.

A user's manual for the PATH beam-optics code was written, making it easier for our researchers to conduct optics calculations. A preliminary optics design for a complete system was completed and has been used by Lockheed in

its straw-man design contract. Various parametric optical-system performance studies were conducted for various particle types and energies and with realistic emittances. Also, a number of permanent-magnet (PM) optical components were designed and fabricated and are now in use on the ATS. RFQ fabrication, assembly, tuning, and installation in its manifold have resulted in significant structural and electrical understanding. The RFQ's sensitivity of intervane voltages to length was determined resulting in several schemes to control the sensitivity. Numerous mechanical design simplifications were identified and a systematic analytical rf tuning capability resulted.

In anticipation of an operating RFQ, we have completed the LEBT and it is ready for injection of the beam into the RFQ. A considerable effort was expended in developing reliable and often computer-automated diagnostics, leading to a much better experimental description of the beam throughout the LEBT.

It was recognized that a long lead time is necessary for TDA construction and, consequently, a preconceptual design was initiated to scope costs and options, as well as to determine siting requirements. The information obtained from a requirements workshop, in which numerous US Department of Defense (DoD) and contractor representatives participated, was amalgamated with a preliminary 7-yr facility schedule to brief the Los Alamos Construction Projects Review Committee. The briefing went very well and is the precursor for site selection and approval within the US Department of Energy (DOE)--typically a multiyear process. Using the workshop output we began a preconceptual technical design, starting with an RFQ frequency optimization study. As an initial step to costing, a work-breakdown structure (WBS) is being defined.

Managerially, a formalized breakdown structure is implemented to better insure an appropriate level of effort on the various problems on all aspects of White Horse. Considerable energy was expended in developing a workable PERT for the ATS construction but, while useful in focusing resources, the PERT was never fully implemented because of the funding turbulence and consequent numerous redirections. Major internal reviews of the RFQ, drift-tube linac (DTL) design, and TDA have occurred. The exchanges with non-White Horse personnel generated many useful ideas. Non-Los Alamos scientists participated in the TDA requirements workshop; a major review of the ion source as it pertains to White Horse requirements occurred in early July.

## II. ACCELERATOR TEST STAND OVERVIEW

The major emphasis during the first few years of the White Horse Program was on the two ends of the system: a research and development program on high brightness, negative ion source technology and an experimental measurement of the scattering angle introduced during neutralization of the  $H^-$  beam in a gas cell. The neutralization experiments were completely successful.

The next step was to look at the heart of the system, the accelerator. The first studies were computer simulations of DTLs, which indicated that the accelerator requirements could be met if we used a relatively high rf frequency and a high (2- to 3-MeV) injection energy and could provide sufficiently strong quadrupole focusing.

We soon realized that there were few experimental data available on emittance growth in linacs. Existing machines were very similar and were all working injectors for large accelerators. This meant that they were minimally instrumented, and little beam time was available for machine experiments. The data seemed to indicate that the observed emittance growth was greater than that predicted by the simulation codes, but it was not clear whether this was because of inadequacies in the codes or errors in the models of the accelerators built into the codes. Because of these uncertainties, we proposed the construction of an ATS to provide a small, well-instrumented accelerator dedicated to experimental accelerator physics. It was to be a flexible facility for the development of accelerator structures, bunchers, low-energy transport, and matching techniques. The major program for the ATS would be to benchmark the design codes in a regime of brightness and current for which there were no data so that the codes could be used with confidence to design even higher performance systems.

The first conceptual design for the ATS used a DTL with a 250-keV injection energy. The injection energy was far below that required for a practical system and resulted in a current limit of  $\sim 20$  mA, even though we used a  $2\text{-}\beta\lambda$  focusing structure for the linac. The choice of injection energy was based on economic considerations because of the large cost of a Cockroft-Walton accelerator. The low-current limit had the experimental advantage that it would be possible to greatly exceed it with existing ion sources and, therefore, we could study accelerator structures with very high space-charge forces. Accordingly, we designed an injector to provide a beam of 25 to 30 mA at

250 MeV. The final design energy was set at less than 5 MeV to avoid shielding expenses that accompany neutron production. An initial technical event that made an accelerator of this type possible was the development, at Lawrence Berkeley Laboratory and here at Los Alamos, of very high strength, compact, PM quadrupole lenses that could provide the needed focusing strength to overcome the space-charge forces.

The success of the proof-of-principle (POP) RFQ test prompted us to abandon the DTL design because the RFQ offered greatly improved performance in capture efficiency, current, and emittance growth. We arrived at a design capable of accelerating 100 mA at an rms emittance of  $0.02\pi$  cm·mrad with a capture efficiency of 80 to 90% and an emittance growth of 10%. The injection energy was now 100 keV, and the final energy was 2 MeV.

The ATS consists of five components: a 100-mA pulsed ion source that produces a beam with 20-keV energy, an accelerating column to bring the beam energy to 100 keV, a low-energy transport to prepare the beam for the RFQ, the RFQ accelerator, and the DTL accelerator. The system is complete through the RFQ, and we are pursuing an experimental program aimed at developing the tools and techniques for controlling the beam delivered to the RFQ. As expected, this has been difficult because intense, low-energy beams present computational problems not present at higher energies. In addition, the magnet layout in the ATS was optimized for the original DTL experiment, and, while we realized that a redesign would be required, we felt that more data were needed before we could optimize a design. To our dismay, we found that the beam emittance measured at the 20- and 100-keV emittance stations was considerably higher than anticipated. Although we could account for some of this growth as coming from magnet aberrations, obviously there were other sources of emittance growth that we had not considered. The high emittance, combined with the higher current and lower injector energy, resulted in large beam losses along the transport system that made it difficult for us to perform meaningful experiments. Apart from the magnet aberrations, we have now identified two other major sources of emittance growth: space-charge effects from ion source noise and a plasma instability from interaction of the beam with the background gas. With these effects considered, we are able to understand the major problems of the low-energy transport reasonably well and will now be able to modify it to minimize these effects.

The RFQ accelerator also provided a surprise. We assembled the RFQ with a mechanical accuracy well within our anticipated tolerances and found that the sensitivity of its rf tune to vane position was much greater than we had anticipated. This effort was aggravated by a few mechanical errors that had crept into the system. We have studied the problem of tuning long RFQs, using the ATS RFQ, and now believe that we can modify the structure to give it significantly better rf properties. In addition, we have identified simple solutions to the mechanical assembly problems encountered. In spite of its sensitivity, we have tuned the RFQ and installed it on ATS to study its properties, while proceeding with a redesign incorporating some improvements.

## ATS EXPERIMENTAL PROGRAM

### I. SUMMARY

The long-range goal of the ATS experimental program is to understand and control the transverse and longitudinal properties and dynamics of the ATS beam. Our immediate concern is the LEBT between the exit of the column and the entrance of the RFQ. The goals are (1) to understand the beam dynamics sufficiently well so that the LEBT can either be tuned for good transmission, with the correct ellipse parameters at the RFQ, or can be rebuilt to obtain better transmission; (2) to transport sufficient beam to the RFQ, so that its acceleration and transmission properties can be studied; (3) to determine source and LEBT conditions that will result in reproducible beam shapes at the RFQ match point. With these goals in mind, we have directed our efforts toward (1) developing beam-diagnostic hardware for the LEBT and for the output beam of the RFQ, (2) developing the necessary software to drive this hardware and analyze the resulting data, and (3) determining whether the TRACE code can model our LEBT. The TRACE model is being tested by comparing the TRACE emittance predictions with the measurements made on the beamline. These comparisons are helping to determine which input TRACE parameters are important and, perhaps, which are in error.

### II. HARDWARE DEVELOPMENT

Our efforts in this area were concentrated in the construction, installation and shakedown of our LEBT hardware. We now have two "harps" installed in the LEBT and have used them to give us on-line x- and y-profile displays of the beam in a nondestructive manner. The harps have been very useful for quick observations of beam steering and focusing adjustments. We now have three wire scanners that will be used for precision profile measurements and have constructed a 1.65-MeV threshold Faraday cup for use on the RFQ output beam (Fig. 1). An actuator-interlock module, which uses hardwired logic to prevent the collision of actuators in the same beam box, was completed and is now in use. The LEBT was extended to the RFQ match point (Fig. 2).

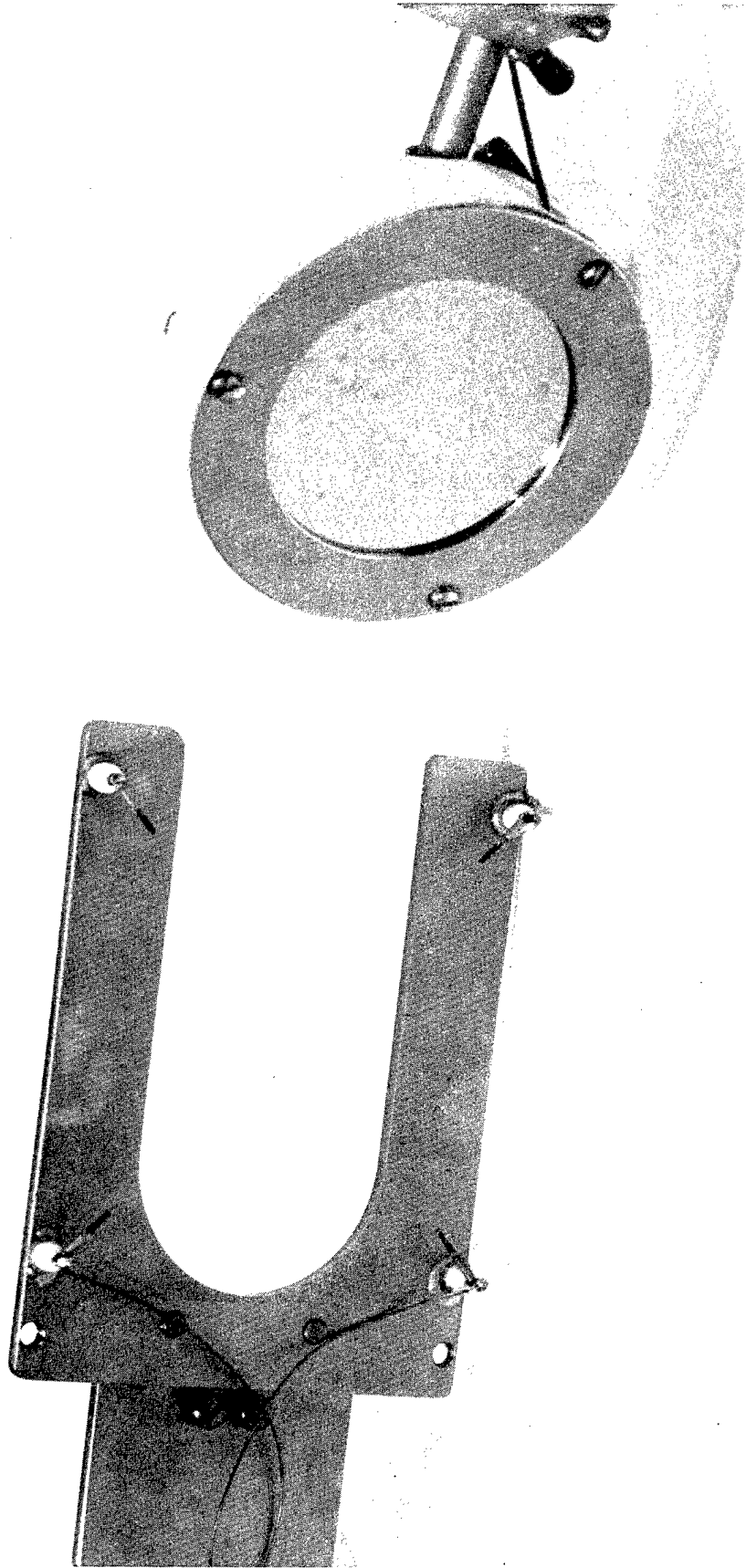


Fig. 1.  
Wire scanner and energy threshold Faraday cup.

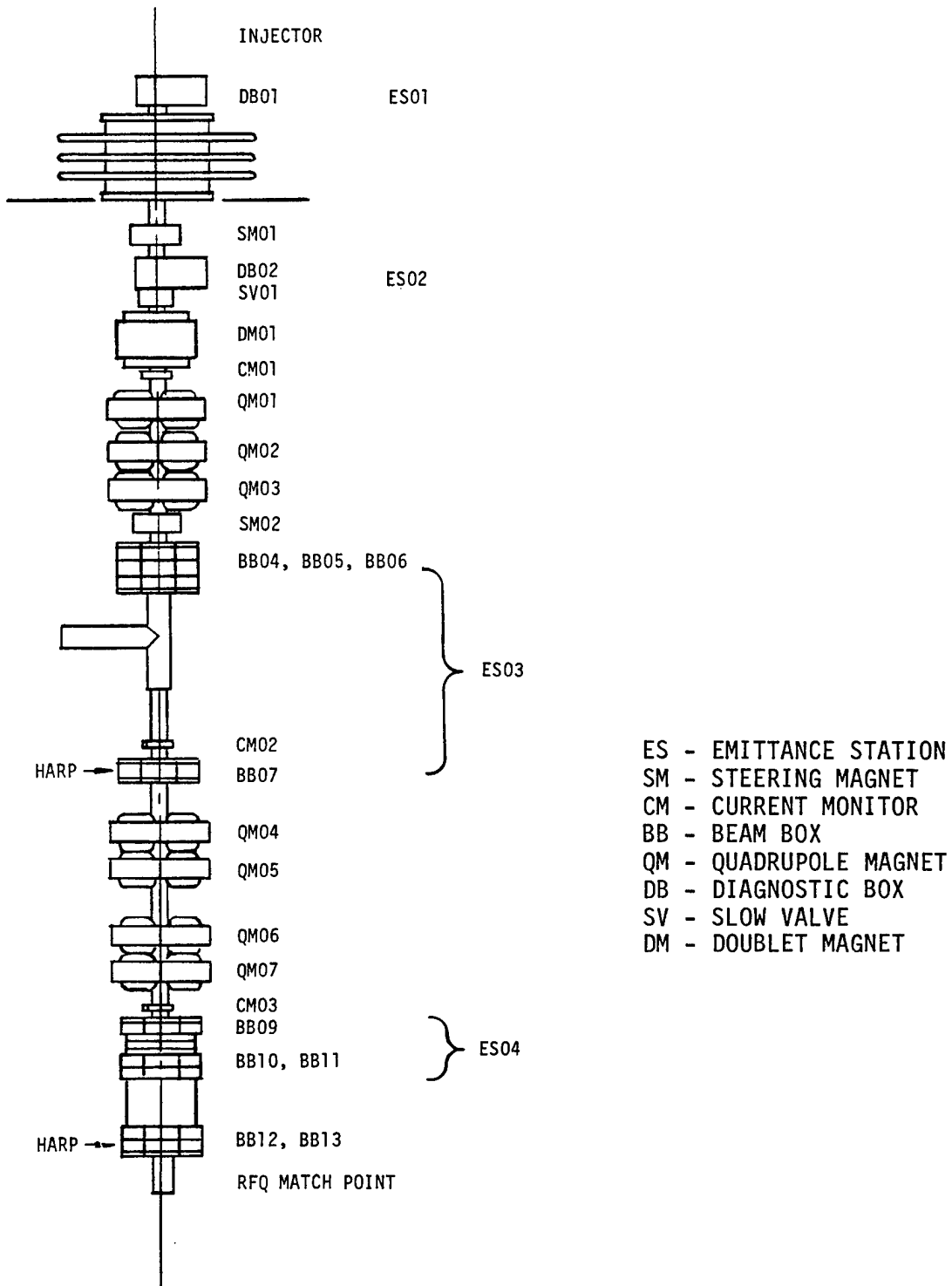


Fig. 2.  
The ATS beamline schematic.

Two stations of slit-and-sandwich collector emittance detectors were built and installed. Figures 3 and 4 show these devices. These devices have a number of advantages. They are rugged; LAMPF uses them at 100 MeV. They are simple in design and have been widely used and tested at other Laboratories. They give a "snapshot" of the beam emittance and, therefore, can be used to observe emittance changes during the beam pulse. They can be used on the output beams of both the RFQ and DTL, limited only by available drift spaces. They can detect neutral  $H^0$  particles. This last feature is necessary for an emittance device using a laser. The device is not without disadvantages. Many amplifiers and analog digital converters (ADCs) are required, each combination having its own overall electronic gain. Changing the angular acceptance requires that we relocate the collector so that the device can require relatively long drift spaces.

New prototype amplifiers for the collectors have been designed and built to replace our limited supplies of borrowed LAMPF amplifiers. The new amplifiers will be simpler in design, will have accessible components, and will allow us to increase our angular sampling from 24 to 48.

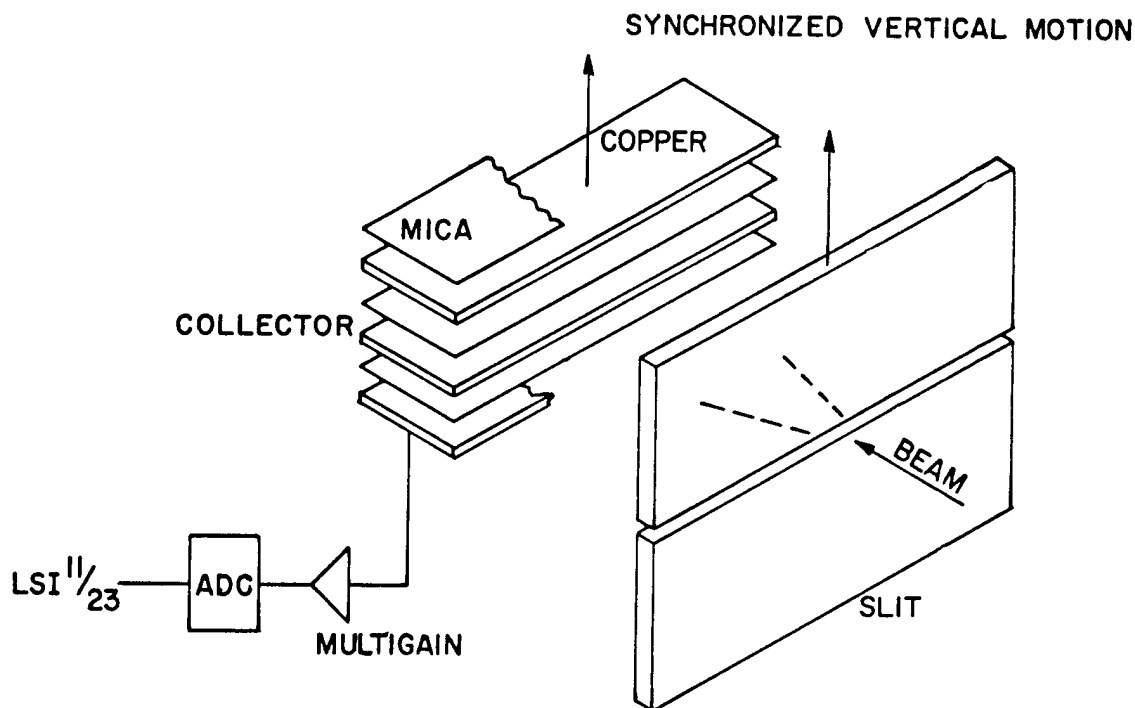


Fig. 3.  
Vertical emittance detector schematic.

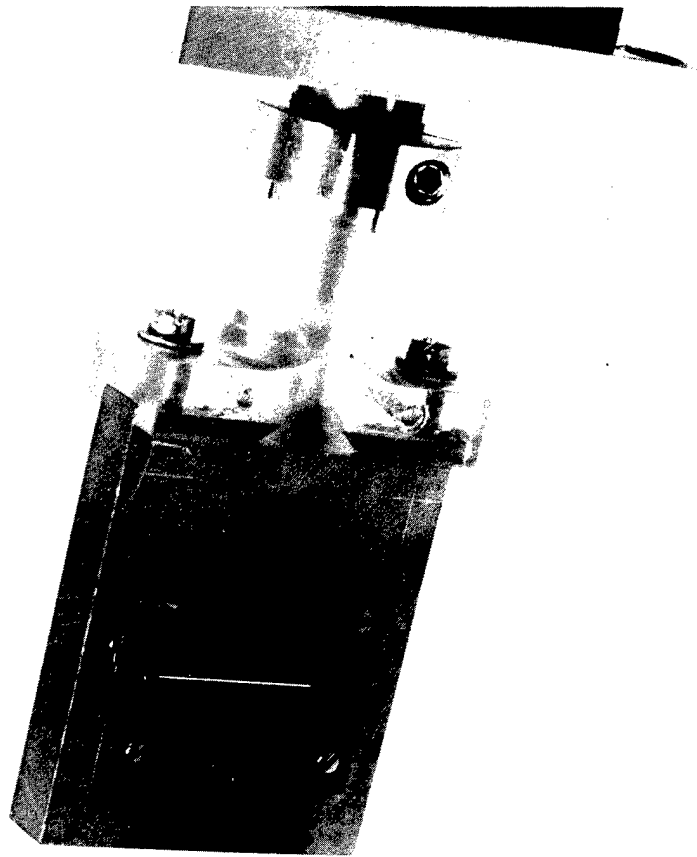
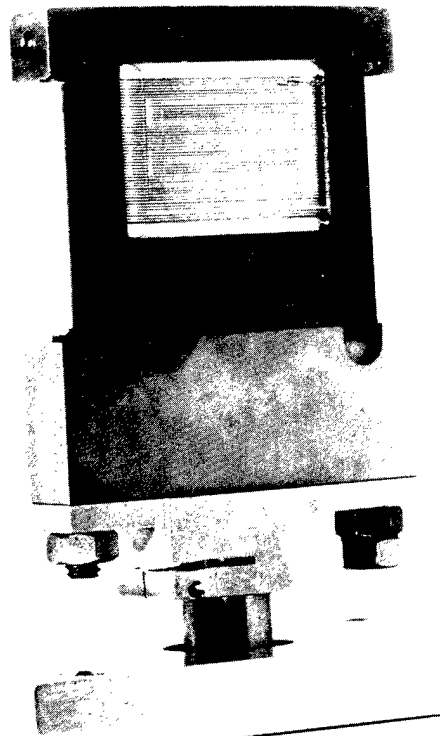


Fig. 4.  
Slit-and-sandwich collector.

### III. SOFTWARE DEVELOPMENT

The beam transport code, TRACE, has been improved and expanded and is now documented with an extensive "HELP" package. The HELP file (Figures 5a, b, and c) furnishes to an inexperienced user all information necessary for using all aspects of this code. Operation and data taking of the emittance stations ES1, ES2, ES3, and ES4 are now completely computerized. A standardized data-taking procedure is being developed and is being used at ES1 and ES2. With the use of overlay computer techniques, we now have real-time graphic display of the data as they are being collected. The analyzing code REANL is operational and, in addition to giving relevant ellipse parameters of the beam, gives graphics displays of the data. Figures 6 and 7 are the isoplot and the contour plot generated by REANL.

INSTRUCTIONS FOR DATA INPUT

DATA INPUT IS PROMPTED WITH THE WORDS 'ENTER INPUT'.  
THE DATA IS ENTERED IN THE FOLLOWING FORM:

variable=value;variable=value;.....  
OR: subscripted variable=value,value;.....

UP TO 80 CHARACTERS MAY BE ENTERED AT A TIME.  
FIELDS MUST BE SEPARATED WITH SEMICOLONS(;).

THESE VARIABLES MAY BE ENTERED WITH FLOATING POINT DATA:

- BEAMI(4) - beam parameters at starting element  
(alpha-x,beta-x,alpha-y,beta-y)
- BEAMF(4) - beam parameters to be matched at final element  
(alpha-x,beta-x,alpha-y,beta-y)
- BEAMP(4) - output beam parameters
- CONU(4) - conversion factors for ME/MP display
- PCONU(6) - conversion factors for PE/PP display
- A(5,50) - element parameters (see HELP, page 2)
- SIG(4,4) - sigma matrix
- ER - rest mass (MeV)
- Q - charge
- DPOP - momentum displacement (dp/p in X)
- U - kinetic energy (MeV)
- XM - scale for X MAX on emittance graph (mm)
- XPM - scale for X' MAX on emittance graph (mrad)
- XI - effective current (ma)
- SFMAX - max. step size for calculation (mm)
- EXI - horiz. emittance at starting element (4xRMS)
- EVI - vert. emittance at starting element (4xRMS)
- EX - horiz. emittance at final element (4xRMS)
- EY - vert. emittance at final element (4xRMS)
- VM - scale for max. radius on profile graph (mm)
- WAVEL - wavelength (mm)

THESE VARIABLES MAY BE ENTERED WITH INTEGER DATA:

- MT(50) - element types (see below)
- M1 - number of starting element for beam trace
- M2 - number of final element for beam trace
- ME(4) - elements designated for matching
- MP(4) - parameter of element designated for matching
- PE(6) - elements for 'printout values' on graph
- PP(6) - parameter of element for printout on graph
- MU - number of variables for matching (max 4)
- MT - type of matching (see HELP, page 3)
- NIT - max number of iterations during matching
- MRC - scope margins (4096 x 3200 max)
- IXU - scope width
- IYU - scope width
- IYP - height of profile on scope

YOU ARE BACK IN COMMAND MODE

Fig. 5a.  
HELP file documentation of TRACE.

COMMAND DESCRIPTIONS

TO IMPLEMENT THE CORRESPONDING COMMAND, TYPE:

- \*H (HELP) - COMMANDS, INSTRUCTIONS, INPUT PARAMETERS
- \*P (PRINT) - PRINT ENTIRE INPUT FILE
- \*I (INPUT) - INPUT CHANGES TO EXISTING DATA
- \*A (ADD) - ADD ELEMENTS IN BEAM LINE
- \*D (DELETE) - DELETE ELEMENTS IN BEAM LINE
- \*G (GRAPH) - GRAPH BKGRND, TRACE BEAM PROFILE
- \*T (TRACE) - TRACE BEAM PROFILE ON EXISTING BKGRND
- \*O (OUTPUT) - BEAM VALUES ONLY, NO GRAPH OR TRACE
- \*M (MATCH) - MATCH DESIRED VALUES USING VARIABLES
- \*N (MATCH) - MATCH, BUT NO ITERATION PRINTOUT
- \*K (MISMATCH) - CALCULATE/DISPLAY MISMATCH FACTOR
- \*U (VARIABLES) - DISPLAY VALUES OF MATCHING VARIABLES
- \*E (ERASE) - ERASE SCREEN (req'd for cursor control)
- \*S (SAVE) - SAVE NEW VERSION OF DATA INPUT FILE
- \*B (BRING) - BRING IN A NEW DATA FILE
- \*C (CLOCK) - DISPLAY DATE AND TIME
- \*F (FILENAME) - DISPLAY FILENAME
- \*W (WRITE) - WRITE NOTE ON OUTPUT
- \*L (LOGOFF) - LEAVE/TERMINATE THE PROGRAM
- \*R (MATRIX) - DISPLAY SIGMA MATRIX ELEMENTS
- \*X (EXCHANGE) - EXCHANGE VALUES PER EXCHANGE CODE:  
(1)-Exchange BEAMF/BEAMI,NI/N2 values  
(2)-Exchange BEAMO/BEAMI,NI/N2 values  
(3)-Enter BEAMO in BEAMI, N2 in M1  
(4)-Enter BEAMO in BEAMF  
(5)-Restore BEAMI (plus EXI,EYI,XI,U)  
(6)-Restore BEAMF

TYPES OF ELEMENTS

A MAXIMUM OF 49 ELEMENTS OF THE FOLLOWING TYPES (NUMBER OF PARAMETERS AS INDICATED) MAY BE ENTERED IN THE BEAM LINE:

Type #	Type	# of Parameters
1	- DRIFT	1
2	- QUAD	2
3	- DOUBLET (SYM)	3
4	- BENDING MAGNET	5
5	- TRIPLET (SYM)	5
6	- BUNCHER/DEBUNCHER SIMULATOR	2
7	- SOLENOID	5
8	- TAPERED RF QUAD	3
9	- RF GAP	1
10	- THIN LENS	5
11	- ACCELERATOR TANK	5
12	- ACCELERATOR COLUMN	5
13	- CURRENT CHANGE	1

(See HELP, page 2, for description of parameters - TYPE 'H')



TYPES OF MATCHING

MATCH TYPE (MT)	DESIRED VALUES TO MATCH (at MT)	HOW SPECIFIED	VARIABLES USED IN MATCHING	HOW SPECIFIED	NUMBER OF VARIABLES (NU)	COMMENTS
1	ALPHA-X BETA-X ALPHA-Y BETA-Y	BEAMF(1)=ALPHA-X BEAMF(2)=BETA-X BEAMF(3)=ALPHA-Y BEAMF(4)=BETA-Y	ANY	ME(1) = element number MP(1) = parameter number	4	TO DETERMINE MATCH
2	X' at X max Y' at Y max	BEAMF(1)=X' BEAMF(2)=Y'	PARAMETER	ME(2) = element number MP(2) = parameter number	2	AT ANY POINT IN BEAM-LINE
3	X max Y max	BEAMF(1)=X max BEAMF(2)=Y max	ANY	ME(3) = element number MP(3) = parameter number	2	POINT IN BEAM-LINE
4	X max X' max Y max Y' max	BEAMF(1)=X max BEAMF(2)=X' max BEAMF(3)=Y max BEAMF(4)=Y' max	BEAM ELEMENT	ME(4) = element number MP(4) = parameter number	4	BEAM-LINE
5	ALPHA-X BETA-X (n1=n2)	Program defaults on BEAM (see NOTE); it enters parameters in dummy element 50 (only the first two are used if MT=5): A(1,50)=ALPHA-X A(2,50)=BETA-X A(3,50)=ALPHA-Y A(4,50)=BETA-Y	INPUT BEAM PARAMETERS (usually the same as BEAMI)	Done automatically - Program uses dummy element 50 and sets up the following (only the first two are used if MT=5): ME(1)=50 MP(1)=1 ME(2)=50 MP(2)=2 ME(3)=50 MP(3)=3 ME(4)=50 MP(4)=4	2	LIMITING SECTION: BEAM CLIPPING (X and X')
6	Input & output base parameters	A(1,50)=ALPHA-X A(2,50)=BETA-X A(3,50)=ALPHA-Y A(4,50)=BETA-Y	ANY PARAMETER OF ANY BEAM ELEMENT	ME(1) = element number MP(1) = parameter number ME(2) = element number MP(2) = parameter number	2	FOR PERIODIC SYSTEM (sets output = to input)
7	ALPHA-X BETA-X	BEAMF(1)=ALPHA-X BEAMF(2)=BETA-X	ANY PARAMETER OF ANY BEAM ELEMENT	ME(1) = element number MP(1) = parameter number	2	FOR SOLENOIDS
8	ALPHA-Y BETA-Y	BEAMF(1)=ALPHA-Y BEAMF(2)=BETA-Y	ANY PARAMETER OF ANY BEAM ELEMENT	ME(2) = element number MP(2) = parameter number	2	FOR SOLENOIDS

NOTE: If values other than BEAMI are desired, they may be entered in dummy element 50 as shown

YOU ARE BACK IN COMMAND MODE

Fig. 5c.  
HELP file documentation of TRACE.

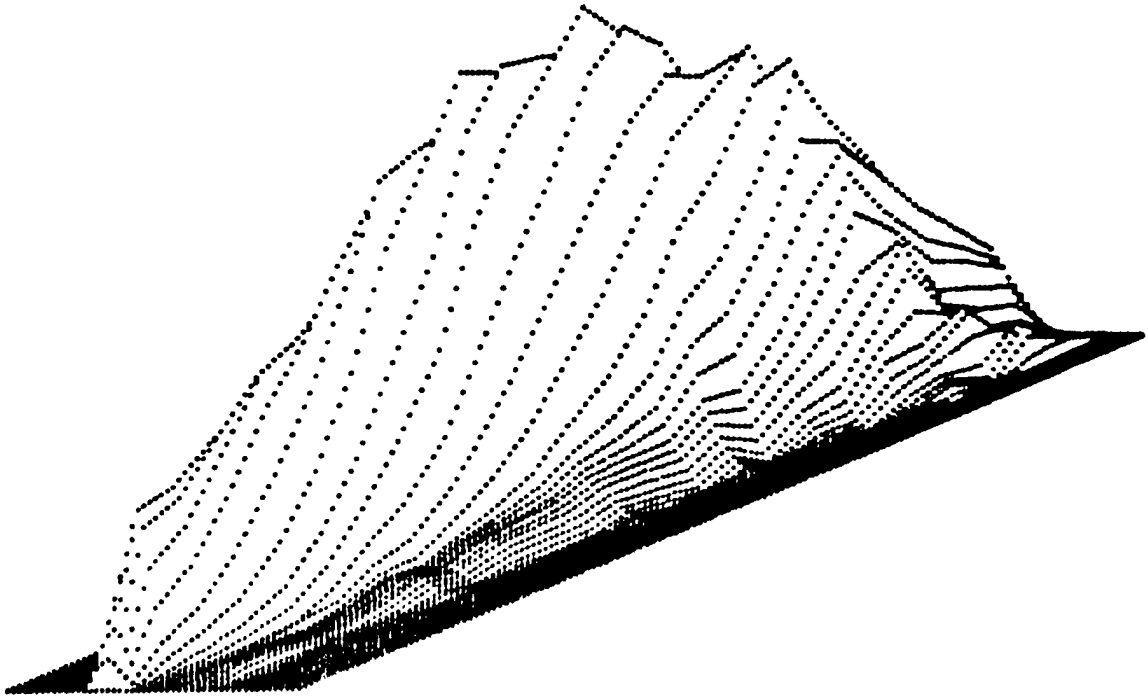


Fig. 6.  
Isoplot of data at ES3.

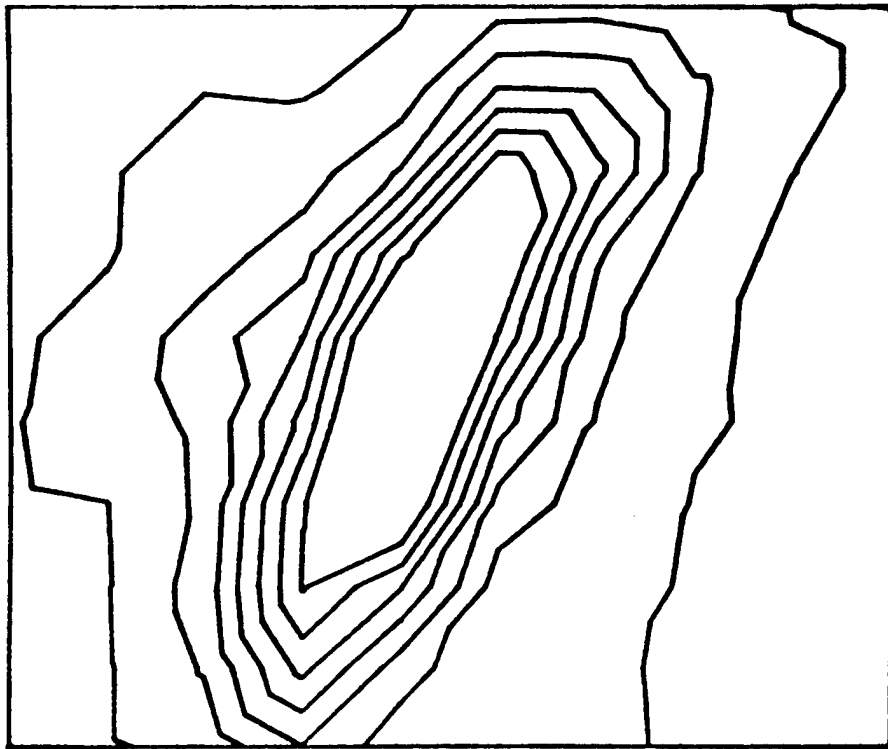


Fig. 7.  
Contour plot of data at ES3.

## ION SOURCE AND ATS INJECTOR

### I. ATS INJECTOR

A substantial fraction of the ion source effort during the year was directed toward injector operation, maintenance, and improvement. The most significant operational improvement was made when we discovered that 20-kV extractor sparking interacted with the gas-valve controller, so that a single spark caused the valve to open wide, forcing a full sparkdown. Since we corrected this problem, the sparkdown rate has decreased more than an order of magnitude to one every few hours. Erratic behavior of the extractor regulator was traced to faulty protective diodes; now we operate with good reliability at over 20 kV with  $\pm 20$ -V stability, adequate to prevent emittance growth in the 90° magnet. Extracted current at our 5-Hz, 1-ms duty factor has been 100 to 150 mA. The measured current at 100 kV has been 50 to 80 mA; however, the 100-kV cup has a secondary-electron emission problem so that the actual current is somewhat higher.

The most troublesome operational problem has been the long conditioning time required to get good operation with new source parts. Use of purer molybdenum (under 200-ppm impurities, mostly carbon) and vacuum bakeout at 1425°C has helped, but  $\sim 20$  h of break-in operation is required before reliable beam can be delivered. This is a significant fraction of the 100- to 200-h lifetime of the parts. It seems increasingly desirable to precondition these parts on the ISTS. A spare source with an external cesium supply has been built and put into operation. With the external supply, the cesium cycling time should be several hundred hours instead of the present 30 h. These measures should result in a big improvement in beam availability.

Much of the injector operation was for providing 100-keV beam for studies of the transport and diagnostics between the column and the RFQ match point. For one set of studies, the beam was collimated with two 2-mm apertures spaced 22.5 cm apart; the last aperture was located 4.4 cm before the 100-keV emittance scanner, ES2. This technique provided a beam of calculable phase space, largely independent of any settings of injector parameters, to help understand the subsequent beam transport and diagnostics; it also provided an interesting calibration check of ES2. The measured phase-space contour at low threshold

(Fig. 8) is in excellent agreement with the calculated boundary. The injector emittance scanners are now computer controlled as shown in Fig. 9.

The emittance of the injector beam has always been substantially higher than that from the prototype source on the ISTS. Also, the projection of the 20-keV emittance measured at ES1 (see Fig. 10 for a plan view) back to the source did not give beam radii corresponding closely to the beam size at the emission slit:  $r_x = 5$  mm,  $r_y = 0.25$  mm. Calculations showed that there should be emittance growth in the electromagnetic quadrupole before ES1 and that this could be reduced by installation of a PM quadrupole between it and

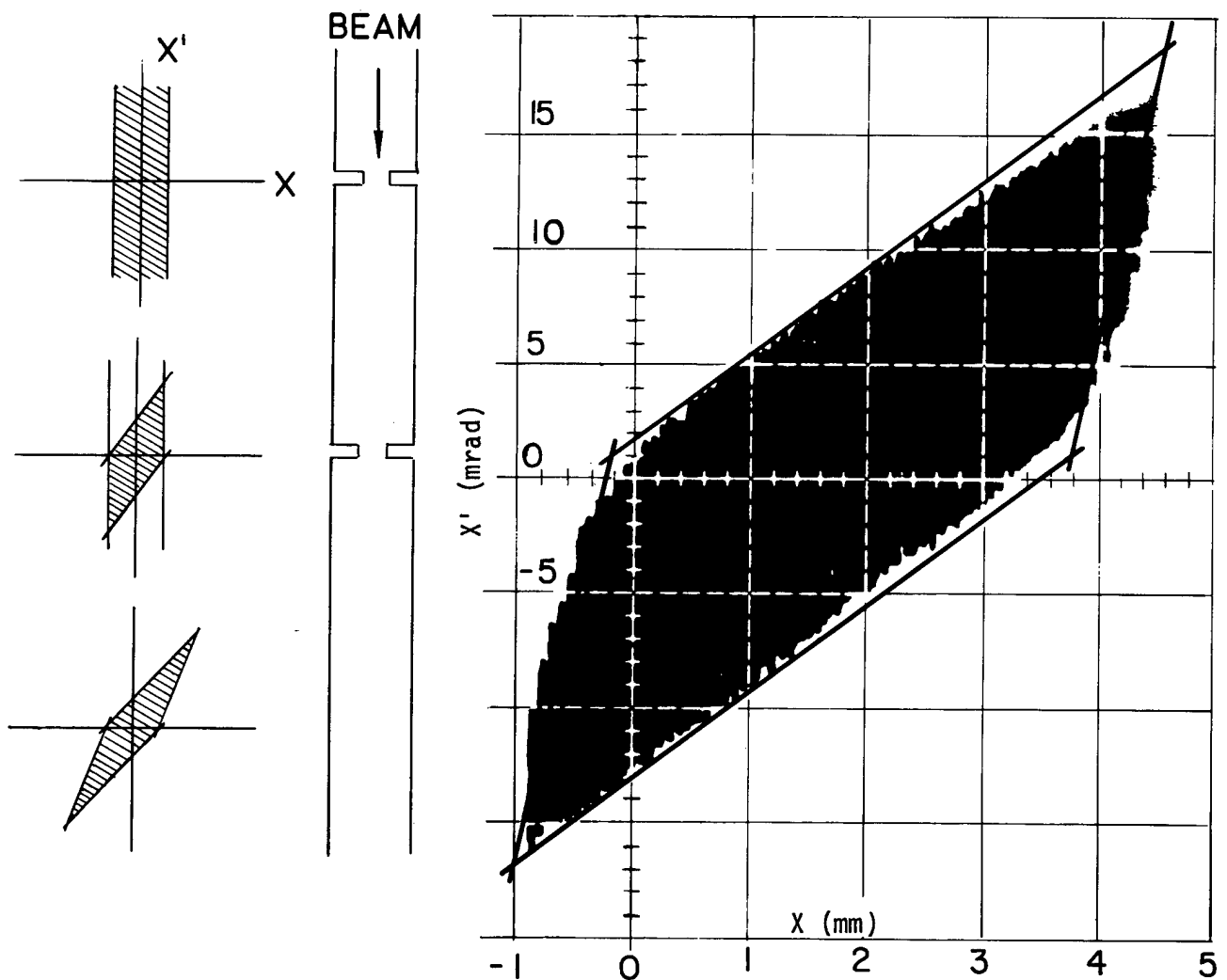


Fig. 8.  
Emittance measurement for collimated beam, with outline of calculated phase space at the 100-keV emittance scanner, ES2.

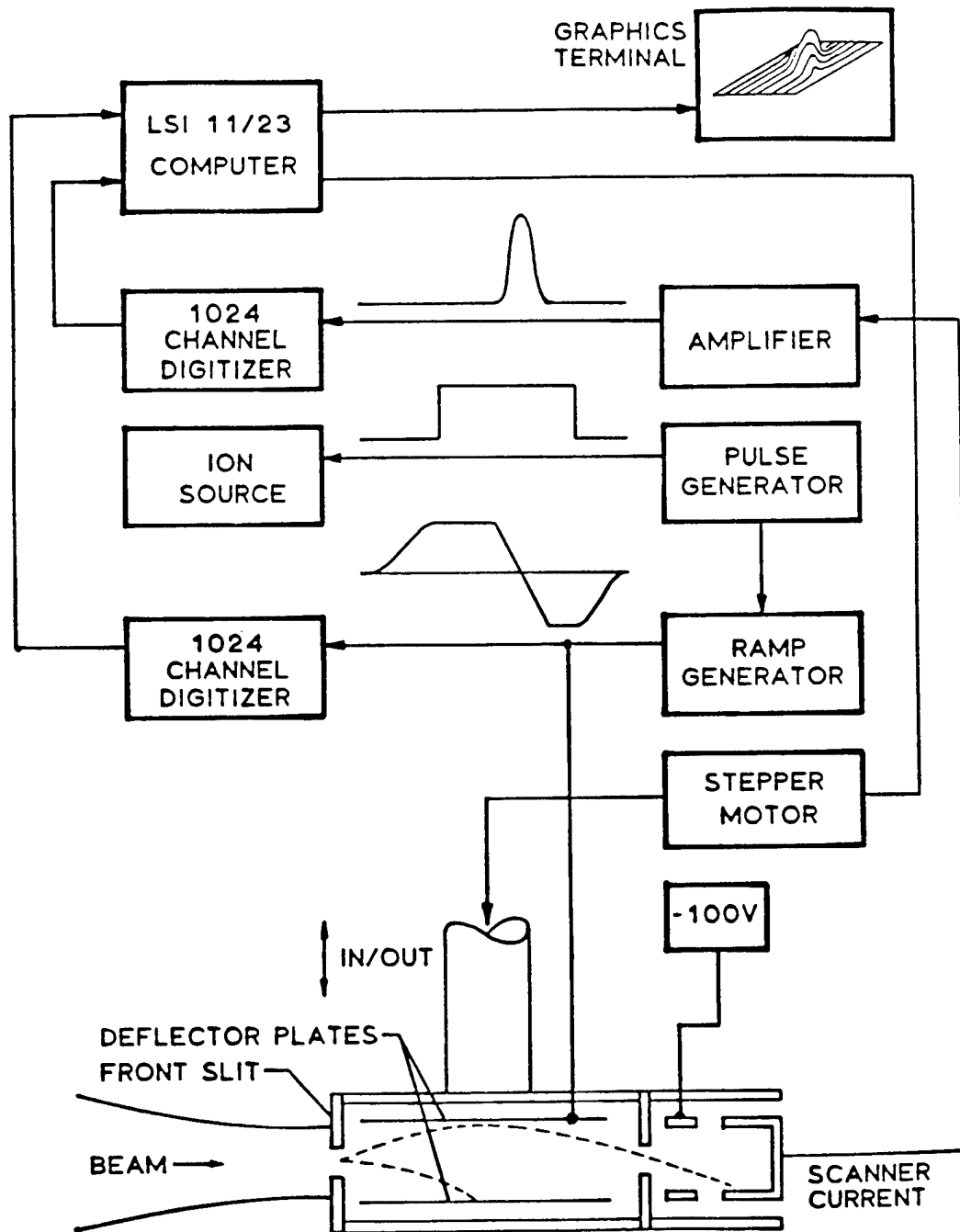


Fig. 9.  
Schematic of computer-controlled electrostatic emittance scanner.

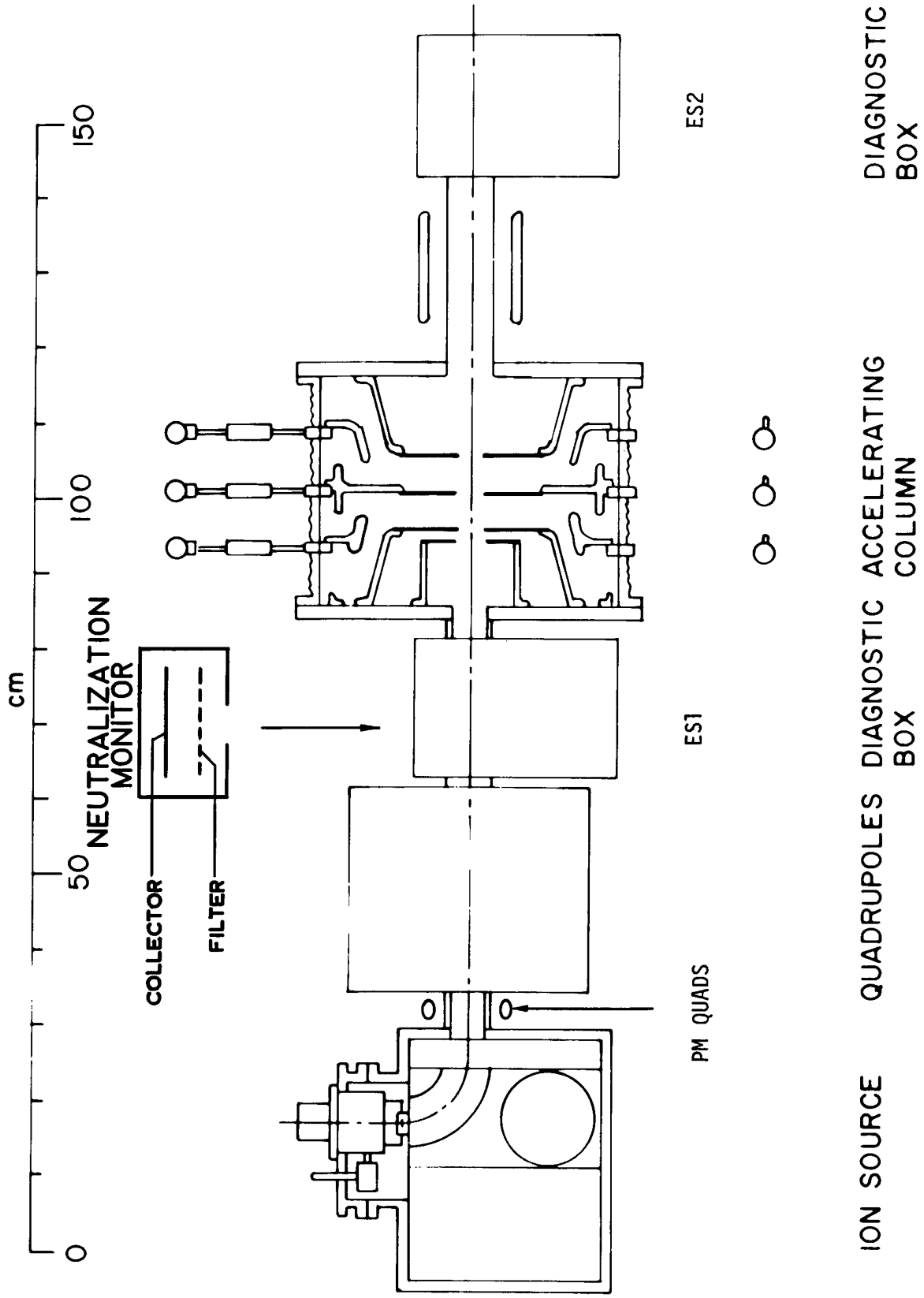


Fig. 10.  
Plan view of the ATS injector.

the bending magnet; however, emittance at ES1 was about the same before and after installation of the PM quadrupole:  $\epsilon_x = 0.06$  and  $\epsilon_y = 0.03\pi$  cm·mrad. An interesting observation had been that the phase-space density, as observed by the emittance scanner currents, had much greater fluctuation than the beam current itself and that the amplitude of fluctuations was progressively larger farther along the transport. Dzhabbarov recently reported beam-plasma oscillations produced by an  $H^-$  beam with conditions similar to those in the ATS injector, and he showed that the oscillations in current density were damped at high gas pressures in the transport line.<sup>1</sup> Normally we use xenon at a density of  $\sim 6 \times 10^{11}/\text{cm}^3$ , for which the stripping losses are 0.25%/cm. In accordance with Dzhabbarov's results, we examined the effects of much higher density.

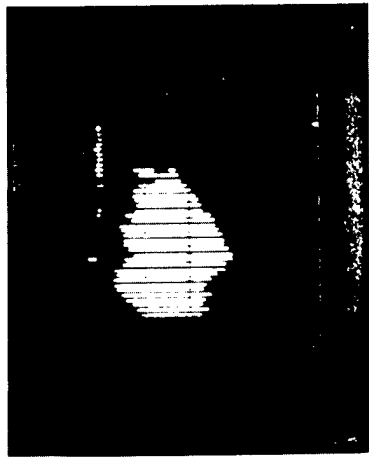
ES1 was positioned in the beam center; the scanner current, proportional to  $d^2i/dydy'$ , was recorded for 50 beam pulses for low and high xenon density. Substantial reduction in pulse-to-pulse fluctuations was observed (Fig. 11), along with a rotation of the phase space. The extracted current did not change significantly with xenon density and had  $\pm 5$  to 10% fluctuations. For these gas flows, the emittance versus beam-fraction data for the y-plane are shown (Fig. 12). The rms emittance was measured in both planes as a function of xenon density; results are shown in Figs. 13 and 14. In the y-plane, the emittance can be reduced by the factor 3; in x, by the factor 1.5. Smaller x-plane emittance has been observed at a different quadrupole tune, and we plan to explore the tune dependence further. It now seems likely that the emittance at the source is less than 0.02 in both planes, confirming previous measurements with a pepper pot near the extractor--and that (in addition to emittance growth in y caused by coupling in the bending magnet) there is growth in transport because of time variations in the beam neutralization. As a first step toward measurement of the beam neutralization, we have installed a device (Fig. 10) at ES1 to measure the flux and energy of charged particles ejected from the beam plasma. If we see oscillations similar to those described by Dzhabbarov, the frequencies should be  $\sim 600$  kHz for xenon and 5 MHz for hydrogen-neutralizing gases.

Holmes's theory<sup>2</sup> of quiescent neutralization for positive ion beams was extended to negative beams, and the residual potential well for a 100-mA, 20-keV  $H^-$  beam in xenon was calculated for various beam radii (Fig. 15). The relative electron density in the beam is given in Fig. 16. For a 1-cm beam



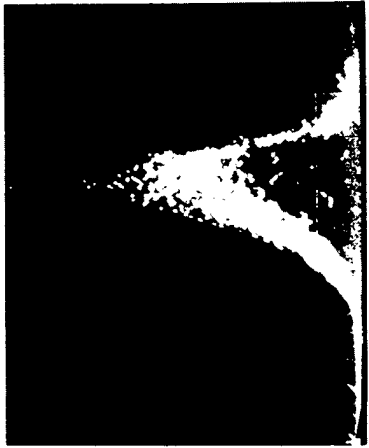
$$n_{Xe} = 0$$

200 us/d



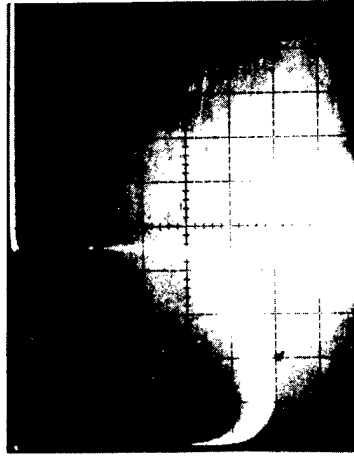
Y' (mrad/d)

Y (0.5 cm/d)



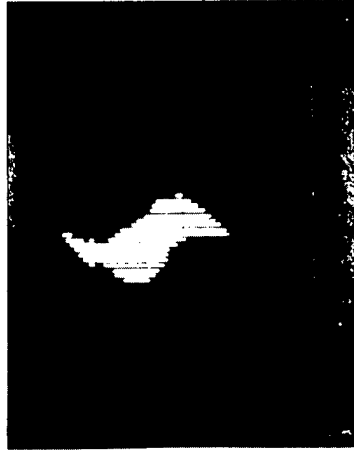
$d^2 i / dy dy'$

Y' (2.5 mrad/d)



$$n_{Xe} = 3 \times 10^{12} / \text{cm}^3$$

EXTRACTED CURRENT  
(20 mA/d)



Y-PLANE PHASE SPACE



DENSITY VARIATION FOR  
50 BEAM PULSES

Fig. 11.

Variation of beam properties with low and high xenon densities at ESI, the 20-keV emittance scanner. Shows extracted current, phase-space contour, and phase-space density variations for 50 consecutive beam pulses.

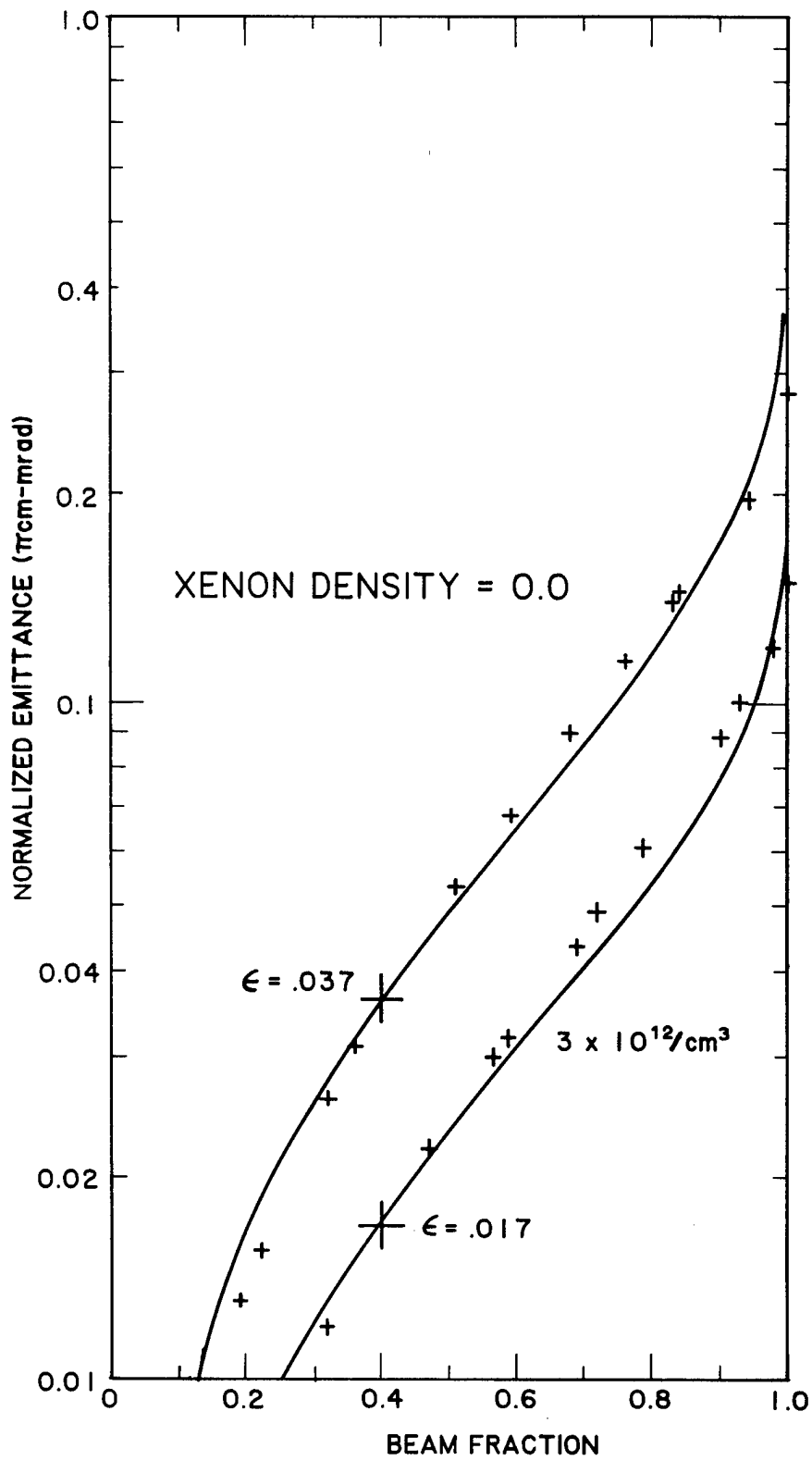


Fig. 12.  
Emittance versus beam fraction in y-plane at 20 keV for low and high xenon densities.

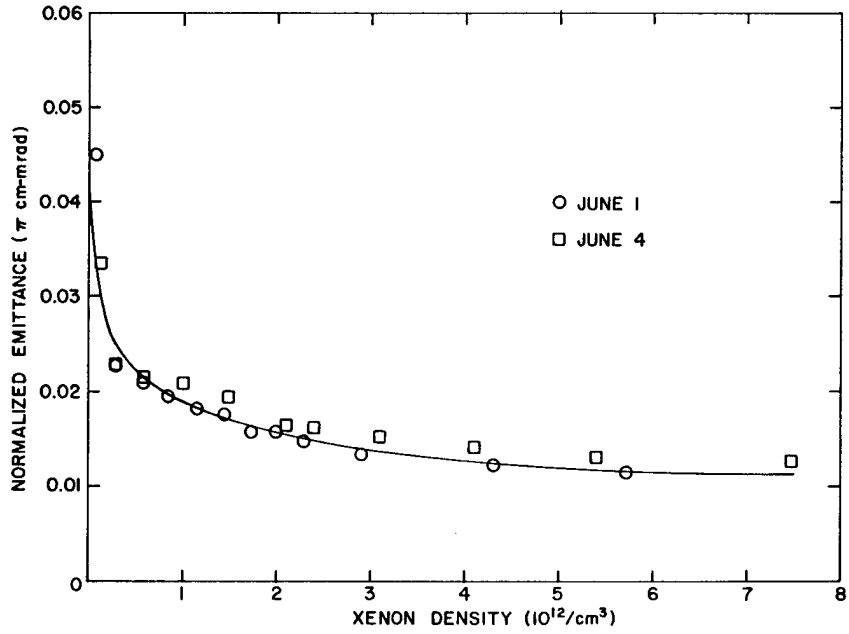


Fig. 13.  
The rms normalized emittance in y-plane versus xenon density at 20 keV.

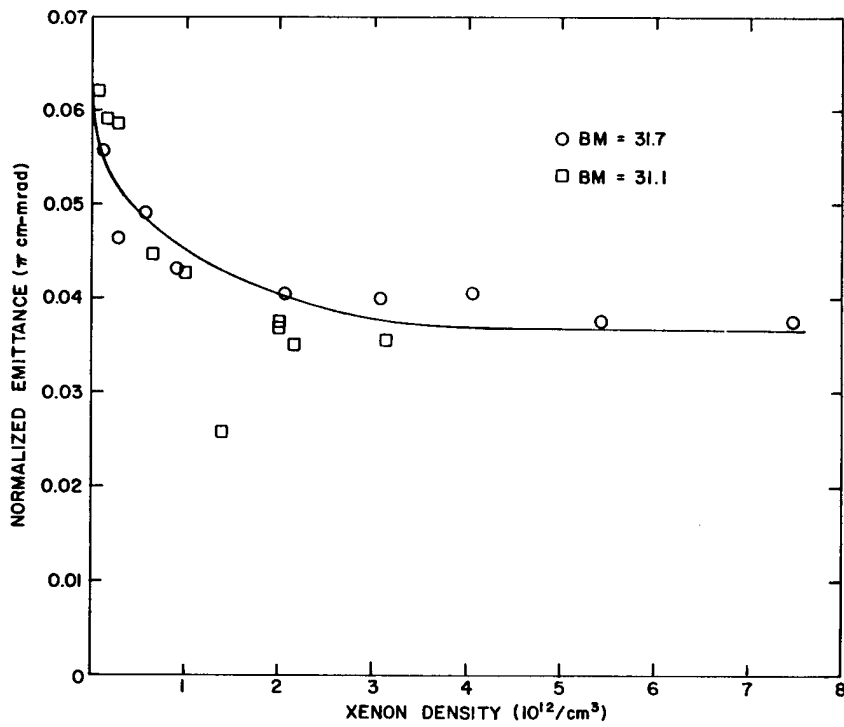


Fig. 14.  
The rms normalized emittance in x-plane versus xenon density at 20 keV.

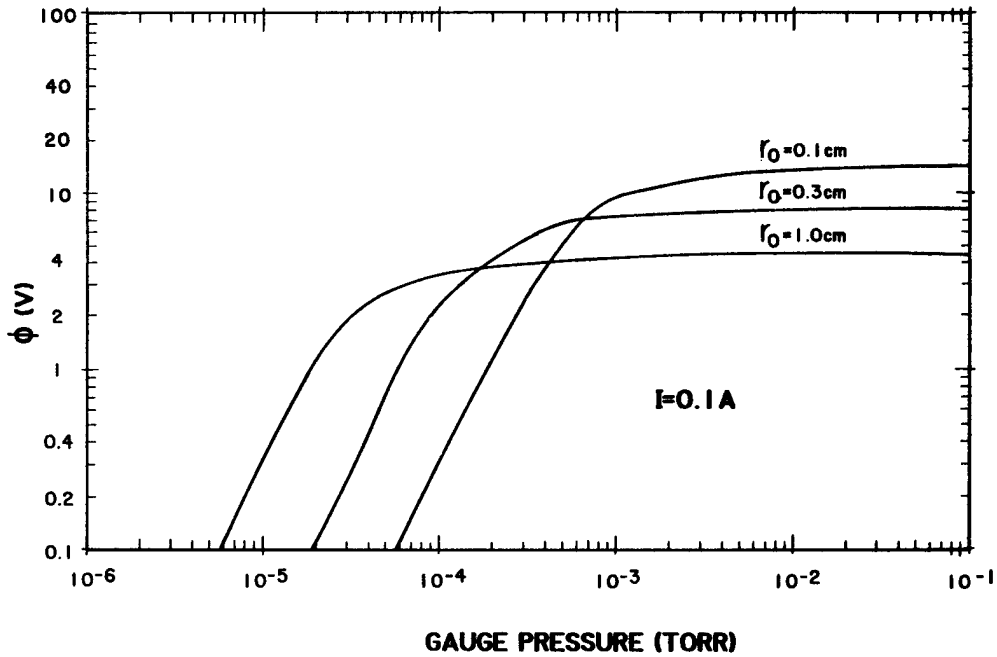


Fig. 15.

Calculated beam potential drop versus xenon gauge pressure for 100 mA of 20-keV,  $H^-$  ions for different beam radii. Calculated from Holmes's theory modified for negative beams.

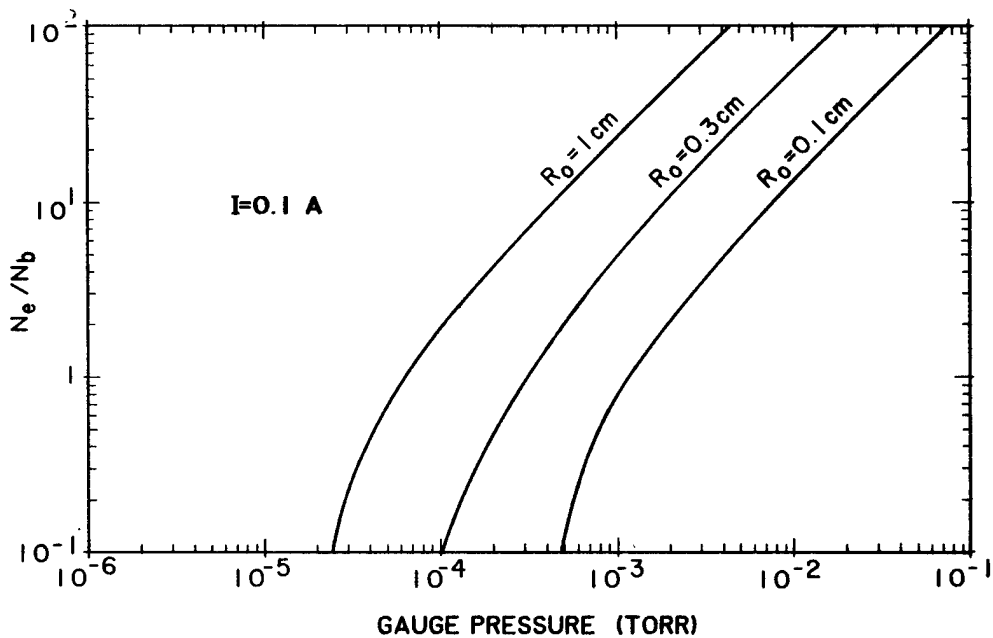


Fig. 16.

Ratio of electron density to beam density for 100 mA of 20-keV,  $H^-$  ions in xenon gas. Calculated from Holmes's theory.

radius, the well is  $\sim 4.5$  eV positive, giving an effective beam current of less than 1 mA (a net focusing force for the beam). From the measurements at ESI for high xenon density, we projected the beam phase space back to the source with TRACE (using four times the rms emittance and zero effective current) and found that the beam was near a waist in both planes with radii of  $r_x = 4.8$  mm,  $r_y = 0.6$  mm, close to the expected values. The beam then was projected forward for various effective currents  $I_{\text{eff}}$  to deduce the sensitivity of phase-space orientation to current. The calculated phase spaces at ESI are shown in Fig. 17 for  $I_{\text{eff}}$  equal to  $\pm 3$  mA. A formula was derived

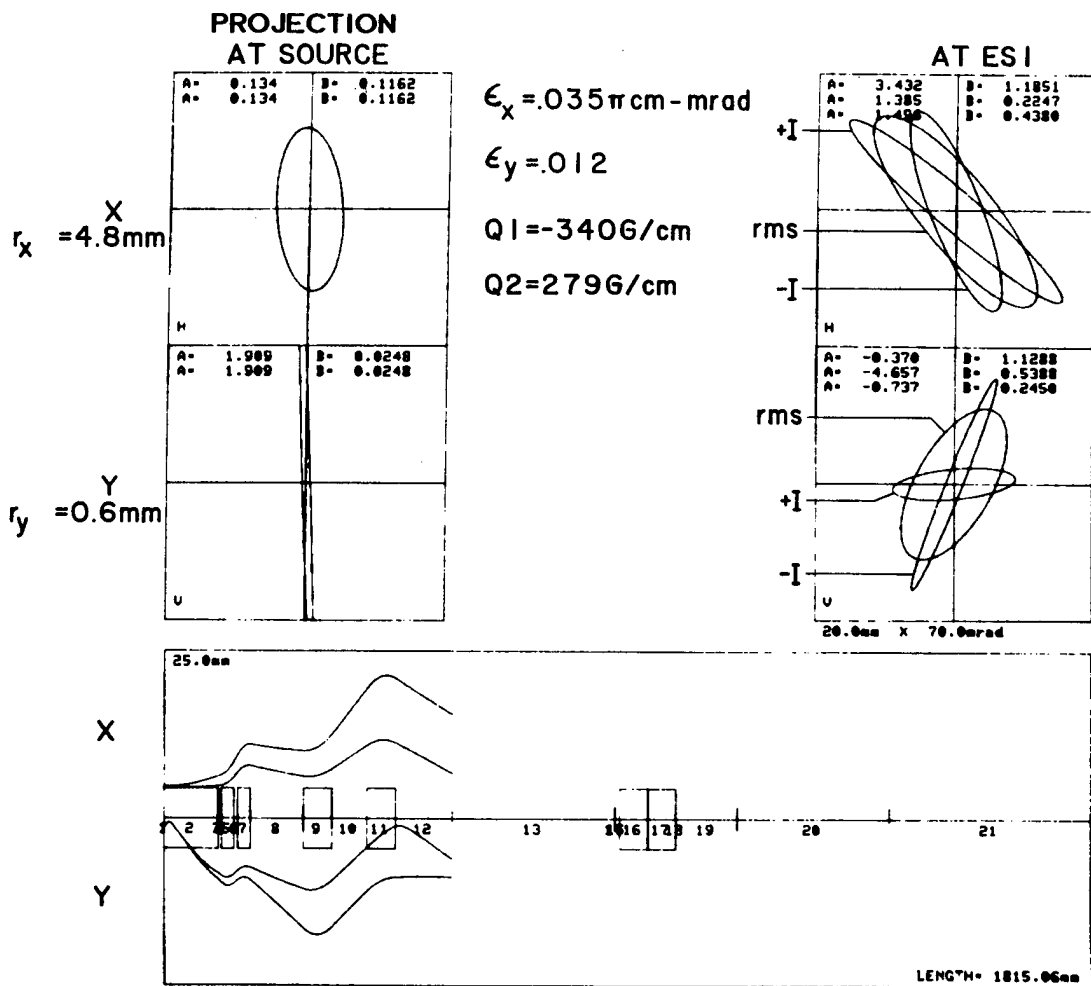


Fig. 17.

Beam-transport calculations, using TRACE, between source and ESI. With high xenon density, the measured phase space at ESI projected back to the source gives nearly the physical slit size. When projected back to ESI with an effective current of +3 mA or -3 mA, the phase spaces do not overlap, resulting in an effective increase in emittance.

for the rms emittance of two superimposed ellipses of uniform current density, and the calculated rms ellipse is shown on the same plots. The emittance-growth factor as determined by this method is shown as a function of  $I_{\text{eff}}$  (Fig. 18). A value of  $I_{\text{eff}} = 3 \text{ mA}$  would account for our measured emittance growth (Figs. 13, 14). The neutralization time constant for  $\text{H}_2$  at  $10^{-4}$  torr is  $10 \mu\text{s}$ ; for xenon at  $2 \times 10^{-4}$  torr, it is  $1 \mu\text{s}$ . The beam current at extraction typically fluctuates about  $\pm 10\%$  or  $\pm 10$  to  $15 \text{ mA}$ ; thus, we expect that fluctuation frequencies higher than  $100 \text{ kHz}$  could cause the emittance growth in the absence of xenon. Frequency-spectrum analysis of the extracted current does not show any pronounced frequencies, but further measurements are required. We might expect that, if there is sufficient electron density, the electrons would be expelled rapidly or retained in the beam to maintain the neutralization; electron density (Fig. 16) may be high enough for this at the highest xenon density, but a theory connecting fluctuations in current with the dynamics of the neutralizing plasma is necessary to make the calculation.

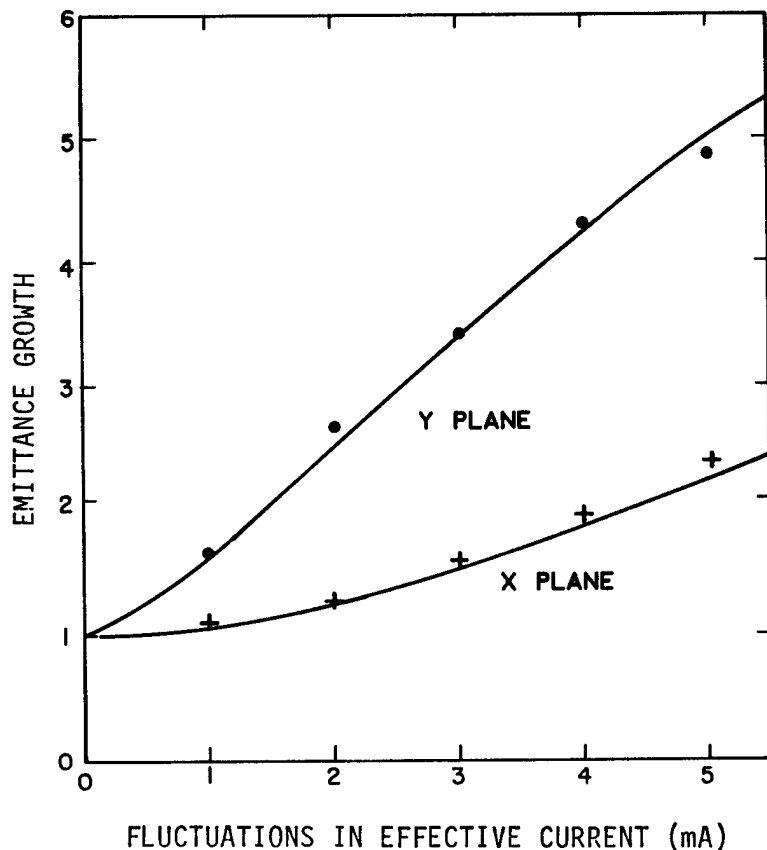


Fig. 18.  
Emittance growth calculated by the above method versus fluctuations in effective current.

## II. CIRCULAR-APERTURE SOURCE DESIGN

With the present ATS injector source, the  $H^-$  beam is extracted from a 10- by 1/2-mm<sup>2</sup> slit. The resulting asymmetry in emittance is quickly lost because of coupling of the planes in the 90° magnet and, in any case, would be lost in the RFQ. Extraction from a circular emitter is desirable to produce a beam of minimum emittance (proportional to radius) with the lowest current density (proportional to the power density in the discharge), which is a possible limitation for dc operation. For the calculation of positive ion trajectories extracted from a plasma, several codes have been written, including WOLF,<sup>3</sup> AXCEL,<sup>4</sup> and SNOW.<sup>5</sup> The SNOW code, developed at Sandia and in use at Los Alamos, assumes a collisionless plasma with electrons in a Boltzman equilibrium with the ions. A finite number of ion rays are traced through the plasma and system of electrodes, with the potentials at all points calculated by a self-consistent relaxation process with fixed conditions along the boundary and electrodes. Although all of these codes have been well tested for their zero- and first-order predictions (total current and envelope divergence), there have not been, to our knowledge, comparisons with analytic models for second-order (emittance) predictions. Of special concern is that the overall accuracy be adequate to make this calculation. For this purpose, an rms emittance calculation was added to SNOW,

$$\epsilon_{xx'} = \frac{\beta\gamma}{\sqrt{2}} \sqrt{\frac{\sum I_j r_j^2 \sum I_j r_j'^2 - (\sum I_j r_j r_j')^2}{(\sum I_j)^2}},$$

where  $\beta$  and  $\gamma$  are the usual relativistic factors, and the  $j^{\text{th}}$  ray has current  $I_j$ , radius  $r_j$ , and divergence  $r_j'$ . Emittance in  $rr'$  space is projected into  $xx'$  space, resulting in a reduction by half. SNOW cannot handle skew rays; therefore, it is not possible to include these in the calculation. However, it can be shown that if skew rays have a distribution equivalent to that of the radial rays in a general distribution of cylindrical symmetry, then the emittance would be increased by  $\sqrt{2}$ , so we divide by  $\sqrt{2}$  in the formula above. For an ion-temperature-dominated beam, the emittance is

$$\epsilon = \frac{r}{2} \sqrt{\frac{kT_{\text{eff}}}{MC^2}},$$

so that we may define an effective ion temperature  $kT_{\text{eff}}$  by equating this to the value calculated by SNOW. Then  $kT_{\text{eff}}$  is a measure of the distortions in the system independent of scale size, although it may depend on extraction voltage.

First we studied a "perfect" Pierce case as a bench-mark calculation (Fig. 19). Plasma originates at the injection plane (in this case coincident with the plasma electrode) with ions having arbitrarily chosen longitudinal and transverse velocities and with the extraction electrode having no opening, thus eliminating equipotential distortions there. The computer calculation differs from an analytic calculation in the following ways:

1. finite mesh size, over which electrodes are placed and the voltage relaxation is carried out;
2. voltage on the radial boundary has a linear  $z$  dependence;
3. finite number of ion rays;
4. finite step size in the calculation;
5. possibility of nonconvergence and oscillations;
6. nonzero longitudinal and transverse velocities of ions at extraction;
7. finite electron temperature;
8. arbitrary location and shape of plasma sheath.

The dependence of the calculated results was minimal for Variables 3, 4, 5, 6, and 7; however, when the mesh size was decreased by a factor of 2 (to 141 by 81 from 81 by 41) the emittance decreased by a factor of 2, and hence  $kT_{\text{eff}}$  by a factor of 4 (Fig. 20). No investigation of the dependence on Variables 2 and 8 was made. It seems likely that  $kT_{\text{eff}}$  of arbitrarily small value could be achieved by taking a small enough mesh size. The calculated values are well below actual ion temperatures, and the distortions are primarily at the beam edge; therefore, the beam core has an even lower emittance.

To test SNOW's calculation of emittance, two types of distribution (Fig. 21) were injected into the perfect Pierce case.

1. Uniform divergence--at each radial point, rays with angles  $0, -\theta, +\theta$  having equal currents were injected, where  $\sin \theta = \sqrt{T_{\perp}/T_i}$ ,  $T_{\perp}$  being the transverse energy and  $T_i$  being the injected energy.

# PIERCE ELECTRODES

25kV, 13.2mA

141 x 81 matrix, 0.2mm/matrix square

$T_e = 0.1\text{eV}$ ,  $T_i = 10\text{eV}$

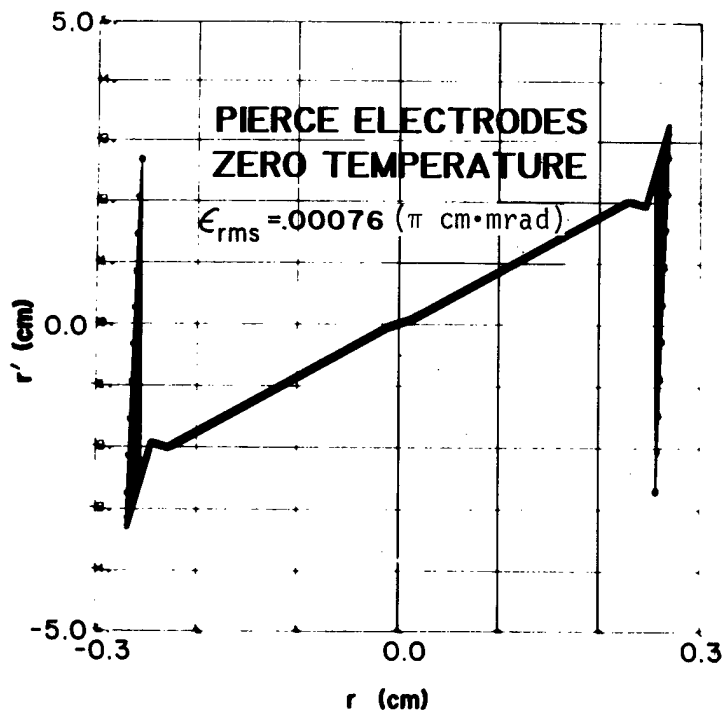
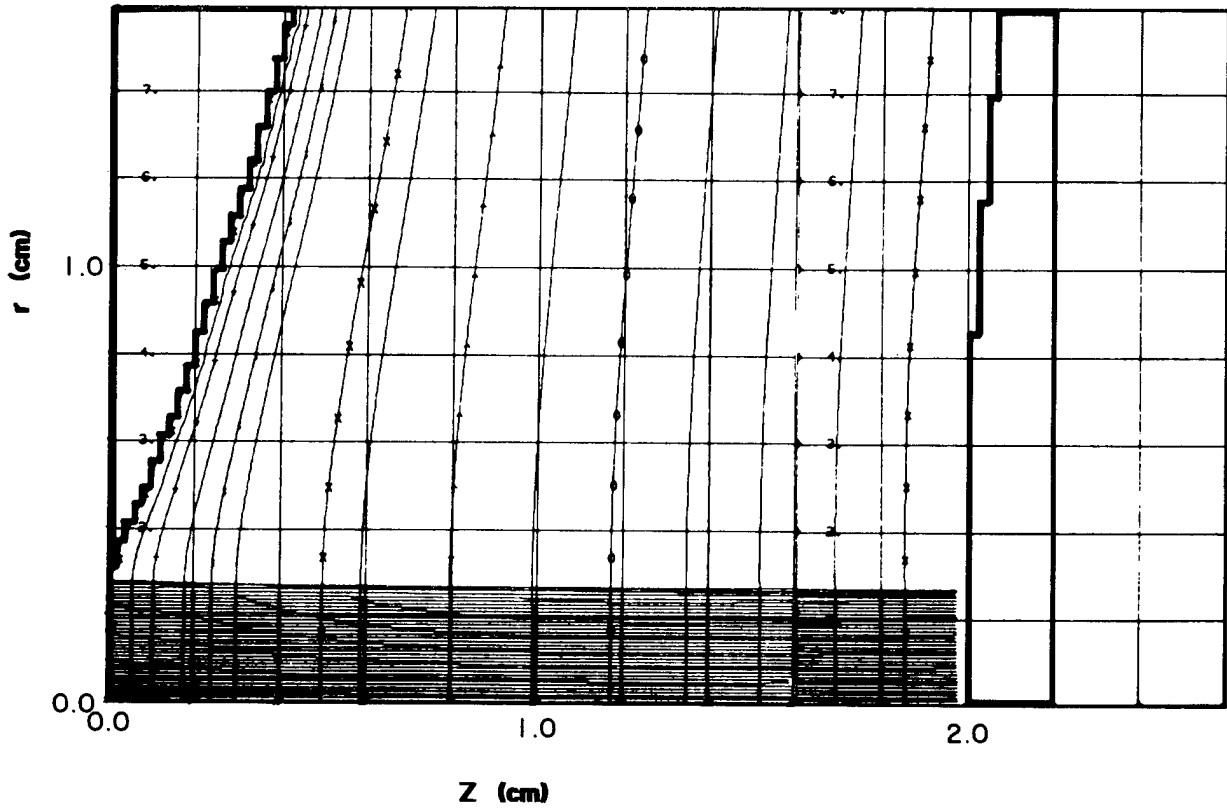


Fig. 19.  
Perfect Pierce test case.

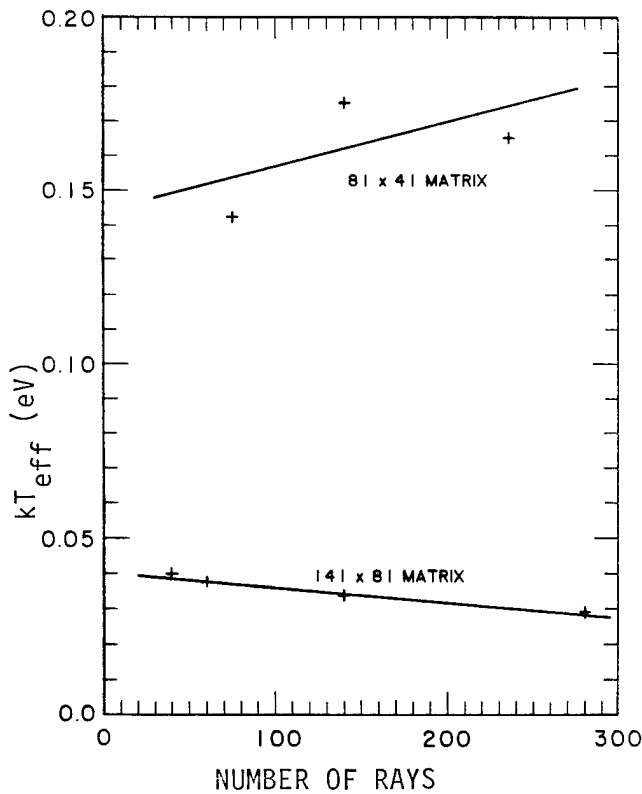


Fig. 20.  
Two mesh sizes are shown for  $kT_{\text{eff}}$  versus number of rays in the perfect Pierce case.

### UNIFORM MODEL

Equal current rays for  $-\theta, 0, +\theta$   
divergence; uniform radial distribution

$$T_{\perp} = T_i \sin^2 \theta, \quad T_i = \text{injected ion energy}$$

$$\text{Here, } \epsilon = r \sqrt{T_{\perp} / 3MC^2}$$

### MAXWELLIAN MODEL

Equal current rays for 10 angles

$$\langle \dot{x}_i^2 \rangle = \frac{\int_{\dot{x}_{i-1}}^{\dot{x}_i} \dot{x}^2 f(\dot{x}) d\dot{x}}{\int_{\dot{x}_{i-1}}^{\dot{x}_i} f(\dot{x}) d\dot{x}}$$

$$\text{where } f(\dot{x}) = e^{-M\dot{x}^2 / 2kT_{\perp}}$$

$$\text{So, } \epsilon = r/2 \left( \sqrt{kT_{\perp} / MC^2} \right)$$

Fig. 21.  
Test of emittance calculation in SNOW.

2. Maxwellian--at each radial point, 10 rays of equal current were injected with angles chosen so that the rms transverse velocity of the distribution was  $T_{\perp}/M$ .

The spatial density was taken to be uniform. For these distributions the rms emittance at emission is given in Fig. 21.

The percentage deviation of the SNOW calculations from these formulae was calculated over a range of parameters. For Distribution 1 the agreement was very good when  $T_{\perp}$  was kept constant and  $T_{\parallel}$  was varied (Fig. 22), or when  $T_{\perp}$  was varied and  $T_{\parallel}$  was kept constant (Fig. 23). For the Maxwellian case with fixed  $T_{\perp}$ , the agreement was good over a range of  $T_{\parallel}$  (Fig. 24). In summary, the calculations have adequate accuracy and are in good agreement with test cases.

Our goals for a circular extractor design are

- current of 150 mA,
- extraction field a maximum of 120 kV/cm,
- an acceptably low emittance, and
- acceptable beam divergence-- $\sim 100$  mrad or less.

We assume an  $H^{-}$  ion temperature of 4 eV, the upper limit for the Dudnikov source as deduced by its emittance; for this, a minimum current density would be  $0.22 \text{ A/cm}^2$ . As a starting point, the Langmuir-Blodgett equations for spherical flow were combined with the Davisson-Calbick equation for extractor defocusing, modified according to Wilson.<sup>6</sup> From this we obtained the parameters given in Table I from the design shown in Fig. 25.

Most of the optical aberrations occur at the emission surface, and they can be reduced by making the plasma electrode thinner or by making the injected ion energy larger, the latter normally not readily variable experimentally. With a 4-eV ion temperature, an artificially high ion energy of 100 eV was required to avoid nonuniform current-density build-up in the plasma, but the emittance was still acceptable (Fig. 26). Finally, for variations in current of  $\pm 10\%$ , the resulting phase-space orientations overlap sufficiently that the time-averaged emittance growth would be only a few per cent at extraction.

These results are encouraging thus far. Next, the problem of current density build-up needs to be resolved; then the shaping of the plasma electrode for minimal aberration will be investigated. With the results of the design of Fig. 25, the study of acceleration to 100 keV can begin. The best solution would be to accelerate immediately, if the voltage gradients are not too large and if beam divergence can be kept reasonable.

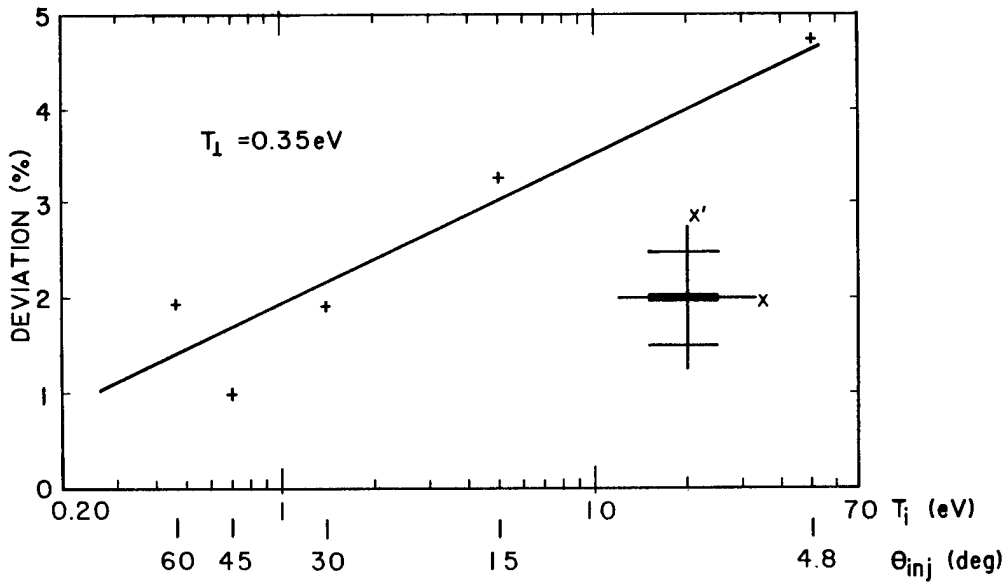


Fig. 22.

Deviation of uniform divergence calculations from theory versus ion injection energy; transverse energy held constant.

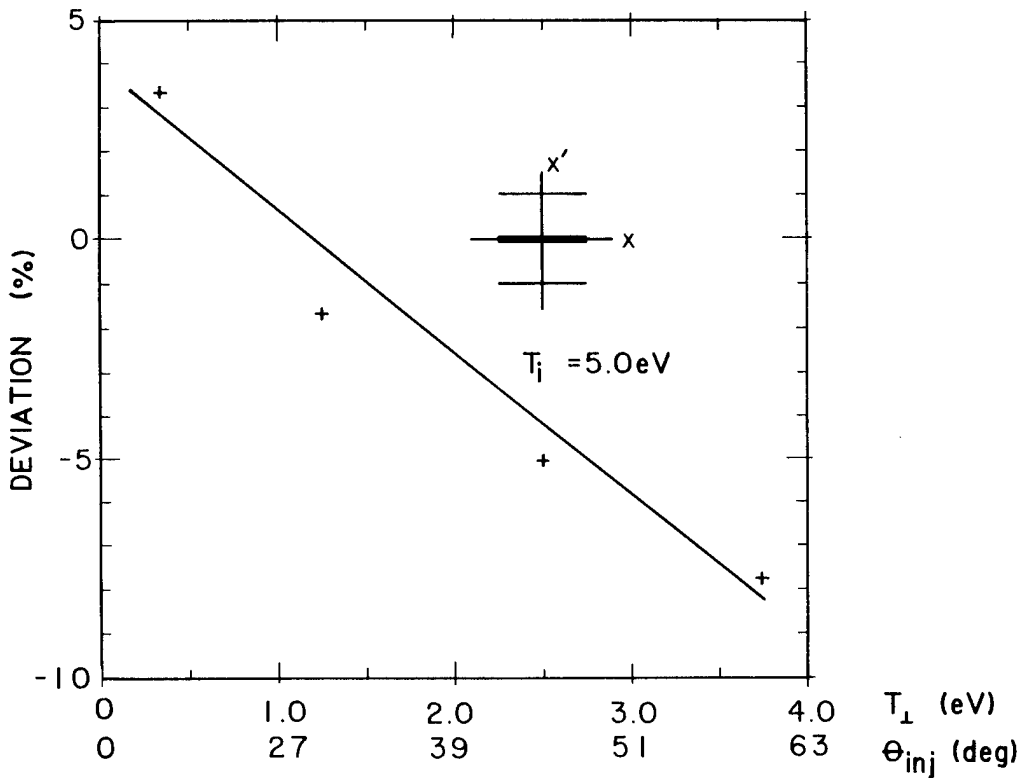


Fig. 23.

Deviation of uniform divergence calculations from theory versus transverse energy; ion injection energy held constant.

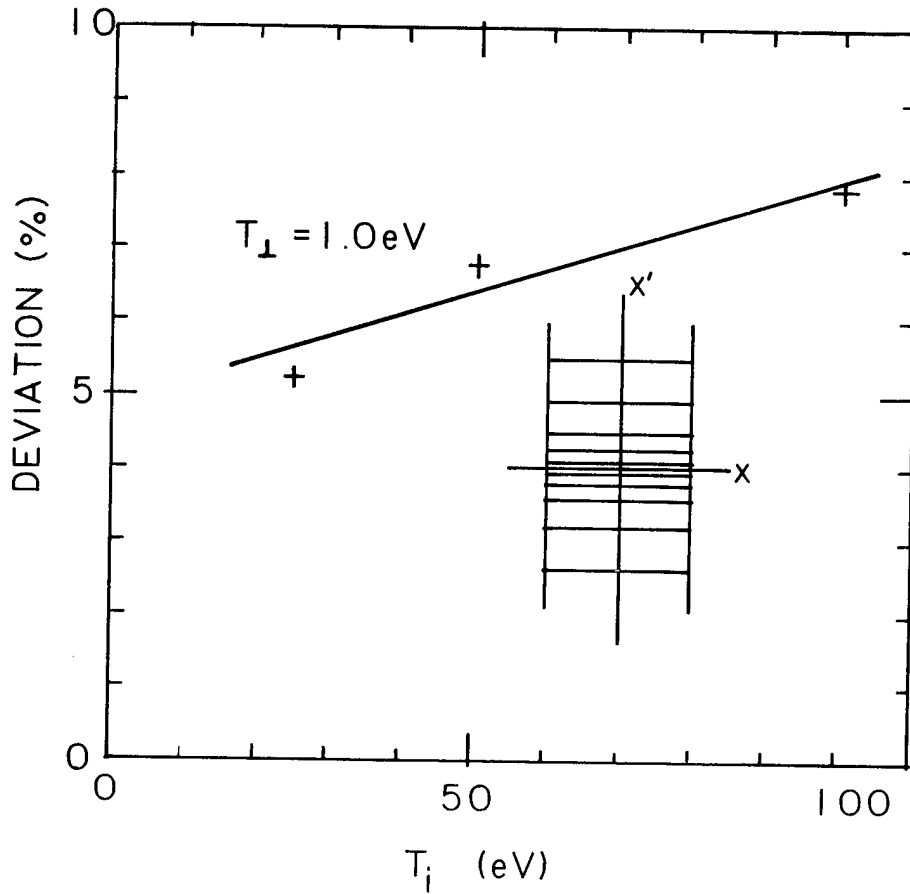


Fig. 24.  
Deviation of Maxwellian distribution calculations from theory versus ion injection energy; transverse energy held constant.

TABLE I

SPHERICAL PIERCE DESIGN PARAMETERS

Voltage	29 kV
Current	151 mA
Emittance	acceptably low
Current density	0.66 A/cm <sup>2</sup>
Emitter radius	0.27 cm
Injected ion temperature	0.0 eV

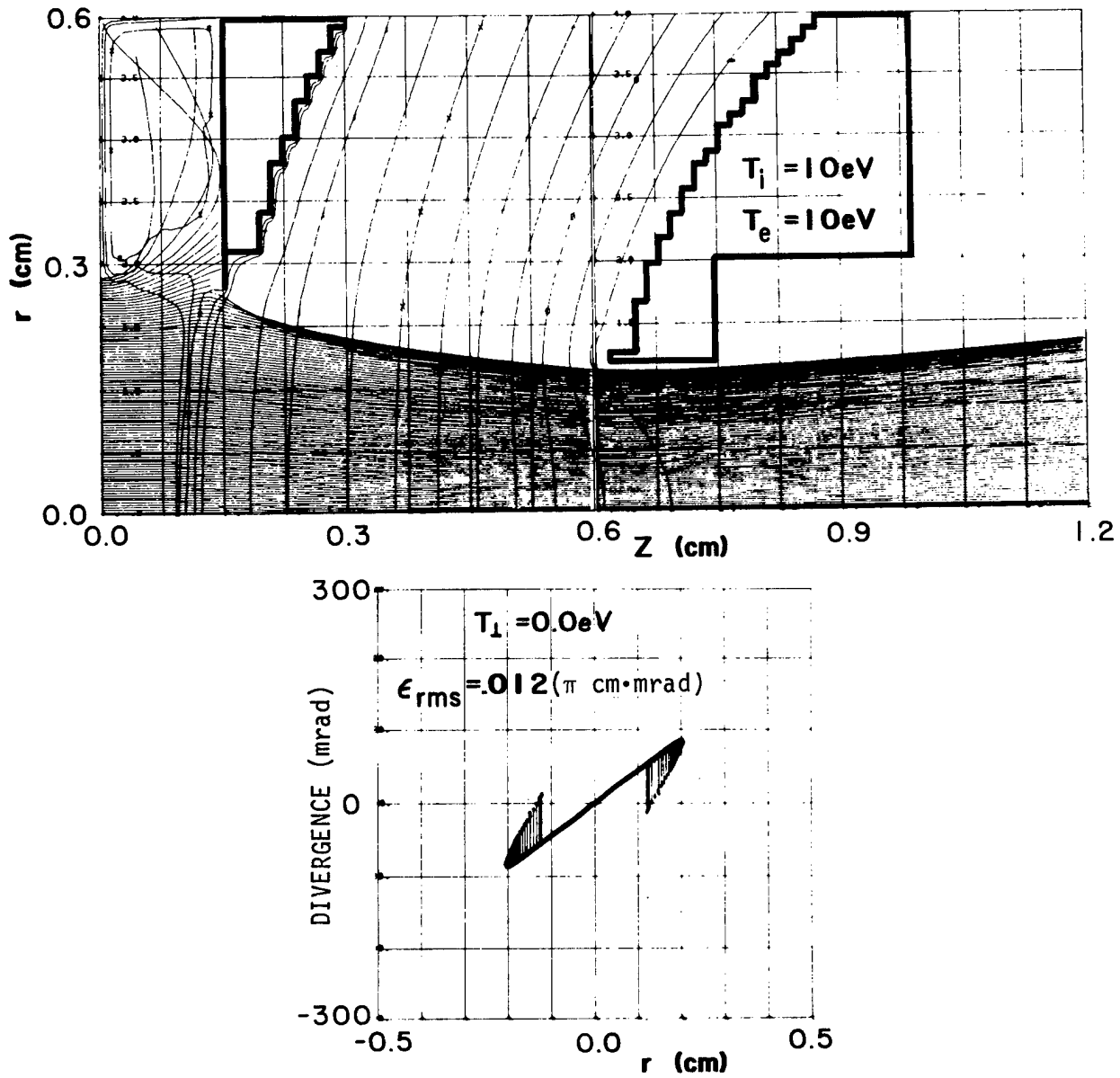


Fig. 25.  
 Calculated properties of spherical extractor with zero ion temperature and 10-eV injection energy.

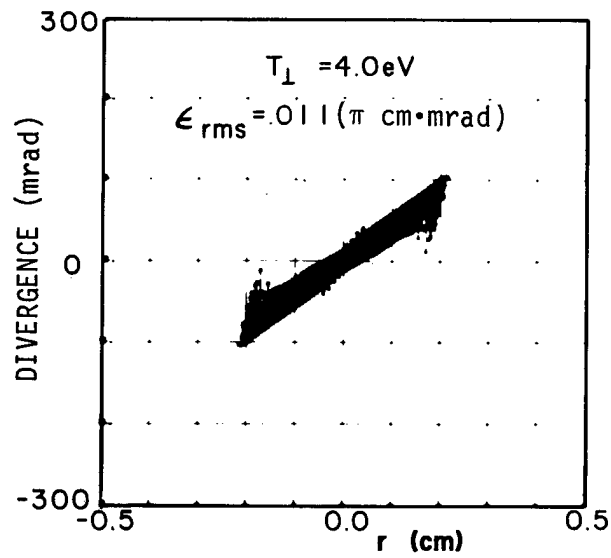
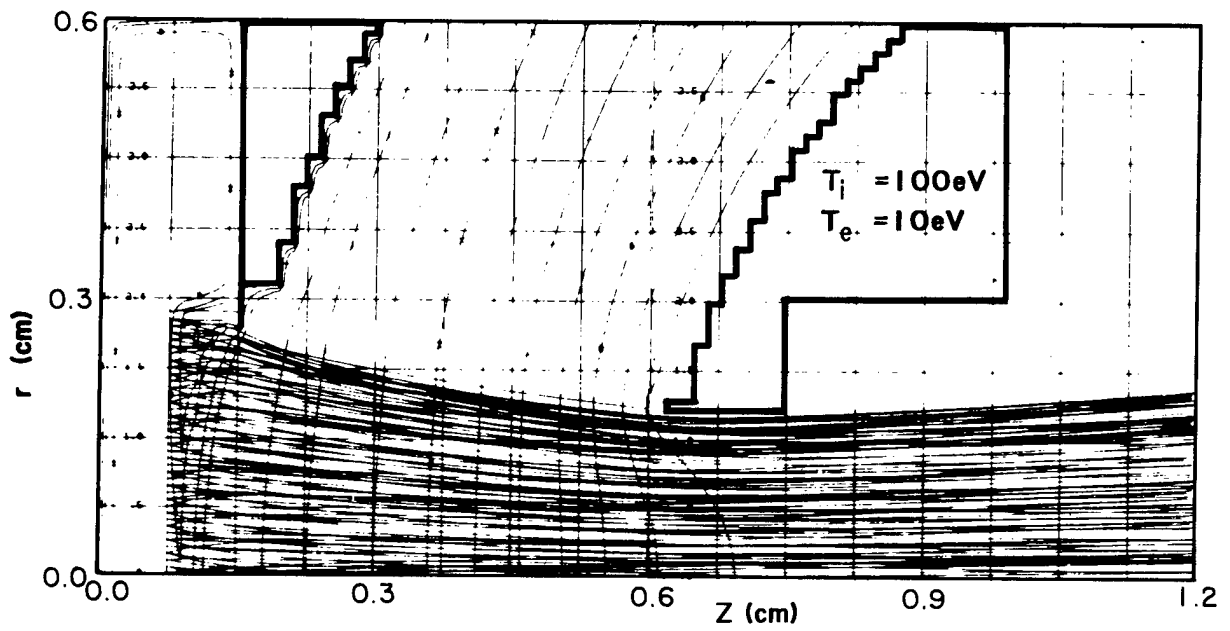


Fig. 26.  
 Calculated properties of spherical extractor with 4-eV ion temperature and 100-eV injection energy.

### III. CIRCULAR-APERTURE SOURCE SCALING

The pulsed ATS injector source can produce a beam of up to  $3.5\text{-A/cm}^2$  current density, but the power density in the discharge ( $\sim 10\text{ kW/cm}^2$ ) prevents extension of the duty factor to dc. The measured emittance is compatible with a 4-eV ion temperature. In this case it should be possible to produce a 150-mA beam from an 11-mm-diam aperture with a  $160\text{-mA/cm}^2$  current density and a low emittance. Scaling the source according to the laws of similarity for gas discharges would result in  $\sim 0.5\text{-kW/cm}^2$  internal power densities, in the range of conventional cooling technology for dc operation. The cathode gap would have to be increased from the present 4 mm to  $\sim 8$  cm; however, it seems likely that a full scaling would not be necessary for a pulsed source. The present source housing cannot accommodate a large expansion, but cathodes were made with gaps of 2.7, 4.3, 8.4, and 11.3 mm. Although this is not a simple scaling, we found that the required gas pressure varied nearly inversely with this dimension, as expected. Through a 2-mm aperture, 25 mA was extracted, a  $0.8\text{-A/cm}^2$  current density, but electron loading prevented successful extraction with a 5-mm aperture. Because these experiments were carried out on the ATS injector, limited time was available and no further work has been done. From previous work with circular apertures for the early injector configuration of 250 kV, 30 mA, we found that the beam emittances were nearly the same in both planes:  $0.003\pi\text{ cm}\cdot\text{mrad}$  for a 1.5-mm-diam aperture. This simple set of measurements indicates that the basic scaling is sound but that some care is required to maintain proper operation. A cathode gap of at least 4 cm is probably required to get reasonable gas efficiency. A new housing would have to be built, but the present  $90^\circ$  magnet probably could be used. A more attractive long-term goal would be to use PMs for the source field and begin focusing the extracted beam as soon as possible with quadrupoles or a solenoid. From the ion-acoustic model of the plasma oscillations, the scaling would result in oscillation frequencies around 1 to 2 MHz. Understanding and damping of these oscillations might be easier in a large-scale source, but the problem seems likely to be a continuing one.

#### IV. ION SOURCE TEST STAND

Work on the ISTS was carried out (using our original Dudnikov source) to determine parameters, to understand the coherent and noise fluctuations in the source and in the beam, and to make measurements to gain an improved understanding of the source plasma. In addition, a small theoretical effort was devoted to plasma modeling, the conclusion of which was that measurement of the relative spectral intensities from excited states of the hydrogen atoms would probably not be easily related to the translational energies of the atoms. This energy is of interest because the  $H^-$  ions extracted are believed to have the temperature of the atoms and the  $H^-$  emittance is consistent with a 4-eV temperature. Because of the small plasma size, most of the emitted light escapes from the plasma; hence, the intensities reflect the spectrum of electron energies and the excitation cross sections, not the atom energies. The primary production mechanism for excited atomic states is presumed to be from collisions with electrons in the tail of the Boltzman distribution.

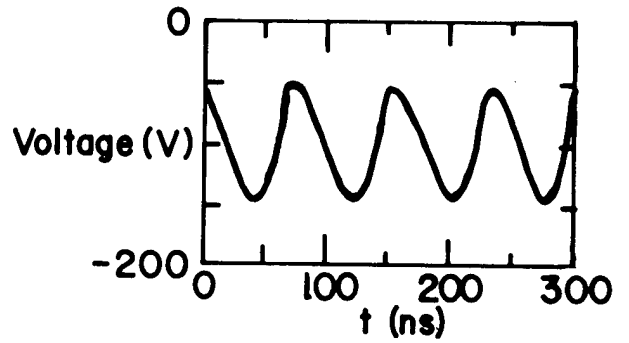
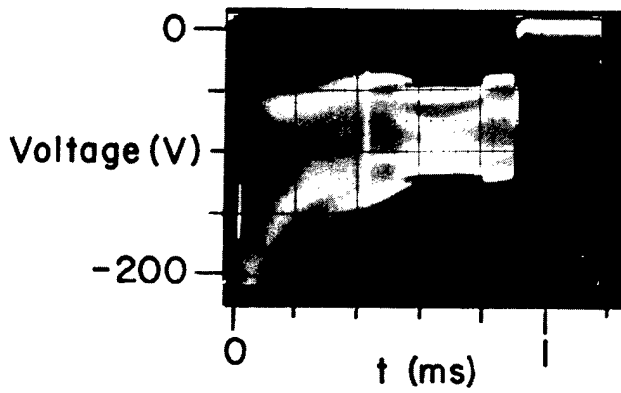
The  $H^-$  ion temperature deduced from an emittance measurement includes the effects of extraction and transport aberrations; however, the deduced temperature should scale with energy for an aberration-dominated system instead of being invariant as for a true temperature. Also, we expect the positive ions to have different temperatures from that of the  $H^-$  ions. We measured the currents and emittances of  $H^+$ ,  $H^-$ ,  $H_3^+$  ions from 4.4 to 13 keV for dc operation so that space-charge forces would be small. The positive currents were mostly  $H^+$  and  $H_3^+$  ions and were approximately the same magnitude as the  $H^-$  current. If the source plasma potential is negative, as suggested by Dudnikov,<sup>7</sup> then the positive ion current at emission would be much less than that in the plasma; therefore, this is probably not an indication of the source-plasma density but indicates that positive ions diffuse outward to maintain neutrality in the  $H^-$  rich plasma. Unfortunately, the emittance data were taken over a period of a few days and had inconsistencies that tended to mask the variations for which we were looking. A tentative conclusion is that our emittance is dominated by aberrations, but this experiment must be more systematically done when the emittance scanner on the test stand is computer automated.

Discharge voltage and current waveforms for the 100-A pulsed discharge have been observed to have large amplitudes of coherent oscillations in the 10- to 20-MHz range (Fig. 27). As reported previously, these oscillations decrease in frequency during the pulse, often in discrete jumps.<sup>6</sup> Primarily they are seen in the voltage, probably because the discharge is driven by a quasi-constant current generator. Only random fluctuations (noise) are seen with a 1-A, dc discharge, but the noise disappears below a critical magnetic field  $B_c$ . The pulsed discharge generally will not operate below this field, but noise decreases as it is approached. The influence of all these oscillations on beam emittance is not fully understood, but previous measurements have shown that the emittance can drop by a factor of 3 when noise is minimized.

The predicted dependence of oscillation frequency on discharge parameters is shown, summarizing the results of an ion acoustic-wave model presented last year (Fig. 28).<sup>8</sup> We examined the frequency dependence on the parameters shown in Fig. 29; the results (Fig. 30) are in reasonable agreement with theory. We have not modeled  $E_{\max}$  theoretically, but the value of  $\sim 10$  eV determined from the formula is in rough agreement with the plasma potential, -20 V, as determined by Dudnikov.<sup>7</sup> There appears to be negligible dependence on  $W$ , the slot width, and on  $B$ , the magnetic field. It is suggested that, with a cylindrically symmetric slot and magnetic field, the oscillations can be suppressed. Emittance measurements will be an important part of this study after upgrading the present equipment to computer control.

To investigate the possibility that source pulsing below  $B_c$  was not possible because of discharge start-up difficulties, a circuit was devised that maintained a 1-A, dc "keep-alive" arc on which a pulse could be superposed. We found that at a field less than  $B_c$ , the pulse current would not exceed more than a few amperes but that high-current operation was possible as usual, above  $B_c$ . A study with hydrogen and deuterium discharges with four different source geometries has shown that  $B_c W / \sqrt{M} = 238$  G·cm within  $\sim 10\%$  for our source, where  $M = 2$  and  $4$ , and  $W$  is the anode width (Fig. 29). This would be consistent with a plasma ion ( $H^+$  or  $D^+$ ) energy of 1.4 eV. Our interpretation is that with a field lower than  $B_c$ , the Larmor radius of the ions is too large for them to return to the cathode; hence, the arc stops. In dc operation at low current, there are probably lower ion energies and different species in the

## Discharge Voltage Waveforms



## Discharge Frequency Spectra

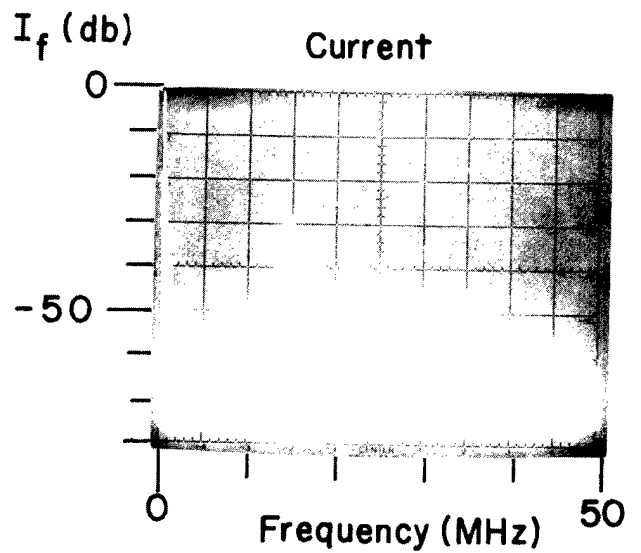
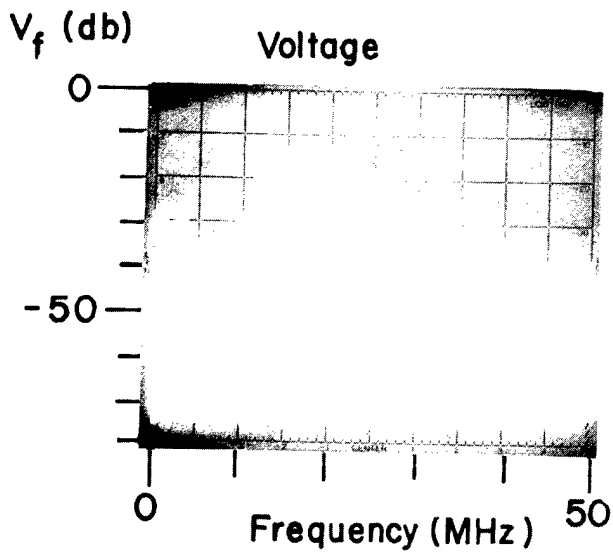
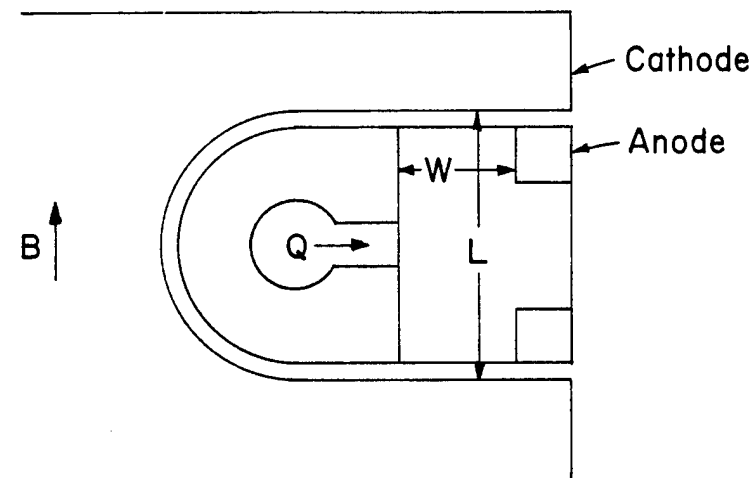


Fig. 27.  
Discharge oscillations study.

$$f = \frac{2n}{L} \sqrt{\frac{E_{\max}}{M}}, \quad \text{where}$$

$f$  = Oscillation frequency  
 $n$  = Integer  
 $E_{\max}$  = Electron energy at the maximum of the electron velocity distribution  
 $L$  = Cathode - Cathode spacing  
 $M$  = Ion mass

Fig. 28.  
Ion acoustic model.



Cross Section of Penning Source

- $L$ , the cathode - cathode spacing
  - $M$ , the ion mass
- Also
- $W$ , the arc slot width
  - $B$ , the magnetic field
  - $Q$ , the discharge gas feed rate ( $H_2$  or  $D_2$ )
  - $I_d$ , the discharge current

Fig. 29.  
Parameters varied in oscillations study.

Parameter	Effect on Oscillation Frequency f	Quantitative Result	
L	Approximate 1/L Dependence	$\frac{1/L, \text{ mm}^{-1}}$ .12 .23 .37	$\frac{f(\text{MHz})}{7.8}$ 13 20
M	Approximate $1/\sqrt{m}$ Dependence	$\frac{1/\sqrt{m}}$ H <sub>2</sub> .707 D <sub>2</sub> .5	$\frac{f(\text{MHz})}{12}$ 10
W	Minimal	$\frac{W(\text{mm})}{2}$ 3	$\frac{f(\text{MHz})}{12.4}$ 12.1
B	Very Weak Dependence	A +29% change in B causes a -2.3% change in f.	
Q	Moderate Dependence	A +53% change in Q causes a -17% change in f.	
I <sub>d</sub>	Moderate Dependence	A -60% change in I <sub>d</sub> causes a +25% change in f.	

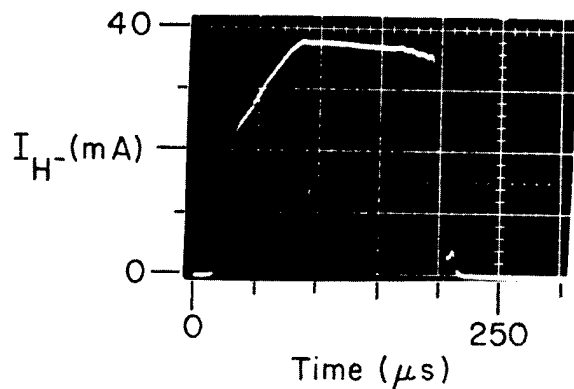
Fig. 30.  
Results of oscillations studies.

plasma. We conclude that the pulsed discharge will not operate at the low field that quiets the dc discharge. Nonetheless, there was substantial reduction in the discharge and beam-current noise near  $B_c$  for the pulse discharge, and the keep-alive circuit made it possible to operate reliably near this field. It was possible to extract a beam with only  $\pm 2\%$  fluctuation in a bandwidth in excess of 10 MHz, substantially less noise than the  $\pm 10\%$  for typical operation (Fig. 31). The discharge voltage still has coherent oscillations; therefore, these have no apparent effect on the current. If the emittance turns out low, then we should try to achieve this operation without the keep-alive circuit so that the injector source can be operated in a similar manner. Without the keep-alive arc, it was possible to produce a pulsed discharge with no coherent oscillation and with low noise over a narrow range of gas flow and magnetic field (Fig. 32). Thus, there are operating regimes for which a promise of lower current fluctuation and beam emittance may be realized.

## V. HIGH-CURRENT TEST STAND

Some source development work has been done during the year on the ATS injector; however, the injector is becoming increasingly devoted to transport and matching studies between the column and the RFQ. The ISTS can be used to continue development and conditioning of parts for the injector, but its power-handling capability is insufficient for dc source development. For these reasons, construction of a high-current test stand (HCTS) has been started so that source discharge power levels of 20 kW, estimated for the rotating ion source (RIS) or a cusped-field source (CFS), are available at 30-kV potential. The basic capabilities of the HCTS, as determined by equipment now on hand, are given in Fig. 33. The isolation transformer is a standard design for 250-kV isolation, 50-kVA power, and it costs little more than a lower voltage unit; however, it can also be used as a spare for the ATS injector transformer. Many of the components for the HCTS are on hand (Fig. 34) as a result of purchases and surplus acquisitions. The floor plan is shown in Fig. 35, and a recent photograph of the installation is shown in Fig. 36. Further work on the HCTS has been delayed pending further funding.

USED A DC "KEEPER" ARC TO PRODUCE QUIET ( $\leq 2\%$  FLUCTUATIONS)  $H^-$  CURRENT PULSES NEAR THE CRITICAL MAGNETIC FIELD  $B_C$ . NORMALLY HAVE  $\pm 10\%$  FLUCTUATIONS.



PULSED CURRENT	80 A
DC CURRENT	1 A
B	1100 G
GAS FLOW	125 STD $CM^3/MIN$
EXTRACTION VOLTAGE	11 kV

$\pm 80$  V, 17 MHz COHERENT OSCILLATIONS ON VOLTAGE PULSE.

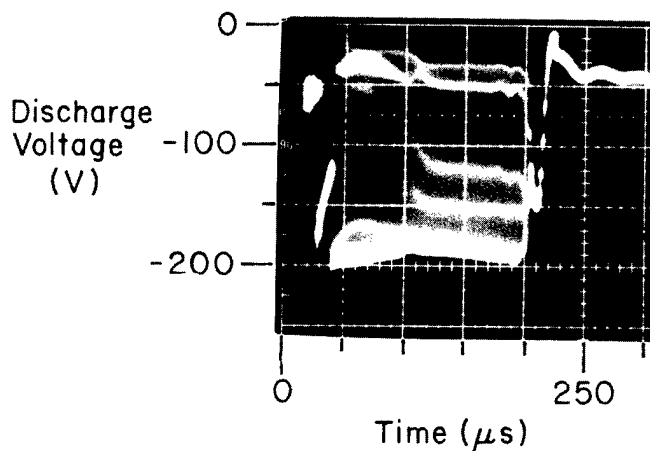
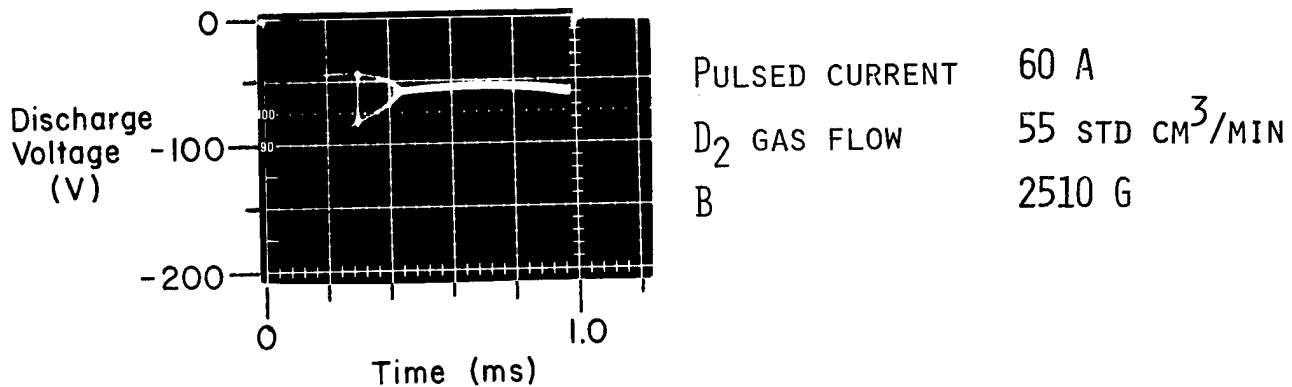


Fig. 31.  
Production of quiet  $H^-$  current pulses near the critical magnetic field.

HAVE PRODUCED PULSED DISCHARGES WITHOUT NOISE OR COHERENT OSCILLATIONS (NO "KEEPER" ARC) - VOLTAGE FLUCTUATIONS LESS THAN  $\pm 5\%$  FOR LAST 550  $\mu\text{s}$  OF PULSE.



FOR  $\text{H}_2$  THERE IS A NARROW BAND OF GAS FLOW (70 - 100 SCCM) AND MAGNETIC FIELD (1410 - 1850 G) WHERE THE QUIET VOLTAGE PULSE WILL RUN.

WORK IN PROGRESS TO UNDERSTAND PRODUCTION OF QUIET DISCHARGES AND TO MEASURE THE RESULTING  $\text{H}^-$  BEAM EMITTANCE.

Fig. 32.  
 Production of quiet discharge-voltage pulses.

- $\text{H}^-$  CURRENT - 100 mA, 100% Duty Factor  
 (limited by power supplies  
 and cooling considerations)
- POWER - 50 kVA (limited by isolation transformer)
- GAS FLOW - 2 torr  $\cdot$   $\ell/\text{s}$  (limited by pumps)
- VOLTAGE - 30 kV (limited by power supply)

Fig. 33.  
 The HCTS design features.

ON HAND

- Diffusion Pump System (10,000  $\ell/s$  for  $H_2$ )
- Isolation Transformer (50 kVA, 250 kV)
- Extraction Power Supply (30 kV, 500 mA)
- Arc Power Supply (250 V, 50 A)
- Some Electronics Modules
- Electronics Racks, HV Cage, and Support Stand

Fig. 34.  
The HCTS status.

TO BE PROCURED

- Valve - Baffle Combination
- Vacuum Box
- Diagnostics
- Other Electronics Modules and Power Supplies

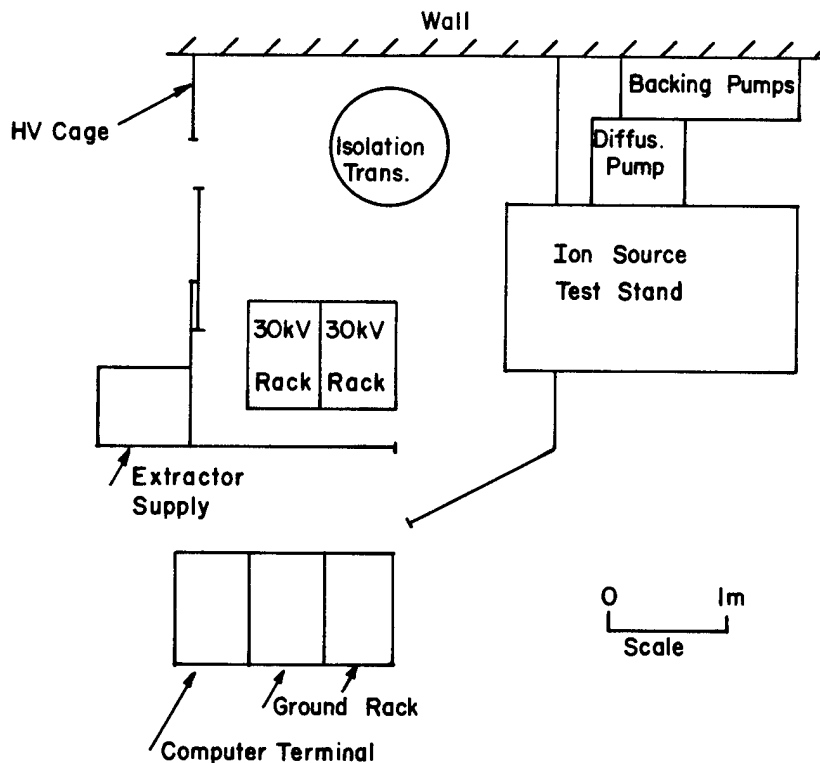


Fig. 35.  
Plan view of the HCTS.



Fig. 36.  
Photograph of the HCTS.

## VI. CONSIDERATIONS FOR A dc SOURCE

In the original concept of the RIS, it was assumed that the asymmetry in emittance of a beam extracted from a slit emitter could be preserved and that the resulting useful brightness would be inversely proportional to  $\epsilon_x \epsilon_y$ . The RIS uses rotating electrodes to spread discharge power density, estimated to be  $10 \text{ kW/cm}^2$  pulsed in the Dudnikov source, over the electrode's periphery and to keep average heat loads under  $1 \text{ kW/cm}^2$ . A localized magnetic field keeps the discharge confined to a peripheral distance of  $\sim 1$  to  $2 \text{ cm}$ , determined by the magnetic pole separation, which must be somewhat larger than the cathode gap. Although this seems reasonable for a slit beam, the power efficiency would be much less for a circular beam because the cathode gap must be increased, thus spreading the discharge peripherally while simultaneously a smaller peripheral region is being used for ion extraction. Inevitable coupling of the x- and y-planes as the beam is propagated has led us to conclude that a circular aperture should be used for the brightest beam with the minimum current density. With the present emittance goal, the projected power density in the source is reduced from previous requirements; therefore, a large-scale version of the Dudnikov source could approach the dc goal.

Elsewhere, development of other sources with focusing cathodes (self-extraction) has led to substantial improvement in their power efficiencies over the past few years. Last year we tested a grooved magnetron source on loan from Brookhaven National Laboratory because it had a possibility of meeting our dc goal; however, the emittance we measured was much larger than could be accounted for by elementary source considerations. This large emittance was attributed to source-plasma oscillations, which were much higher than for the Dudnikov source. At present we do not have a specification for the allowable amplitude and frequency of current fluctuations; if fluctuations must be kept under a few per cent, it may be necessary to use a source with no magnetic field, one successful version of which is the CFS.

The CFS developed by Leung and Ehlers has produced a quiescent 1-A, dc  $\text{H}^-$  beam over a large area, the current at the converter surface having a density of  $\sim 10 \text{ mA/cm}^2$ .<sup>9</sup> This can be focused to higher density for extraction, but the sputter energy at the converter would have to be low to produce a beam of sufficiently low emittance. This sputter energy is not known, but there is evidence that it is 1 to 5 eV. By collimating the converter-produced beam at

extraction, it is possible to reduce the emittance, as has been done for LAMPF for a pulsed 10- to 20-mA version of the CFS. In its present state of development, this type of source could probably produce 25 mA dc within our emittance requirement.

To increase the current, the plasma density might be increased. This would require better cooling, more efficient magnetic confinement, and longer filament lifetime. Use of a larger converter and more collimation also would help. With a larger converter, enough primary electrons might be produced to solve the filament problem. There is much to be learned about this source, including the sputter energy and its dependence on operating parameters, optimum coating of cesium on the converter, and optimum converter voltage. An interesting question is whether, as a pulsed source (for which heating limitations can be overcome), a quiescent beam of adequate current can be extracted. It may be possible to examine this possibility with the LAMPF source. Development of a suitable dc source can be carried out on our HCTS, now partially completed.

#### REFERENCES

1. D. G. Dzhabbarov and A. Naida, "Spatial Development of the Instability of a Dense Beam of Negative Ions in a Rarefied Gas," Inst. of Physics, Ukrainian Academy of Sciences, Zh. Eksp. Teor. Fis. 78., p. 2259 (June 1980).
2. A. J. T. Holmes, "Theoretical and Experimental Study of Space Charge in Intense Ions Beams," Phys. Rev. A, Vol. 19, No. 1, p. 389 (January 1979).
3. W. S. Cooper, K. Halbach, and S. B. Magyary, "Computer-Aided Extractor Design," Proc. 2nd Symp. Ion Sources and Formation of Ion Beams, Berkeley, California, October 22-25, 1974, p. II-1.
4. J. H. Whealton, "Ion Extraction and Optics Arithmetic," Nucl. Instrum. Methods 189, No. 1, p. 1 (October 1981).
5. Jack E. Boers, "SNOW - A Digital Computer Program for the Simulation of Ion Beam Devices," Sandia National Laboratories report SAND-79-1027 (August 1980).
6. Robert G. Wilson and George R. Brewer, Ion Beams with Applications to Ion Implantation (John Wiley & Sons, New York, 1973).

7. V. G. Dudnikov, E. G. Obrazovskii, and G. I. Fiksel, "Emission Properties of the Electrodes of Surface-Plasma Sources and Efficiency of H<sup>-</sup> Production," Inst. Nucl. Physics, Siberian Branch, Academy of Sciences of the USSR, Fiz. Plazmy 4, p. 662 (May-June 1978).
8. Accelerator Technology Division, "1981 White Horse Progress Report" (to be published as a Los Alamos National Laboratory LA-series report).
9. K. N. Leung and K. W. Ehlers, "LBL Self-Extraction Negative Ion Source," Lawrence Berkeley Laboratory report LBL-13261 (August 1981).

## RFQ TUNING

### I. INTRODUCTION

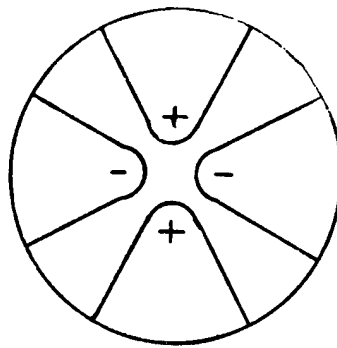
The tuning of the ATS RFQ has been the proving ground for substantial development of tuning techniques. Difficulties in tuning this structure have led to advances in our understanding the effect of tuning errors on the azimuthal and longitudinal field distributions of RFQ structures and in our ability to determine the adjustments required to correct the field distributions. We conclude that shorter or modified structures are needed to achieve the ATS performance goals.

Here we discuss the current state of knowledge about RFQ tuning; these principles then are related to the tuning goals for high-frequency RFQ structures. A transmission-line model is used to calculate field distributions for structures with position-dependent parameters and is used to determine these parameters, given the measured field distribution. The model is expanded to illustrate how azimuthal and longitudinal effects are taken into account. Data illustrating how this information has been used in tuning the ATS RFQ are presented. A brief account of how geometrical parameters are related to the model parameters is given, an analysis that permits RFQ tuning adjustments to be predicted from the field-distribution data. Data from such measurements for the ATS RFQ are presented. Finally, techniques for improving the performance of long RFQ structures are reviewed, and the techniques considered to be the most fruitful are discussed.

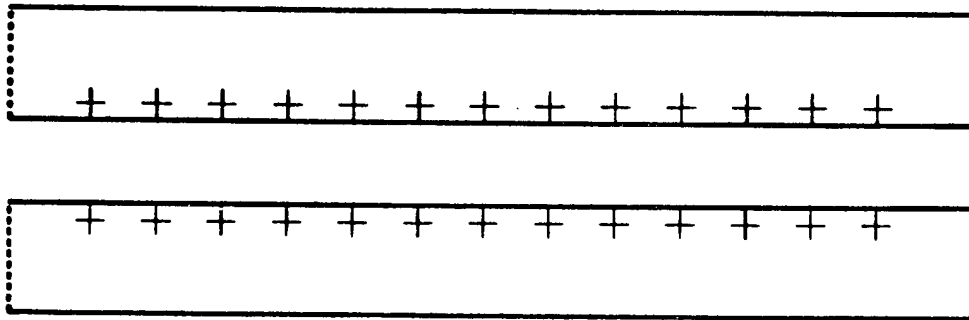
### II. RFQ DESIGN PRINCIPLES AND TUNING GOALS

Figure 37 represents the most essential features of the RFQ structure. For designing the vane-tip profiles for beam-dynamics considerations, we assume the vane tips to be equipotential surfaces with quadrupolar symmetry; thus, the fundamental tuning goals are to give the vane tips these assumed characteristics.

Some compromise is required at this point because the RFQ is an rf system and not an electrostatic system. Furthermore, the vane tips are not hyperbolic



AZIMUTHAL CROSS SECTION



LONGITUDINAL CROSS SECTION

Fig. 37.  
RFQ schematic representation.

surfaces. Therefore, tuning requirements are reduced to requiring a constant potential along the center of the vane tips and to requiring 90° rotational symmetry of the field amplitudes, with the sign of the potential alternating on adjacent vane tips.

### III. ERROR ANALYSIS

#### A. The Transmission-Line Model

Figure 38 shows an infinitesimal element of an RFQ structure's two-port transmission-line representation. The series impedance per unit length  $Z$  and shunt admittance per unit length  $Y$  are derivable from Maxwell's equations.

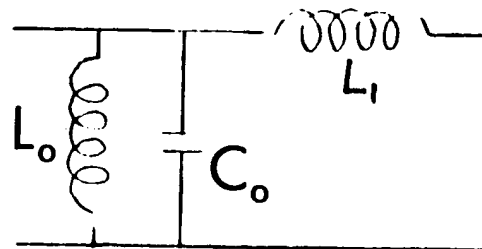


Fig. 38.  
An infinitesimal element of the transmission-line model for the RFQ of length  $\delta x$ .

For simplicity, however, we will postulate inductances and capacitances, the exact values of which will vanish from the calculated results.

For a TE mode, we can take  $Z = j\omega L_1$  and  $Y = j\omega C_0 + 1/j\omega L_0$  in the lossless case as shown in Fig. 38. The transmission-line equations for a uniform cross-section structure are

$$\frac{dV}{dx} = ZI \quad ,$$

$$\frac{dI}{dx} = YV \quad ,$$

$$\frac{d^2V}{dx^2} = YZV \quad ,$$

and

$$YZ = \frac{L_1}{L_0} \left( 1 - \frac{\omega^2}{\omega_0^2} \right) = \gamma^2 = \frac{\omega_c^2}{c^2} \left( 1 - \frac{\omega^2}{\omega_0^2} \right) \quad ,$$

where

$$\omega_0 = (L_0 C_0)^{-1/2} \quad .$$

We can relate the parameters to properties of a distributed system such as a high-frequency RFQ structure by the following expressions:

$$\omega_0 = \omega_c \quad ,$$

and

$$\frac{L_1}{L_0} = \frac{\omega_c^2}{c^2} \quad .$$

The wave equation may be rewritten

$$\frac{d^2V}{dx^2} - \gamma^2 V = 0 \quad .$$

If we assume a power-series solution of the form

$$V = V_0 \left( 1 + \sum_{n=1}^{\infty} r_n x^n \right) \quad ,$$

we get the recursion relations

$$r_2 = \frac{1}{2} \gamma^2 \quad ,$$

and

$$r_{n+2} = \frac{\gamma^2 r_n}{(n+1)(n+2)} \quad \text{for } n \geq 1 \quad .$$

If we assume the resonant frequency of the structure  $\omega$  is equal to the cutoff frequency of the structure  $\omega_0$ , then  $\gamma = 0$  and all coefficients of the power series vanish, except for the constant and the linear coefficients.

The solution to the wave equation then is  $V = V_0(1 + r_1 x)$ . We can calculate the impedance at the end points using the relation

$$I = \frac{1}{Z} \frac{dV}{dx} \quad .$$

The required terminating impedances  $Z_0$  and  $Z_\ell$  are

$$Z_0 = \frac{V(0)}{I(0)} = \frac{Z}{r_1} \quad \left(\text{or } r_1 = \frac{Z}{Z_0}\right) ,$$

and

$$Z_\ell = -\frac{V(\ell)}{I(\ell)} = -\frac{V_0(1 + r_1\ell)}{V_0 r_1 / Z} = -\frac{Z}{r_1} (1 + r_1\ell) .$$

Thus, we have  $Z_\ell = -(Z_0 + Z\ell)$ . If  $Z_0 \rightarrow \infty$ , then  $Z_\ell \rightarrow -\infty$ , and  $r_1 \rightarrow 0$ . So we see that if the terminating impedances are made arbitrarily large, that is, open circuits, the field distribution must be constant, independent of position. To avoid getting bogged down in a discussion of fringe-field effects near the vane ends, the structure's end terminals are assumed to be outside the fringe-field region (Fig. 39). The remaining portions of the structure, fringe fields and all, are considered to be the end terminations. The tuning capacitors at each end serve to adjust the terminating impedances to the required values.

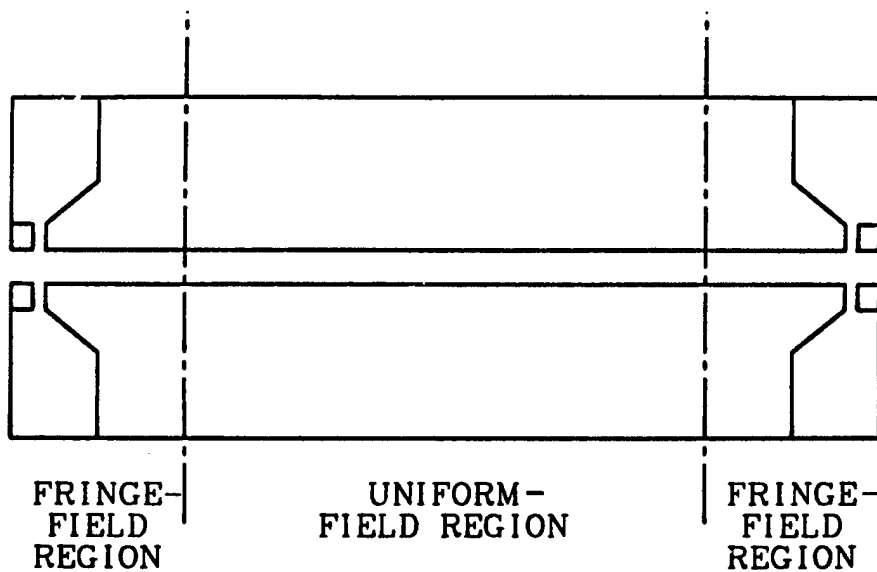


Fig. 39.  
Termination of the  
RFQ uniform-field  
region.

If the terminating impedances are finite but the same at each end, the field distribution will vary with  $x$  according to the equations

$$V = V_0 \frac{\cosh \gamma (x - l/2)}{\cosh \gamma l/2}$$

below cutoff, where  $\omega < \omega_0$ ,  $\gamma$  is real, and

$$V = V_0 \frac{\cos \beta (x - l/2)}{\cos \beta l/2}$$

above cutoff, where  $\omega > \omega_0$  and  $\gamma = j\beta$ . Note that above the cutoff frequency, the field peaks in the middle; whereas below cutoff, the field at the center reaches a minimum. This characteristic is useful experimentally as a guide to adjusting the end tuners.

### B. Predicting Field Distributions

The procedures developed above can be extended to determine the field distribution for a structure with  $x$ -dependent parameters. For simplicity we assume that the position dependence is in the shunt capacitance. Relaxing this restriction does not substantially affect the conclusions drawn here. The power-series expansion of the capacitance variation is given by

$$C(x) = C_0 \left( 1 + \sum_{n=1}^{\infty} \delta_n x^n \right) .$$

The wave equation for the voltage distribution is the same as before, except that now the propagation "constant" is a function of  $x$ :

$$\frac{d^2 V}{dx^2} = Y(x)ZV \quad ,$$

where

$$Y(x)Z = \frac{\omega_0^2}{c^2} - \frac{\omega^2}{c^2} \left( 1 + \sum_{n=1}^{\infty} \delta_n x^n \right) .$$

If we again assume a power-series solution of the form

$$V = V_0 \left( 1 + \sum_{n=1}^{\infty} r_n x^n \right) ,$$

we get the recursion relations

$$r_2 = \frac{1}{2} \left( \frac{\omega^2}{c^2} - \frac{\omega_0^2}{c^2} \right) = \frac{1}{2} \gamma^2 ,$$

$$r_3 = \frac{1}{6} \gamma_0^2 r_1 - \frac{1}{6} \frac{\omega^2}{c^2} \delta_1 ,$$

and

$$r_{n+2} = \frac{1}{(n+1)(n+2)} \left[ \gamma_0^2 r_n - \frac{\omega^2}{c^2} \left( \delta_n + \sum_{m=1}^{\infty} r_m \delta_{n-m} \right) \right] \quad \text{for } n \geq 2 .$$

As an example, we consider a linear capacitance variation. If the structure is excited at the cutoff frequency of the  $x = 0$  end, with an open circuit termination at  $x = 0$  and with whatever impedance is required to make the structure resonant at the excitation frequency at the other end, the recursion relations reduce to

$$r_1 = 0 \quad ,$$

$$r_2 = 0 \quad ,$$

$$r_3 = -\frac{1}{6} \frac{\omega_0^2}{c^2} \delta_1 \quad ,$$

and

$$r_{n+2} = -\frac{1}{(n+1)(n+2)} \frac{\omega_0^2}{c^2} \delta_1 r_{n-1} \quad .$$

To first order in  $\delta_1$ , the voltage distribution is

$$V = V_0 \left( 1 - \frac{1}{6} \frac{\omega_0^2}{c^2} \delta_1 x^3 \right) \quad ,$$

where

$$\frac{c}{\omega} = \lambda = \lambda / 2\pi \quad .$$

The end-to-end voltage difference given by  $\delta V / V_0$  is

$$\frac{\delta V}{V_0} = -\frac{1}{6} \frac{\ell^2}{\lambda_0^2} \frac{\delta C}{C} \quad ,$$

in terms of the end-to-end capacitance variation  $\delta C / C = [C(\ell) - C(0)] / C(0)$ .

The most significant thing to notice about this calculation is that, for a given capacitance error, the voltage error goes as the square of the ratio of

the structure length to the operating wavelength. An RFQ structure is considered to be "long" in the sense of being difficult to tune when its length exceeds 1.5 free-space wavelengths. The ATS RFQ is quite long: its length is nearly 4 free-space wavelengths at 425 MHz.

For the ATS RFQ we have  $l \approx 2.8$  m, and  $f_0 \approx 425$  MHz. This gives  $(l/\lambda)^2 \sim 600$ . If we assume the capacitance to be inversely proportional to the gap  $g$ , we get

$$\frac{\delta V}{V} \approx 100 \frac{\delta g}{g} .$$

If  $g \approx 0.1$  in. and we require  $\delta V/V < 0.1$ , we must have  $\delta g < 10^{-4}$  in.

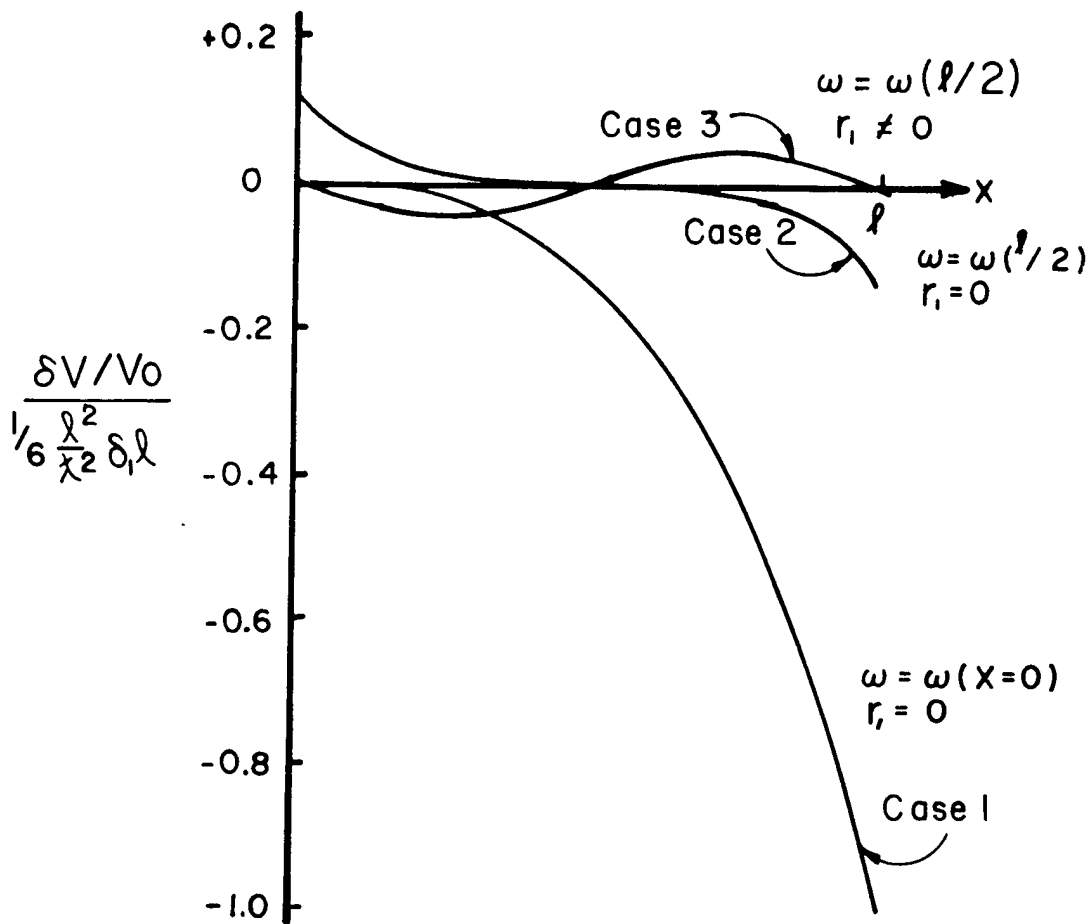
In Fig. 40 we illustrate the improvement that can be obtained by using the end tuners to adjust the operating frequency to be the frequency at the center of the structure. This reduces the overall field error by a factor of 4. Adjusting the symmetry of the end terminations can further reduce the magnitude of the field deviation, for a net improvement factor of 10. This improvement is somewhat misleading, however. If the average vane-to-vane gap were to change somehow by 0.0001 in., the field error could be as bad as before.

#### IV. DATA ANALYSIS

Leaving the question of mechanical stability, we return to the wave equation. Now we invert the analysis. Instead of asking for the field distribution for  $x$ -dependent parameters, we ask for the  $x$  dependence of the parameters given the measured field distribution. Because the structure has already solved the wave equation for us, this is a very simple question to answer.

Recall the wave equation

$$\frac{d^2 V}{dx^2} - \gamma^2(x)V = 0 .$$



IMPROVEMENT  
FACTOR  
 $\frac{(\delta V_{\max} - \delta V_{\min})}{V_0 \frac{1}{6} \frac{\ell^2}{\lambda^2} \delta_l \ell}$

Case 1	1.0
Case 2	0.25
Case 3	0.096

Fig. 40.  
Relative amplitude error versus position for linear capacitance error and various tuning conditions.

Solving for  $\gamma^2(x)$ , knowing  $V(x)$ , we get

$$\gamma^2(x) = \frac{1}{V} \frac{d^2V}{dx^2} .$$

If we take  $\omega = \omega_0 + \delta\omega$ , using

$$\gamma^2 = \frac{\omega_0^2 - \omega^2}{c^2} ,$$

we get an approximation for  $\gamma^2$

$$\gamma^2 \approx -2 \frac{\delta\omega}{\omega} \frac{1}{\lambda^2} .$$

Thus we can relate the frequency error  $\delta\omega/\omega$  to the observed voltage distribution:

$$\frac{\delta\omega}{\omega} = -\frac{\lambda_0^2}{2} \frac{1}{V} \frac{d^2V}{dx^2} .$$

In the approximation where the capacitance varies inversely as the vane-to-vane gap, we can relate the frequency error  $\delta\omega/\omega$  to the average gap error  $\delta g/g$ :

$$\frac{\delta\omega}{\omega} \approx -\frac{1}{2} \frac{\delta g}{g} ,$$

yielding an approximate expression for the average gap error:

$$\frac{\delta g}{g} \approx \lambda_0^2 \frac{1}{V} \frac{d^2 V}{dx^2} .$$

This is a very useful guide, telling us where along the structure the average gap should be changed. The gap also can be adjusted uniformly along the length of the structure to vary the frequency at which a flat field distribution occurs.

Adjusting the average gap is not the only way to tune the structure. More complete analysis shows that the same results can be obtained by varying the structure's shunt inductance. In addition, it is not essential that the tuning be done continuously along the structure's length. It is sufficient to distribute the tuning corrections in discrete packages along the structure, providing the packages are close enough together. For practical purposes "close enough" can be taken to mean  $\sim 0.5$  free-space wavelength apart.

#### A. Data Acquisition

Information about the RFQ field distribution is obtained by the perturbation method. The frequency change produced by a metal plunger inserted radially into the magnetic field of each quadrant, for a series of positions along the length of the structure, is taken as a measure of the square of the magnetic field. The magnetic field can be related to the vane-to-vane potential difference, with sufficient accuracy for tuning purposes. It is not necessary to convert the magnetic-field data to vane-potential data. The quadrupole component of the magnetic-field data is the same as the quadrupole component of the vane-tip potential. The dipole components of the magnetic-field data are equivalent to dipole components of the potential data for a different basis; that is, the  $+0-0$  component of the magnetic field is equivalent to the  $++--$  mode of the potential, and the  $0+0-$  component of magnetic field corresponds to the  $+-+-$  mode of the potential. The choice of basis for the dipole modes is arbitrary; therefore, the analysis can be applied to the magnetic-field data directly, with the interpretation of results modified by the above equivalence.

To estimate the average gap error, the quadrupole components of the data  $A_q(x)$  are calculated for each value of  $x$ , using the expression

$$A_q(x) = \frac{A_1 - A_2 + A_3 - A_4}{4} ,$$

where

$$A_1 = \sqrt{\delta f_1} ,$$

$$A_2 = -\sqrt{\delta f_2} ,$$

$$A_3 = \sqrt{\delta f_3} , \text{ and}$$

$$A_4 = -\sqrt{\delta f_4} .$$

The quadrupole components then are fitted to the Fourier series

$$A_q = C_0 + C_1 \cos v + C_2 \cos 2v + C_3 \cos 3v + \dots \\ + S_1 \sin v + S_2 \sin 2v + S_3 \sin 3v + \dots ,$$

where  $v = \pi(x/\ell - 1/2)$ . The fundamental half-period for the structure is taken to be the length of the vane bases, not the vane tips, because this is the length of the uniform part of the structure (ignoring fringing fields and vane modulation). Figure 41 shows a computer plot of the estimated average gap error for the ATS RFQ.

### B. Azimuthal Asymmetry

Figure 42 shows an ad hoc model for interpreting the cause of azimuthal field-distribution asymmetries. The principal modes of the RFQ (the quadrupole and the two dipole modes) are represented by the transmission-line models. In the absence of azimuthal asymmetry, these modes would be independent. But, we can interpret azimuthal field-distribution errors as arising from a mixing of these modes. The coupling of the modes is represented by mutual admittances. Although these couplings are postulated ad hoc, it is possible to relate the coupling factors to geometrical asymmetries of the structure in a rigorous way.

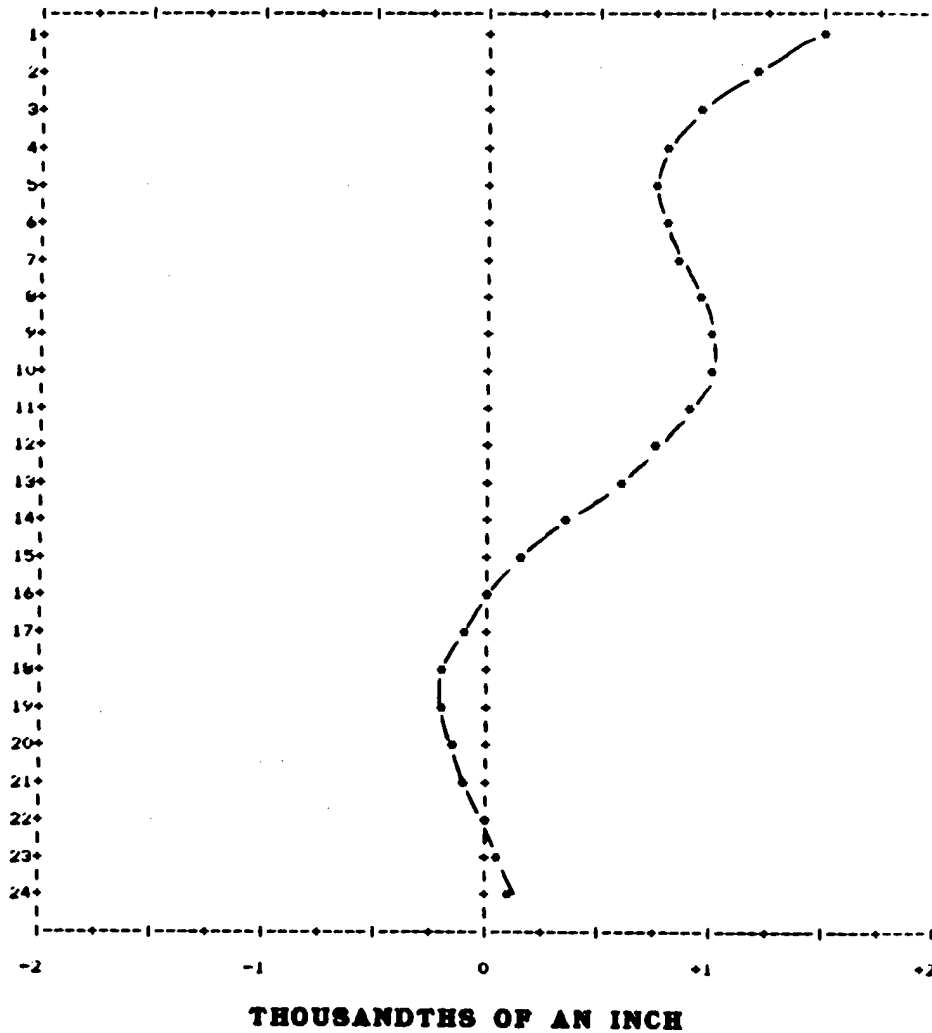


Fig. 41.  
The ATS RFQ average gap error versus position.

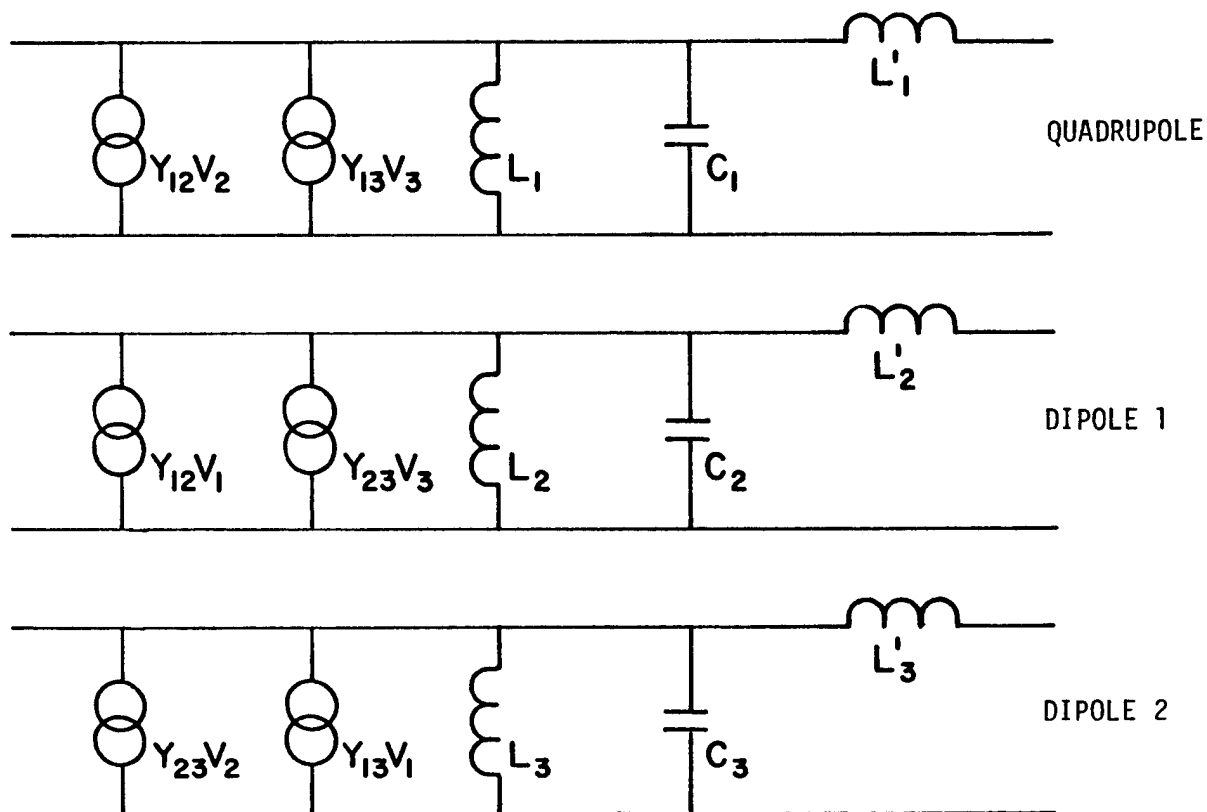


Fig. 42.  
Ad hoc model for RFQ mode mixing.

The field distribution for each measured mode is considered to be a sum of quadrupole and dipole components. For one mode, say the structure's lowest frequency quadrupole-like mode, we can write a set of three coupled-wave equations:

$$\frac{d^2 V_i}{dx^2} = Y_i Z_i V_i + Y_{ij} Z_i V_j + Y_{ik} Z_i V_k \quad .$$

These equations cannot be inverted directly to get the structure parameters as a function of position because there are more parameters than

there are equations. However, if we also obtain data on the two lowest lying dipole-like modes, we can then write a set of nine coupled-wave equations:

$$\frac{d^2 V_i^\ell}{dx^2} = Y_i Z_i V_i^\ell + Y_{ij} Z_j V_j^\ell + Y_{ik} Z_k V_k^\ell \quad ,$$

where  $V_i^\ell(x)$  is the amplitude of the  $i$ th component of the  $\ell$ th mode,  $i, j, k = 1, 2, 3$  with  $i \neq j \neq k$ , and  $\ell = 1, 2, 3$ .

The nine equations split into three sets of three coupled-wave equations in three unknowns:

$$\frac{d^2 V_i^\ell}{dx^2} = -\frac{2}{\lambda_\ell^2} \frac{\delta\omega_i}{\omega_i} V_i^\ell - \frac{1}{\lambda_\ell^2} k_{ij} V_j^\ell - \frac{1}{\lambda_\ell^2} k_{ik} V_k^\ell \quad ,$$

where we have taken

$$Y_{ij} = j\omega C_{ij} \quad ,$$

$$k_{ij} = \frac{C_{ij}}{\sqrt{C_i C_j}} \quad ,$$

and

$$\omega_\ell = \omega_i + \delta\omega_i \quad .$$

Each of the sets of equations can be inverted to give the position dependence of the average gap for each mode and the position dependence of the coupling factors to the other two modes. The equations for determining the parameters for the quadrupole mode are, in matrix form,

$$\begin{pmatrix} v_1^1 & v_2^1 & v_3^1 \\ v_1^2 & v_2^2 & v_3^2 \\ v_1^3 & v_2^3 & v_3^3 \end{pmatrix} \begin{pmatrix} 2 \frac{\delta\omega_1}{\omega_1} \\ k_{12} \\ k_{13} \end{pmatrix} = \begin{pmatrix} -\lambda_1^2 \frac{d^2 v_1^1}{dx^2} \\ -\lambda_2^2 \frac{d^2 v_1^2}{dx^2} \\ -\lambda_3^2 \frac{d^2 v_1^3}{dx^2} \end{pmatrix}$$

The matrix  $V(x)$  is inverted at each value of  $x$ , supplying  $v_i^l(x)$  and  $d^2 v_1^l/dx^2$  from data fits, to calculate the average gap error  $\delta g(x)/g = -2[\delta\omega_1(x)/\omega_1]$  and the dipole-mode coupling factors  $k_{12}(x)$  and  $k_{13}(x)$ .

Figures 43 and 44 are plots of the quadrupole-mode to dipole-mode coupling factors versus position for the ATS RFQ. The two pairs of plots correspond to two different-basis vectors for the dipole modes. The curve labeled S on Fig. 44 is, for example, half of the point-by-point sum of Curves 1 and 2 from Fig. 43.

## V. THE 2N-PORT NETWORKS

To relate the RFQ structure's geometrical properties to the coupling factors postulated above, it is necessary to expand the transmission-line model into a multiport network. Expanding the concepts for two-port networks to 2N-port networks, we define two  $N \times N$  matrices:  $Z$ , the series impedance per unit length and  $Y$ , the shunt admittance per unit length. The voltage  $V$  and current  $I$  are  $N$ -vectors. The  $2N \times 2N$  matrix for an infinitesimal element of length  $\delta x$  is

$$M = \begin{pmatrix} 1 & Z\delta x \\ Y\delta x & 1 \end{pmatrix},$$

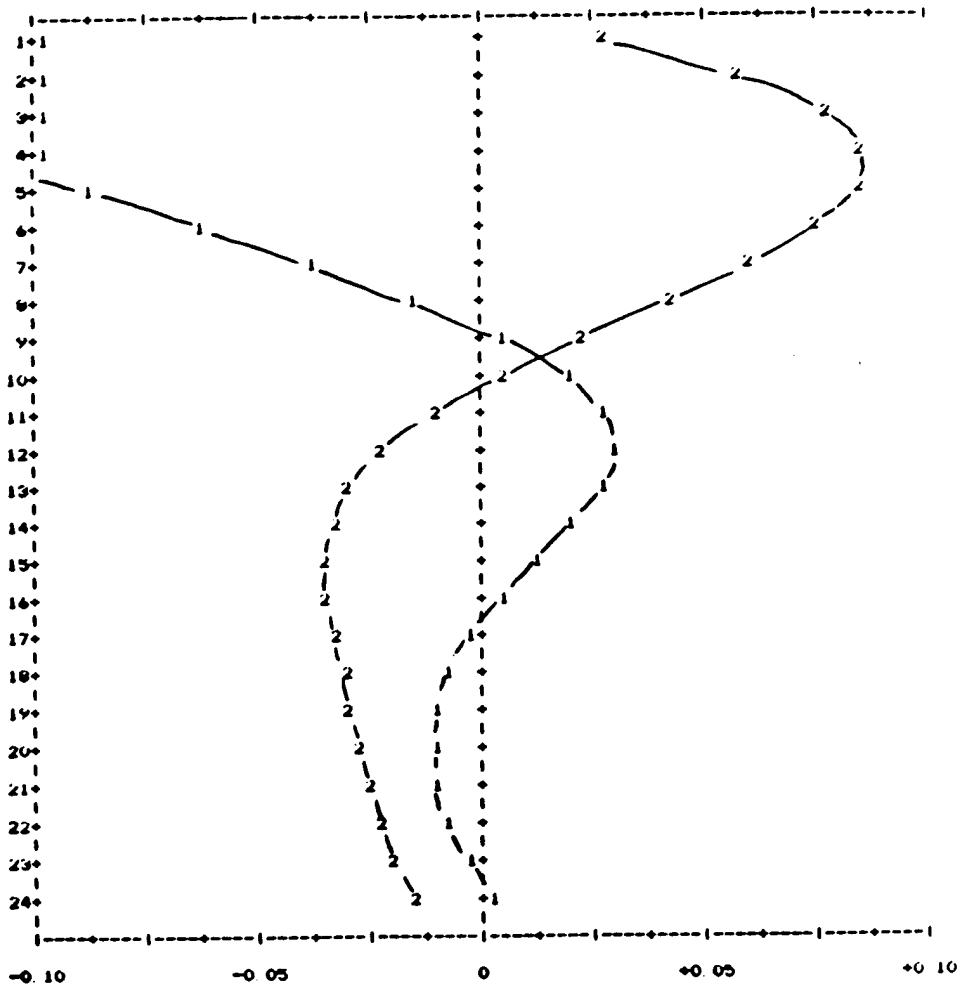


Fig. 43.  
Relative coupling to the dipole modes +0-0 and 0+0-.

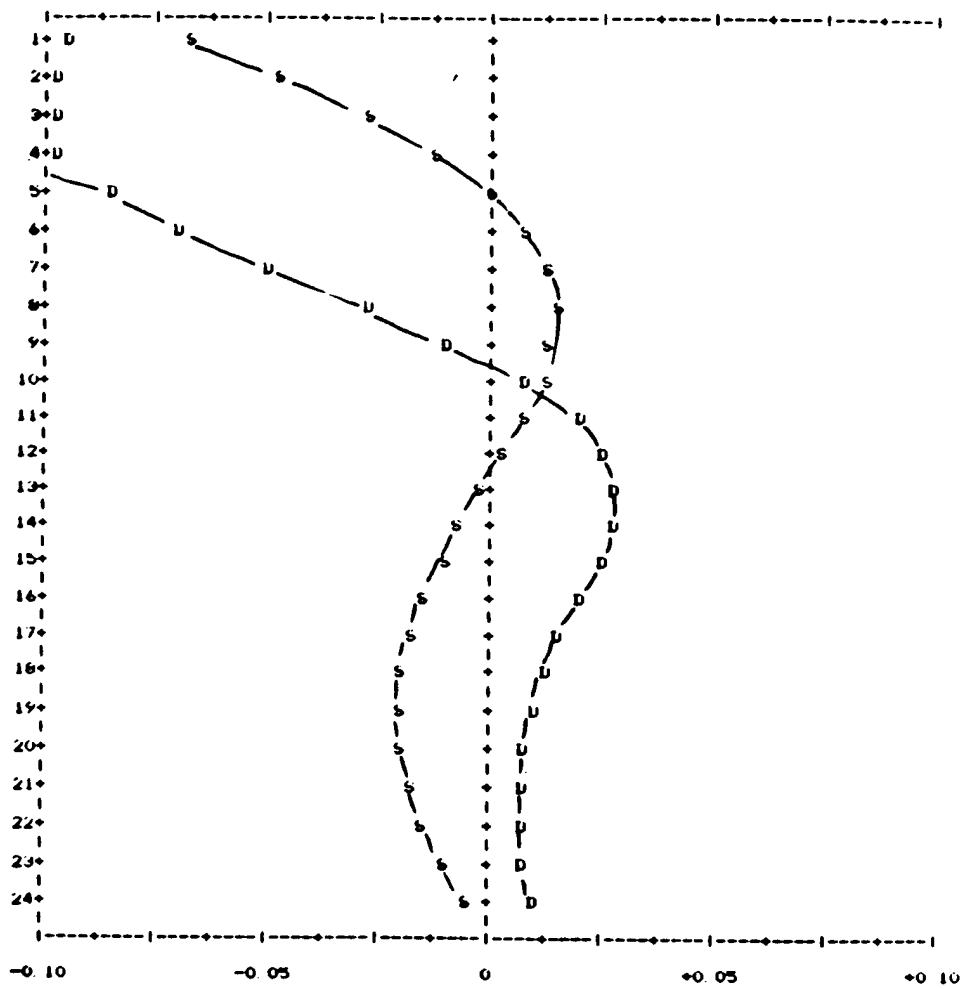


Fig. 44.  
Relative coupling to the dipole modes ++-- and +--+.

and the chain-matrix equation relating the currents and voltages at the input ports to the currents and voltages at the output ports is

$$\begin{pmatrix} V' \\ I' \end{pmatrix} = M \begin{pmatrix} V \\ I \end{pmatrix} .$$

These equations can be expressed as the matrix transmission-line equations:

$$\frac{dV}{dx} = ZI \quad ,$$

$$\frac{dI}{dx} = YV \quad ,$$

or as the matrix wave equation:

$$\frac{d^2V}{dx^2} = ZYV \quad .$$

Figures 45 and 46 illustrate the suggested models for the infinitesimal shunt and series elements representing the continuous part of an RFQ structure.

Note that the structure is treated as an eight-port network. Although it is possible to consider it as an eight-terminal (six-port) network, the relation of the vane-tip potentials is more readily perceived in the eight-port model. The  $2N$ -port matrix equation can be transformed to the mode basis, using the similarity transforms  $S$  for the voltages and  $T$  for the currents:

$$\begin{pmatrix} S & 0 \\ 0 & T \end{pmatrix} \begin{pmatrix} V' \\ I' \end{pmatrix} = \begin{pmatrix} S & 0 \\ 0 & T \end{pmatrix} \begin{pmatrix} 1 & Z\delta x \\ Y\delta x & 1 \end{pmatrix} \begin{pmatrix} S^{-1} & 0 \\ 0 & T^{-1} \end{pmatrix} \begin{pmatrix} S & 0 \\ 0 & T \end{pmatrix} \begin{pmatrix} V \\ I \end{pmatrix} \quad ,$$

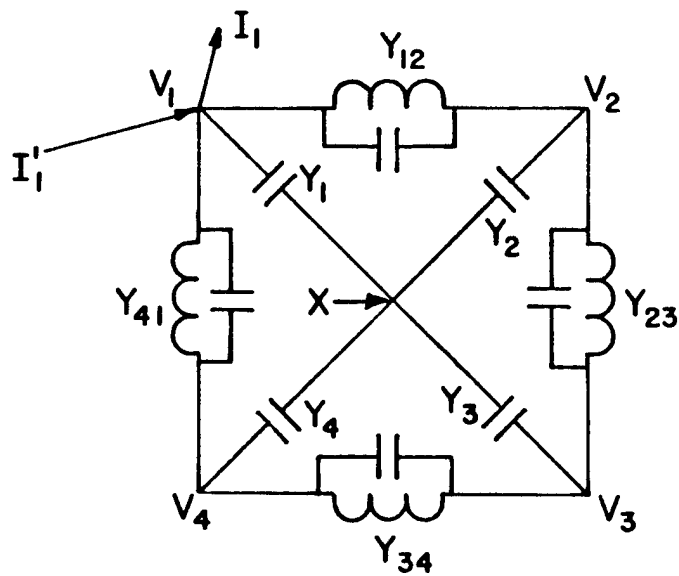


Fig. 45.  
Model for the RFQ's infinitesimal shunt-admittance element.

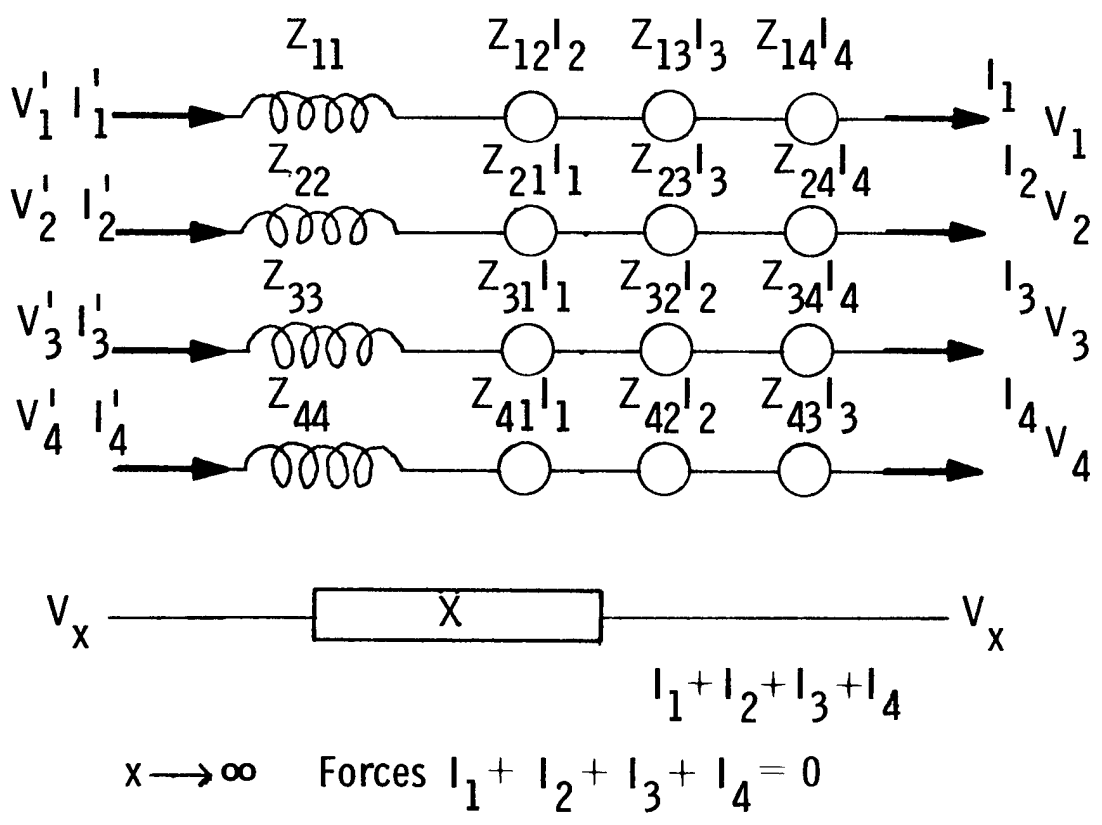


Fig. 46.  
Model for the RFQ's infinitesimal series-impedance element.

where S and T are given by

$$S = \begin{pmatrix} 1/4 & -1/4 & 1/4 & -1/4 \\ 1/2 & 0 & -1/2 & 0 \\ 0 & 1/2 & 0 & -1/2 \\ 1/4 & 1/4 & 1/4 & 1/4 \end{pmatrix}, \quad T = \begin{pmatrix} 1 & -1 & 1 & -1 \\ 1 & 0 & -1 & 0 \\ 0 & 1 & 0 & -1 \\ 1 & 1 & 1 & 1 \end{pmatrix},$$

and the inverses are  $S^{-1} = T^T$ , and  $T^{-1} = S^T$ . The transformed matrix equation is

$$\begin{pmatrix} v' \\ i' \end{pmatrix} = m \begin{pmatrix} v \\ i \end{pmatrix},$$

where the transformed matrix m is

$$m = \begin{pmatrix} 1 & SZT^{-1}\delta x \\ TYS^{-1}\delta x & 1 \end{pmatrix}.$$

The corresponding transmission-line equations are

$$\frac{dv}{dx} = zi,$$

and

$$\frac{di}{dx} = yv,$$

where  $z = SZT^{-1}$ ,  $y = TYS^{-1}$ , and the corresponding wave equation is

$$\frac{d^2v}{dx^2} = zyv.$$

If the matrix for an infinitesimal element is obtained using the parameters from Figs. 45 and 46, transforming to the mode basis will yield explicitly the coupling factors postulated earlier. A useful simplification of the model is obtained if the fact that, effectively, there is no coupling to the zero mode is made explicit in the transformed shunt-admittance and series-impedance matrices.

## VI. ATS RFQ DATA

Table II lists the fits to a Fourier series of perturbation data for the ATS RFQ. The data set was obtained after adjusting the end terminations to minimize the ratio of the maximum field to the minimum field before installation in the manifold. Improvement in the distribution of the quadrupole component was made at the expense of introducing a large mixture of dipole components.

Figures 47, 48, and 49 are computer plots of the magnetic field data for the ATS RFQ with open-circuit boundaries. The data shown in Fig. 50 are the direct perturbation data representing the square of the magnetic field at selected points along the structure. A computer plot of the same data appears in Fig. 51. This is the final field-distribution measurement made before the

TABLE II

### BEST ADJUSTMENT OF END TUNERS

Quadrupole	$1.0 - 0.24 \cos v + 0.044 \sin v + 0.31 \cos 2v - 0.021 \sin 2v$ $- 0.09 \cos 3v + 0.017 \sin 3v$
Dipole 1	$-0.46 - 0.76 \cos v + 0.07 \sin v + 0.46 \cos 2v - 0.02 \sin 2v$ $- 0.13 \cos 3v - 0.063 \sin 3v$
Dipole 2	$-0.77 + 0.10 \cos v + 0.15 \sin v - 0.10 \cos 2v - 0.10 \sin 2v$ $- 0.004 \cos 3v + 0.43 \sin 3v$

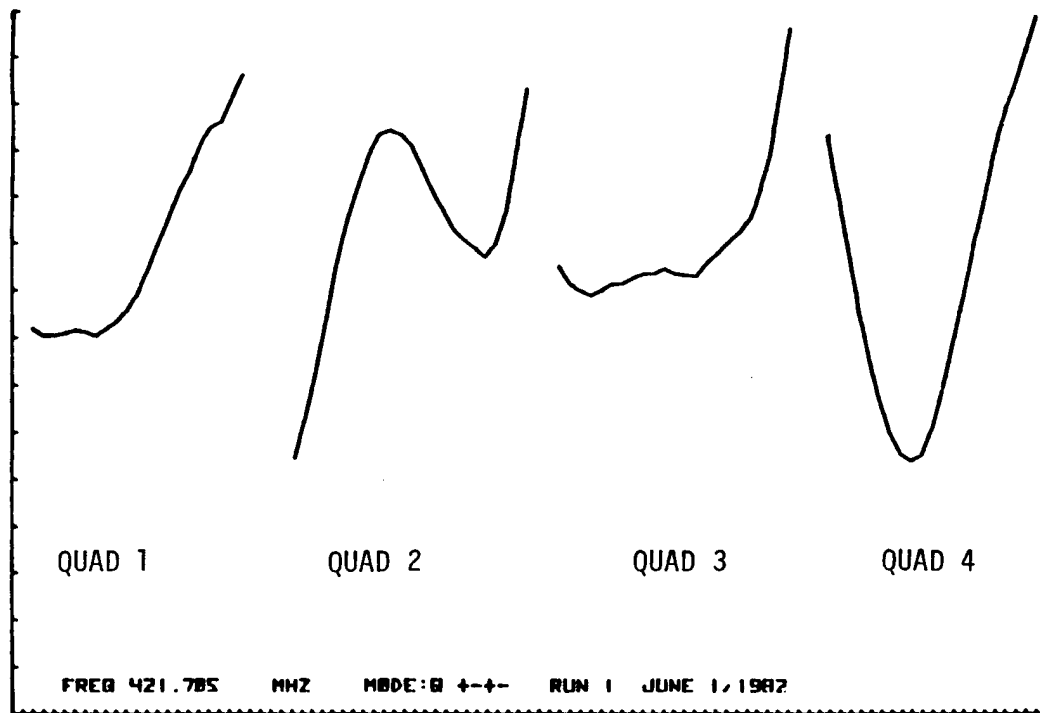


Fig. 47.  
 Quadrupole mode magnetic-field data for open-circuit termination.

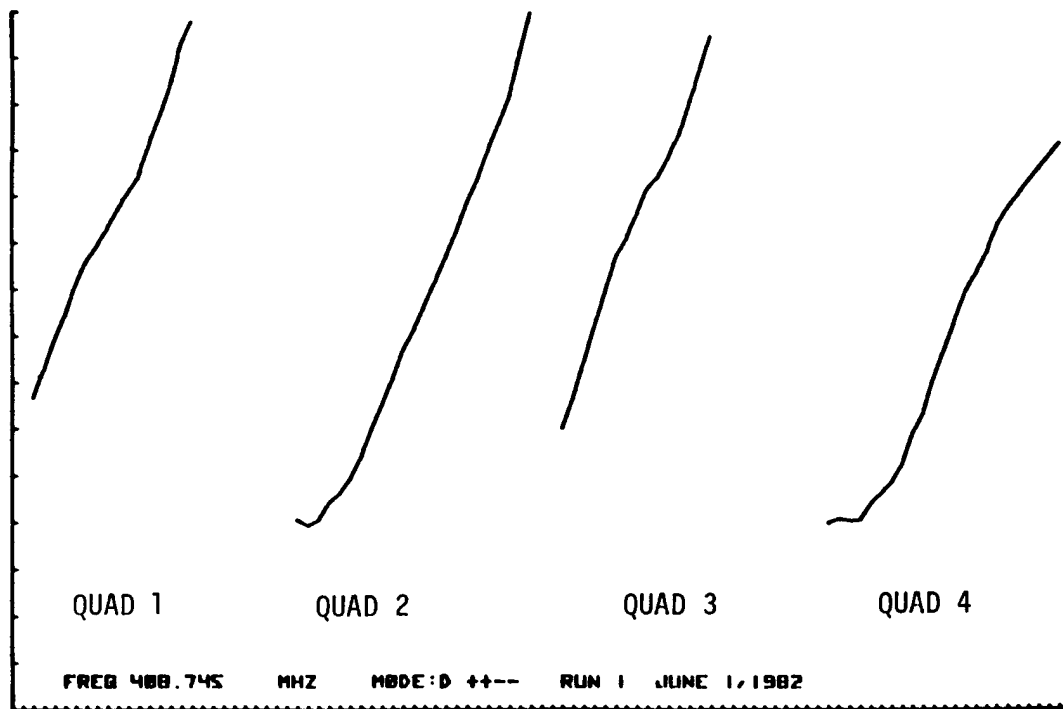


Fig. 48.  
 Dipole Mode 1 magnetic-field data for open-circuit termination.

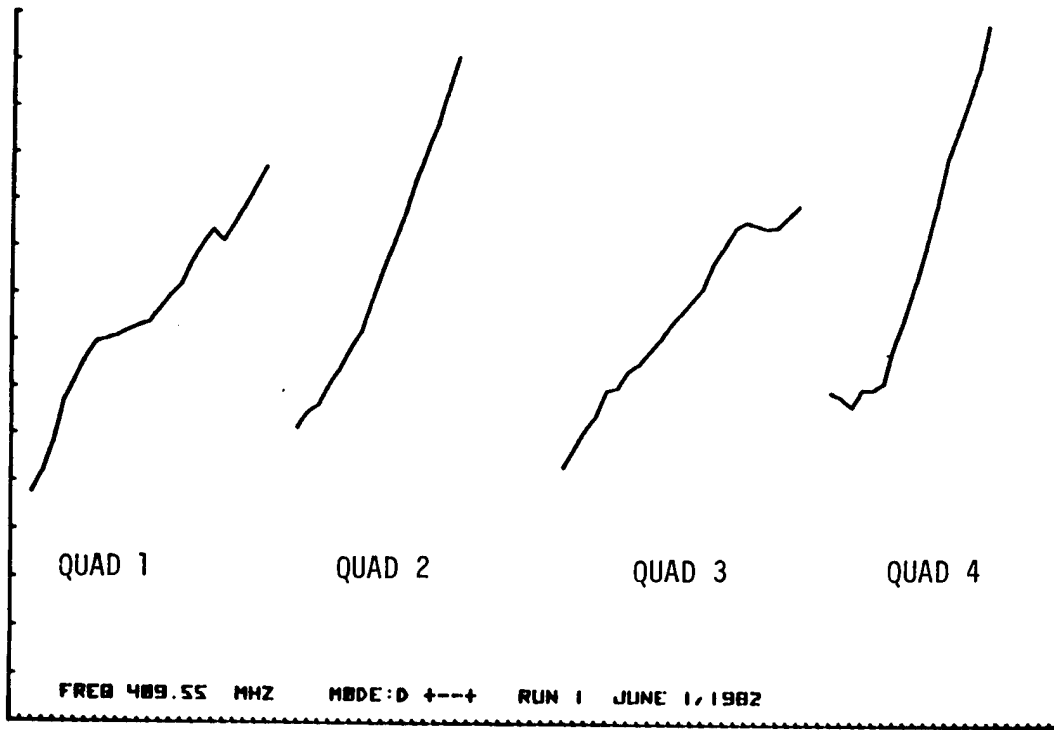


Fig. 49.  
Dipole Mode 2 magnetic-field data for open-circuit termination.

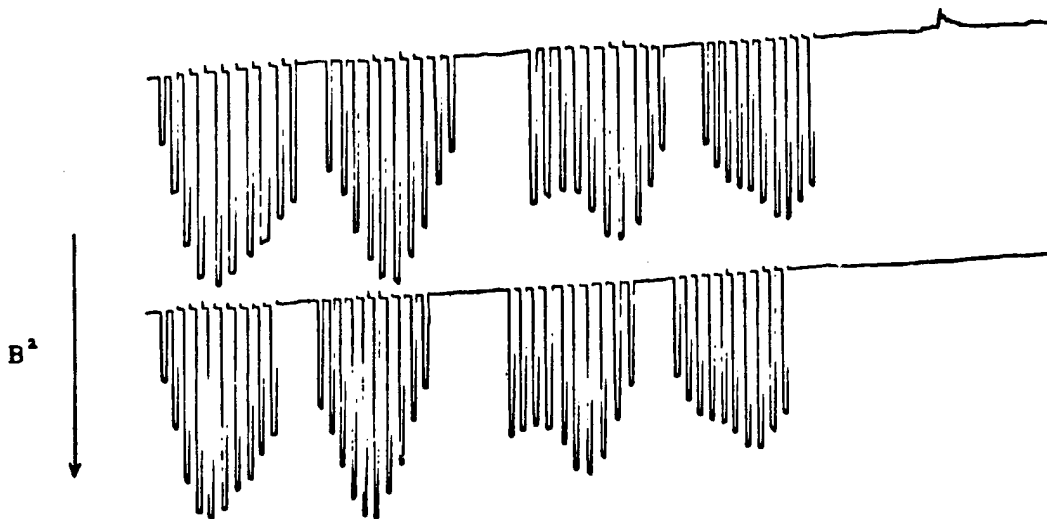


Fig. 50.  
Raw magnetic-field data from final RFQ measurement before installation in the manifold.

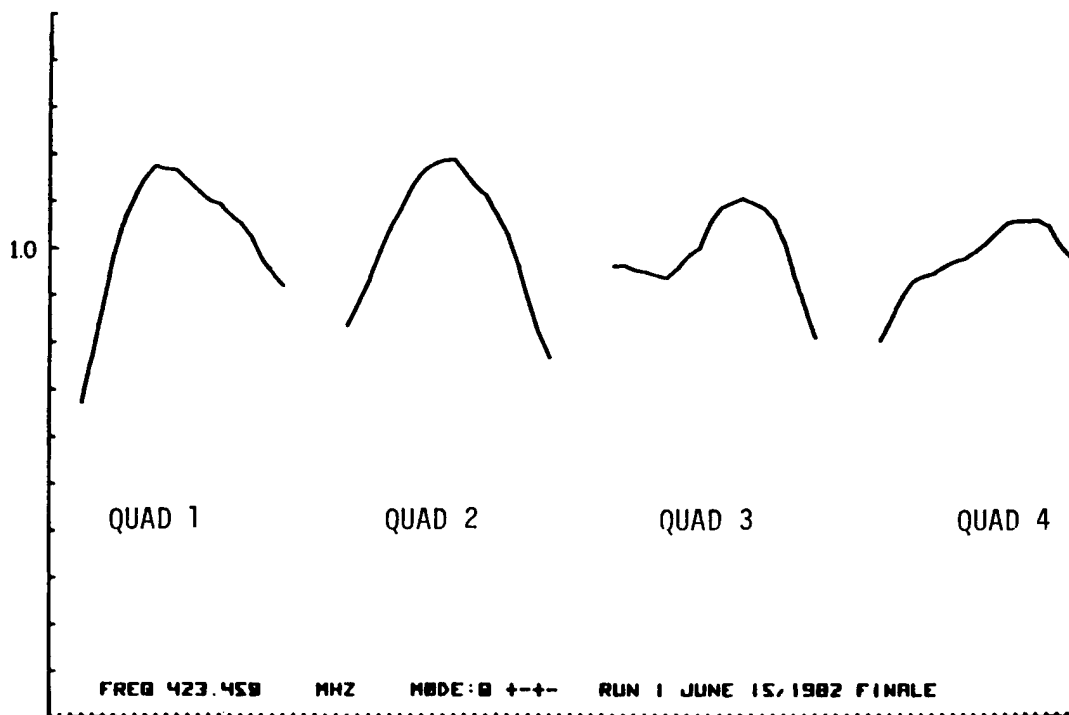


Fig. 51.  
Computer plot of raw magnetic-field data.

RFQ was installed in its rf manifold. An initial determination after installation of the RFQ in the manifold indicates that the fields have changed less than 5%.

## VII. TECHNIQUES FOR IMPROVING LONG RFQ STRUCTURES

Basically there are two principles that can be applied to improve the performance of long RFQ structures. The first is to reduce the problem to a previously solved case by somehow breaking the structure into several short structures. An alternative approach is to develop a structure that forces the fields to have less dependence on the uniformity of the structure.

### A. Shorter Structures

If it were possible to obtain the same performance with respect to emittance growth in a shorter structure, a longer structure still would be desirable in order to have even better performance. Breaking the structure

into several shorter sections seems, at first glance, to be a simple solution. However, this technique raises several new questions that have not yet been completely answered. One needs to know the effect a longitudinal gap in the vanes would have on beam properties. In addition, the problems of keeping the field distribution continuous across the gap and keeping the axes of the sections aligned must be carefully considered. The problem of keeping the vane-tip potentials continuous across a break in the structure can be solved by periodically breaking the magnetic flux path in the structure while leaving the vane tips continuous. It is not yet clear if this approach would be effective because longitudinal currents flowing in the vane tips would couple the sections.

### B. Modified Structures

A related solution, based on an idea developed at Chalk River in Canada, would involve making only one pair of opposing vanes continuous. The other pair would be interrupted by being grounded. Each section would have one pair of vanes grounded on one end and the other pair of vanes grounded on the other end. Such a structure raises new beam-dynamics questions. However, because it is not operated at the cutoff mode but in a mode with finite group velocity and should therefore be somewhat less susceptible to longitudinal tuning errors, it is worth further consideration.

The Chalk River idea also somewhat reduces problems with coupling to dipole modes. Work on another interesting concept that addresses the dipole-mode problem is being done at Lawrence Berkeley Laboratory. Periodically placed shorting rings, connecting opposite vanes, have been shown to disturb the dipole modes while having little effect on the quadrupole-mode field distribution. Figure 52 shows the theoretical passband for a dipole mode in a structure similar to the ATS RFQ. The bottom curve is the passband for no inductive loading. (The vane-to-vane shorts are considered to be inductors.) Adding four sets of 50-nH inductors, spaced one-fourth of the structure's length apart, raises the bottom end of the dipole passband as shown by the second curve. The mode at 462 MHz is unaffected by the shorting rings because its guide wavelength is exactly twice the spacing between the shorts. As seen in the figure, the loading is not enough to move the passband far enough from the operating mode to reduce problems with dipole modes. Reducing the ring inductance or adding more rings would improve the situation, but the effective

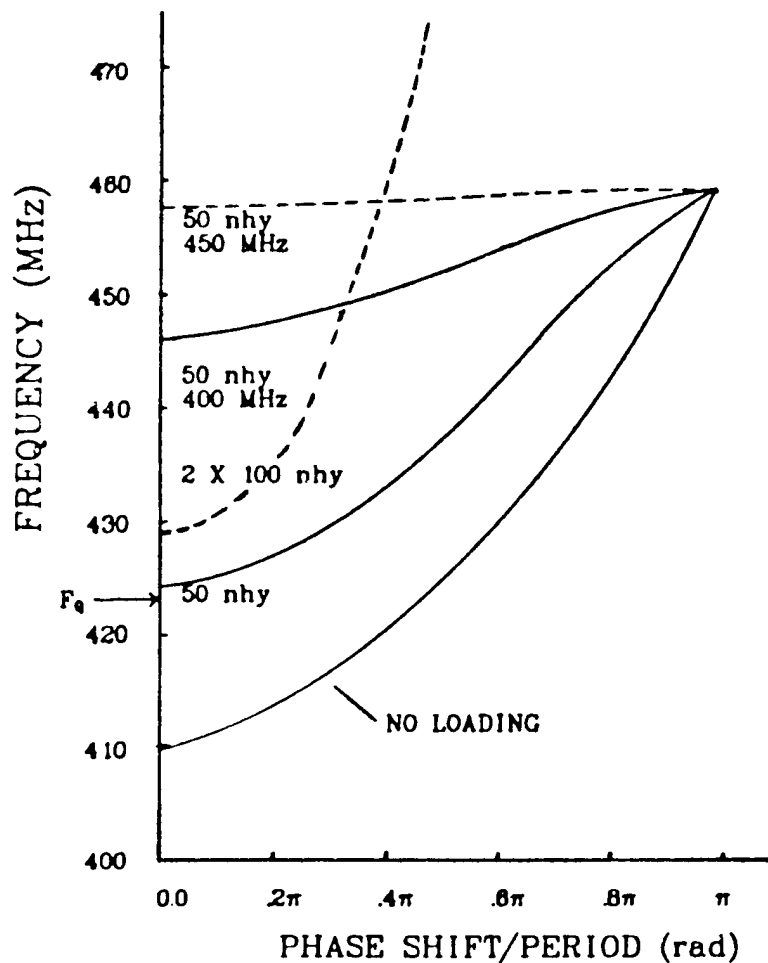


Fig. 52.  
Dispersion curves for RFQ  
with ring-loaded vanes.

inductance can be reduced also by adding a series capacitance to resonate the inductance at or near the operating frequency. The top two curves in Fig. 52 show the effect of tuning four vane-to-vane shorting rings to 400 and 450 MHz. This is clearly much more effective than adding a large number of shorting rings with the same inductance, and the tuning accuracy required is not critical. Figure 53 illustrates how either resonant or nonresonant shorting rings could be installed in an RFQ.

Shorting rings, especially resonant shorting rings, seem to be an effective way to improve the symmetry of the RFQ structure. The problem of reducing the sensitivity of a long RFQ to errors in the cross section of the structure does not seem to have such a simple solution. However, the possibility of improving the field distribution by connecting sections of the structure with something that provides a good alternate power-flow path is worth further

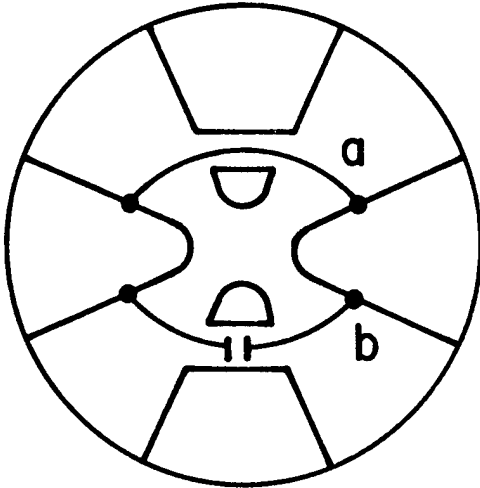


Fig. 53.  
Two possibilities for loading rings:  
a. inductive, b. resonant.

onating capacitor, the currents in the two oscillators are equal only if the two frequencies are equal. When we add the capacitor and tune the slot to resonate at the operating frequency, the mutual impedance is raised and the currents are forced to be nearly equal, even if the two oscillator frequencies differ significantly. The sketch in Fig. 54b illustrates one way to implement

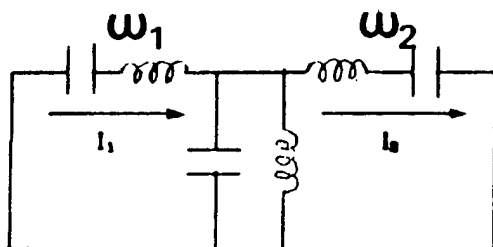


Fig. 54a.  
Schematic illustration of possible  
slot-tuning capacitor.

investigation. One way to implement such a scheme would be by resonating the slots that couple the RFQ to its manifold. The manifold has good power-flow characteristics, at least in the longitudinal direction. Resonating the slots would force the currents intercepted by each side of each slot to be equal. Because the manifold mode has good power-flow characteristics and the RFQ has poor power flow, the RFQ fields would tend to lock to the manifold fields.

Figure 54a is a simplistic representation of an RFQ coupled to a manifold. In the absence of the res-

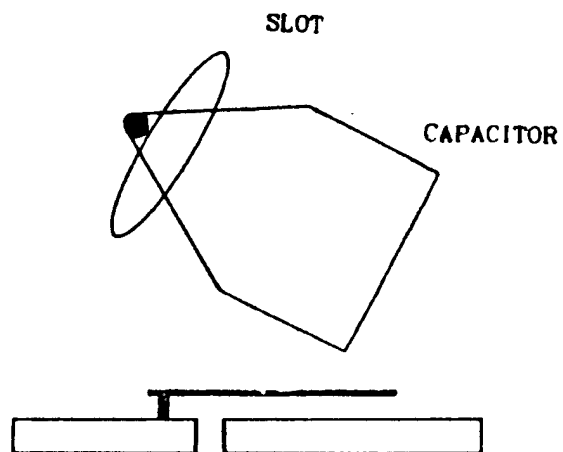


Fig. 54b.  
Possible mechanical configuration of  
slot-tuning capacitor.

the resonating capacitor. We have demonstrated experimentally the feasibility of resonating a slot in this way. What remains is to sufficiently understand the properties of multiple resonant slots to permit tuning them correctly.

#### VIII. THE BOTTOM LINE

It appears that the best hope for success in building long RFQ structures that are insensitive to fabrication errors is to build them with resonant shorting rings and to couple them to an external manifold with resonant slots. If this is feasible, then tractable RFQ structures of arbitrary length can be built.

## RFQ BEAM DYNAMICS

### I. INTRODUCTION

Four years ago the Los Alamos Accelerator Technology (AT) Division initiated a program to investigate the properties of the RFQ accelerating structure. The RFQ is a new concept originally proposed by Kapchinskii and Teplyakov.<sup>1</sup> Our development of this structure, the first outside of the USSR, has culminated in a successful experimental test of the RFQ principle.<sup>2</sup> We conclude that the RFQ offers an attractive solution to the low-velocity problems that are an intrinsic part of many accelerator systems.<sup>3</sup> In this report we emphasize the RFQ's functional properties and briefly discuss our methods for designing RFQ systems. Also, we describe the RFQ's application for the ATS.

The RFQ uses rf transverse electric fields to focus ions traveling along its axial region. Figure 55 is a schematic section of the RFQ resonator. It operates in a modified  $TE_{210}$  mode in which the currents flow transversely to the z-axis. The current flow results in +-+ polarities on the pole tips at a certain time, thus producing a quadrupole focusing, or defocusing, force in a given transverse plane. One-half cycle later these forces reverse sign to produce an overall strong focusing effect. The focusing force at a given time is spatially continuous along the z-axis. If the pole tips have a constant radius, only a radial focusing force is present. In Fig. 55 the pole tips have

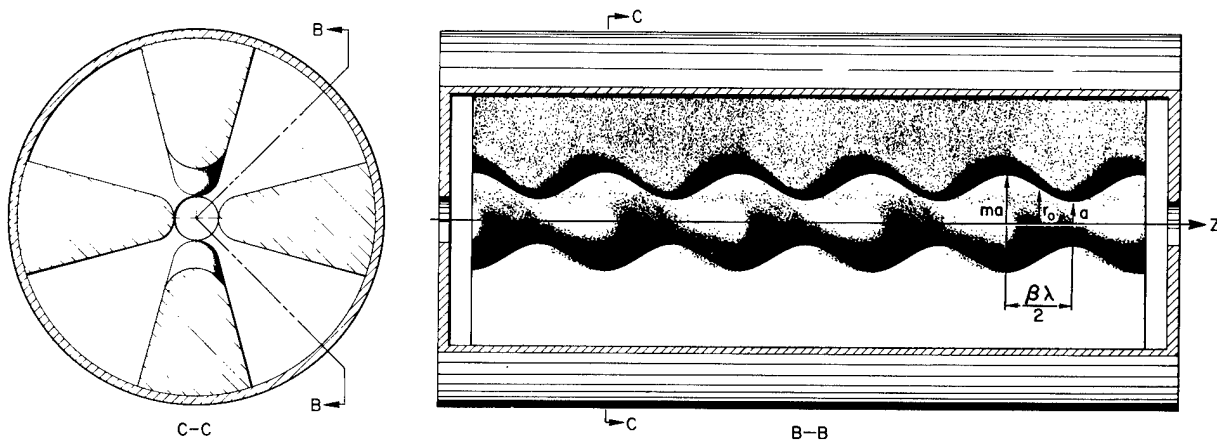


Fig. 55.  
Schematic drawing of an RFQ resonator.

a sinusoidal-like variation in radius. Between the x- and y-plane pole tips, this variation in radius is shifted by  $\beta\lambda/2$ . This pole-tip modulation produces longitudinal accelerating fields in addition to the transverse focusing field.

The operation of an RFQ system in the USSR has been described previously.<sup>4</sup> Early in 1980 a highly successful experimental test at Los Alamos confirmed predicted behavior and general capabilities of an RFQ system.

## II. GENERAL PROPERTIES OF THE RFQ

An RFQ system can be designed to accept an intense low-velocity unbunched ion beam from a low-voltage dc injector; then it will provide radial focusing, bunching, and acceleration to a velocity where a conventional linac operates efficiently. Because the electric force is independent of velocity, the RFQ is especially effective in the radial focusing of low-velocity ions. In typical systems that we have designed, the dc injector can have a voltage of 50 kV for protons or 250 kV for  $\text{Xe}^{+1}$  ions. Once the radial focusing of the beam has been obtained, the RFQ can provide useful longitudinal functions. For example, it can bunch the beam slowly enough to capture a very high percentage of the injected beam. This adiabatic bunching can be accomplished in a reasonable distance because of the low velocity of the ions. The bunching cycle also can be designed to increase the current capacity of the system. While the beam is being bunched, it is also being accelerated so that by the time the final synchronous phase is reached, the beam energy has been increased by about a factor of 10. This allows acceptance of high-current beams at the input and acceleration with only minimal emittance growth. In applying the RFQ in a specific case, it is possible to optimize its characteristics in a flexible way to obtain the desired compromise between transmission efficiency, emittance growth, beam current capacity, overall length, and power dissipation.

## III. BEAM-DYNAMICS ANALYSIS AND POLE-TIP DESIGN

As a basis for beam-dynamics simulation calculations and for construction of RFQ pole tips, we use the lowest order potential function. Our procedure is summarized in Fig. 56. Electric fields obtained from the potential function

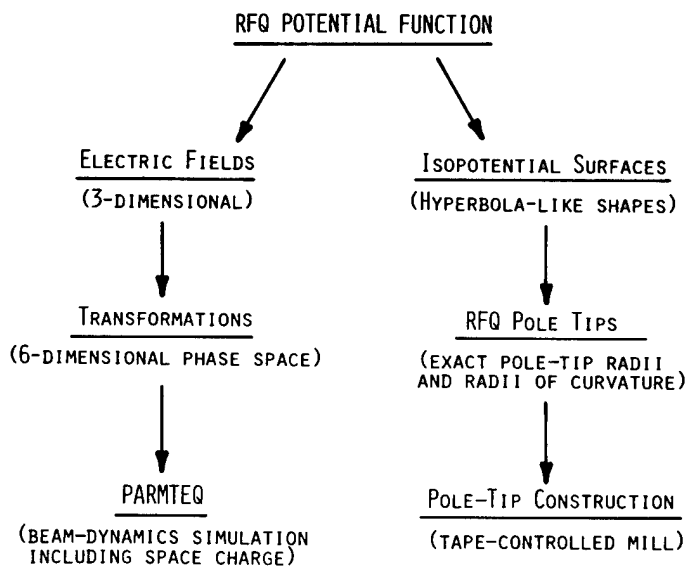


Fig. 56.  
Beam-dynamics simulation and pole-tip geometry.

were used to construct transformations for the beam-dynamics simulation program PARMTEQ.<sup>5,6</sup> This program, which includes space-charge effects, analyzes specific RFQ designs to obtain transmission efficiency, radial emittance growth, and radial and longitudinal characteristics of the output beam. From an appropriate isopotential surface, we obtain the radial variation of the pole tips and the variation of their radius of curvature in the transverse plane, both as a function of  $z$ . Figure 55 shows the unit cell of length  $\beta\lambda/2$ , through which the radius varies from  $ma$  to  $a$ . In the center of the unit cell, the pole tips have quadrupolar symmetry and the radius  $r_0$ . The pole tips are constructed by generating a data file on magnetic tape that is used as input to a numerically controlled milling machine.

#### IV. BEAM-DYNAMICS DESIGN PROCEDURES FOR RFQ SYSTEMS

The methods used to synthesize RFQ systems to meet specific objectives have been previously described.<sup>6</sup> Figure 57 shows how the design procedures can be divided into four separate sections. The unbunched beam from the dc injector first goes into the radial matching section, where the radial focusing strength is increased from a low initial value to a higher final value in  $\sim 5\beta\lambda$ . This allows the beam to adapt itself adiabatically to the time-varying focusing forces. The next section is the shaper where we start to ramp both  $\phi_s$  and

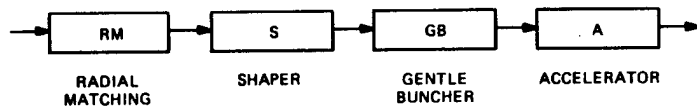


Fig. 57.  
RFQ functional block diagram.

$E_0$ , the average longitudinal field. The phase angle  $\phi_s$  starts at  $-90^\circ$  and increases linearly with  $z$ ;  $E_0$  starts at zero and is slowly turned on by increasing the amplitude of the pole-tip modulation. If the parameters are chosen correctly, we can "shape" the particle distribution at the output of the shaper to occupy the desired level in the phase stable region of the bucket. Next is the gentle buncher where two conditions are imposed, as suggested by Kapchinskii.<sup>1</sup> The average  $z$ -length of the bunch is held constant, and the small-amplitude longitudinal frequency is held at a fixed value. This allows the final value of  $\phi_s$  to be attained at the end of the gentle buncher and preserves the particle distribution throughout. In the accelerator section, the ions are accelerated to their final energy at a constant value of  $\phi_s$ .

The design methods described previously are constrained to make the average radius of the pole tips  $r_0$  constant, except in the radial matching section.<sup>6</sup> This keeps the distributed capacitance nearly constant for easier resonator tuning and is consistent with a constant value of the focusing strength  $B$ . Also, the voltage is assumed to be constant along the vanes.

The strong quadrupole focusing in the RFQ must compensate for the defocusing effects that are due to both the rf-defocus term and the space charge. The ideal RFQ electric fields in the region of the beam are given in Eq. (1) in cylindrical coordinates,  $r, \psi, z$ .

$$E_r = \frac{\chi V r}{a^2} \cos 2\psi - \frac{kAV}{2} I_1(kr) \cos kz \quad ,$$

$$E_\psi = \frac{\chi V r}{a^2} \sin 2\psi \quad ,$$

and

$$E_z = \frac{kAV}{2} I_0(kr) \sin kz \quad . \tag{1}$$

Each term should be multiplied by  $\sin(\omega t + \phi)$  to include the time dependence  $k = 2\pi/\beta\lambda$ ;  $V$  equals the voltage between adjacent vanes. The quadrupole terms in  $E_r$  and  $E_y$  are proportional to the focusing efficiency  $\chi$ . The accelerating field  $E_z$  depends on the acceleration efficiency  $A$ . The second term of  $E_r$  is the rf defocus term, which depends on the acceleration efficiency  $A$  and on  $z$ . When the  $\sin(\omega t + \phi)$  is included and when the term is averaged over a cell, it is defocusing for synchronous phases that correspond to longitudinal phase focusing, a result that also occurs for conventional linacs. Because of the strong dependence of rf defocusing on particle velocity, this term becomes more important for low-velocity structures, and furthermore it is inherently a nonlinear defocusing force, which is stronger at larger radii.

To include the space-charge defocusing in our design procedures, we make use of a simple model that assumes a uniform three-dimensional ellipsoid for the average charge distribution in the bunch and assumes the smooth approximation to include both the quadrupole-focusing and the rf-defocusing terms.<sup>7</sup>

We are able to calculate limiting currents from this model for both longitudinal and transverse degrees of freedom. Figure 58 shows the calculated current limits versus the dimensionless focusing strength  $B$  for a family of Fusion Materials Irradiation Test (FMIT) RFQ designs that has a fixed peak-surface electric field. Each value of  $B$  represents a different RFQ. The two curves give the calculated transverse- and longitudinal-current limits from the model. The design, where the two curves intersect and the current limits are equal, has the maximum beam-current capacity. The dots are corresponding computer simulations from the program PARMTEQ. The excellent agreement shows that the model is a useful guide for high-current RFQ design.

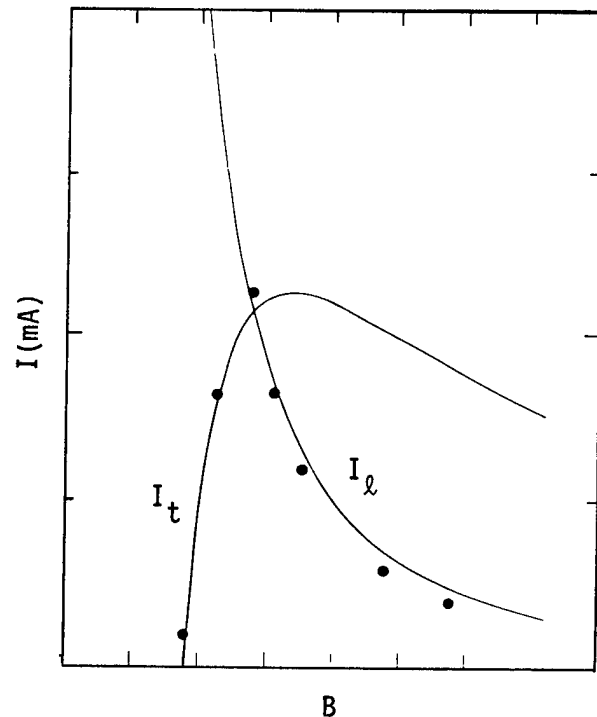


Fig. 58. Typical current limits versus normalized quadrupole-gradient  $B$  for RFQ designs.

## V. RFQ EXPERIMENTAL TEST

Early in 1980, we conducted a full-scale experimental test of the RFQ principle. The test linac was designed to accept a beam of protons from a 100-kV dc injector and to focus, bunch, and accelerate the beam to a final 640-keV energy. The RFQ test resonator had 1.1-m-long vanes and a 0.15-m o.d. The rf power was furnished by a 425-MHz klystron that was coupled to the resonator through a coaxial manifold and coupling slots. The beam-dynamics design for this test and the calculated performance have been described previously.<sup>6</sup>

The momentum spectrum of the accelerated beam was measured with a 45° magnetic analyzing system.<sup>2</sup> This system confirmed an expected 640-keV energy for the accelerated particles, and we observed no low-energy components. Adjusting the RFQ vane voltage made it possible to rotate the final longitudinal phase space to yield a 3% FWHM minimum energy spread.

The transmission efficiency was measured with biased Faraday cups immediately before and after the linac. With a 30-mA injected beam, the output beam current was 26 mA, corresponding to the predicted 87% transmission efficiency.

The input beam emittance was measured ahead of the lens that matches the beam from the dc injector into the RFQ, and the output emittance was measured immediately following the RFQ tank. Typical measurements for a 25-mA output beam indicate a normalized rms emittance-growth factor of  $\sim 1.5$ . We believe this to be an upper limit because the injected beam's emittance is somewhat increased in the matching lens.

The test linac's reliability and simplicity of operation were outstanding. After an initial conditioning period, the RFQ operated continuously, accelerating a 20-mA beam current for more than a month at a 0.1% duty factor. Also, the test has shown that the RFQ is tolerant of both constructional errors and errors in the rf resonator tuning.

## VI. RFQ DESIGN FOR THE ATS

Table III summarizes the properties of a high-current H<sup>-</sup> design for the ATS. This RFQ bunches and accelerates a 100-mA H<sup>-</sup> beam from 0.1 MeV to 2.072 MeV at a 425-MHz frequency. The results of a computer simulation using the program PARMTEQ are shown in Table IV.

TABLE III

## ATS RFQ DESIGN PARAMETERS

Frequency	425 MHz
Ion	H <sup>-</sup>
Number of cells	356
Length	289.23 cm
Vane voltage	111.34 kV
Average radius, $r_0$	0.394 cm
Final radius, $a_f$	0.270 cm
Final modulation, $m_f$	1.830
Initial synchronous phase, $\phi_i$	-90°
Final synchronous phase, $\phi_f$	-30°
Peak surface field	41.4 MV/m (2.06 Kilpatrick)
Nominal current limit	167 mA
Nominal acceptance at 100 mA	$0.232\pi$ cm <sup>2</sup> ·mrad (normalized)

TABLE IV

## RESULTS OF PARMTEQ SIMULATION

	<u>Input Conditions</u>
$W_I$	0.10 MeV
$E_{rms}$	0.0166 $\pi$ cm $\cdot$ mr (normalized)
I	110 mA
	<u>Output Conditions</u>
$W_F$	2.072 MeV
$E_{rms}$	0.0207 $\pi$ cm $\cdot$ mr (normalized)
Transmission	91%
I	100 mA

## REFERENCES

1. I. M. Kapchinskii and V. A. Teplyakov, "Linear Ion Accelerator With Spatially Homogeneous Strong Focusing," Prib. Tekh. Eksp., No. 2, p. 19 (1970).
2. J. E. Stovall, K. R. Crandall, and R. W. Hamm, "Performance Characteristics of a 425-MHz RFQ Linac," Proc. 6th Conf. on Applications of Accelerators in Research and Industry, Denton, Texas, November 3-5, 1980, IEEE Trans. Nucl. Sci. 28, p. 3469 (1981).
3. D. A. Swenson, "Low-Beta Linac Structures," Proc. 10th Linear Accelerator Conf., Montauk, New York, September 10-14, 1979, Brookhaven National Laboratory report BNL-51134, p. 129 (1980).
4. B. M. Gorshkov, S. A. Il'evskii, G. M. Kolomenskii, S. P. Kuznetsov, N. N. Kutorga, A. P. Mal'tsev, K. G. Mirzoev, V. B. Stepanov, V. A. Teplyakov, and I. M. Shalashov, "Startup of the URAL-15 Linear Proton Accelerator With Quadrupole RF Focusing," Sov. Phys. Tech. Phys. 22 (11), p. 1348 (November 1977).

5. R. H. Stokes, K. R. Crandall, J. E. Stovall, and D. A. Swenson, "RF Quadrupole Beam Dynamics," IEEE Trans. Nucl. Sci. 26, p. 3469 (1979).
6. K. R. Crandall, R. H. Stokes, and T. P. Wangler, "RF Quadrupole Beam-Dynamics Design Studies," Proc. 10th Linear Accelerator Conf., Montauk, New York, September 10-14, 1979, Brookhaven National Laboratory report BNL-51134, p. 205 (1980).
7. T. P. Wangler, "Space Charge Limits in Linear Accelerators," Los Alamos Scientific Laboratory document LA-UR-8388 (December 1980).

## DTL BEAM DYNAMICS

### I. INTRODUCTION

Details of the computer design of the 2- to 5-MeV 425-MHz DTL are given in Refs. 1 and 2. We will describe the parametric searches that were made, the final design, the proposed transport section to join the RFQ to the DTL, and the results of beam-dynamics simulations through the entire system.

### II. DESIGN SUMMARY

The object was to design a DTL that would accelerate the RFQ output beam to a 5-MeV energy with minimum emittance growth. The 100-mA beam had a  $0.02\pi$  cm·mrad normalized rms emittance with a 2.07-MeV average energy. Although transverse phase spaces from one structure can be matched into a succeeding one, the longitudinal phase space generally is fixed by the first structure and, except for gradual debunching in the intervening distance, cannot be changed easily. The DTL had to be designed to accommodate this fixed longitudinal size. The parameters of interest, then, are synchronous phase  $\phi_s$  and electric field gradient  $E_0$ .

Accelerators with constant values of  $\phi_s$  from  $-30^\circ$  to  $-70^\circ$  were investigated. Below  $\phi_s$  of  $-40^\circ$ , longitudinal emittance growth and space-charge forces were unacceptably high. The optimum  $\phi_s$  was  $-40^\circ$  with no improvement in any measured quantity at  $\phi_s$  of  $-45^\circ$  or above. Transverse matching became difficult, and longitudinal instabilities worsened at  $\phi_s$  of  $-50^\circ$ .

Constant  $E_0$  of 2 MV/m was chosen because at higher values, 2.5 or 3 MV/m, longitudinal instabilities as defined by space charge  $\mu_L$  caused immediate emittance growth. With current, longitudinal emittance growth causes unacceptable emittance growth in the transverse phase space. The accelerating gradient could be increased linearly with distance, from an initial value of 2 MV/m to as high as 5 MV/m, without serious degradation of beam quality and with significant decrease in length. Such a design may be of interest for a DTL not built primarily for testing purposes.

PM quadrupoles were to be used, and it was hoped they could be identical throughout the linac. This imposed a constraint on both their length, as determined by the geometry of the first few drift tubes, and their strength, which is limited by available materials. Magnets 2.54 cm long having a 0.5-cm radius with 10-kG pole-tip fields have gradients of 20 kG/cm, and these strengths were used when  $\phi_s$  and  $E_0$  were chosen. However, dynamics calculations with off-axis beams or with random quadrupole misalignments showed that the bore radius should be increased to prevent particle loss. When we increased the magnet radius to 0.6 cm and assumed pole-tip fields of 11 kG, the quadrupole gradients were changed to 18.33 kG/cm, which we selected for the final design.

Table V lists the parameters of the accepted DTL. After SUPERFISH calculations by A. Harvey,<sup>3</sup> a corrected data file for PARMILA was used to create drift-tube tables and to make the final dynamics simulations.

TABLE V

THE 5-MeV DRIFT-TUBE LINAC

Injection energy	2.07 MeV
Final energy	5.03 MeV
Frequency	425 MHz
Length	2.39 m
Number of cells	40
Synchronous phase	-40°
Electric field gradient	2 MV/m
Quadrupoles	2.54 cm at 18.33 kG/cm

### III. TRANSPORT DESIGN

In selecting a transport section between the RFQ and the DTL, there must be a compromise between number of knobs available for transverse matching and short length to prevent debunching. If one assumes the output beam from the RFQ will be reasonably constant, the knobs can be eliminated if the transport is well designed.

When we used two drift lengths and two quadrupole strengths as matching parameters and selected, as criteria for a well-matched beam, either smooth ellipse  $\beta$ 's or smooth rms beam sizes in the first 30 cells of the DTL, several good matches were obtained. Some were rejected because drifts were too small or gradients were too high. Because it is necessary to match selected gradients very close to the 18.33 kG/cm used in the linac, we substituted this value and found the match to remain completely satisfactory. The simple transport is shown in Fig. 59. The second quadrupole begins the periodic structure of the DTL and is positioned as though there were a drift tube at the linac entrance. Because the "matching" quadrupoles are identical to those in the DTL, procurement is simplified. The total transport region is short enough to prevent debunching of the beam.

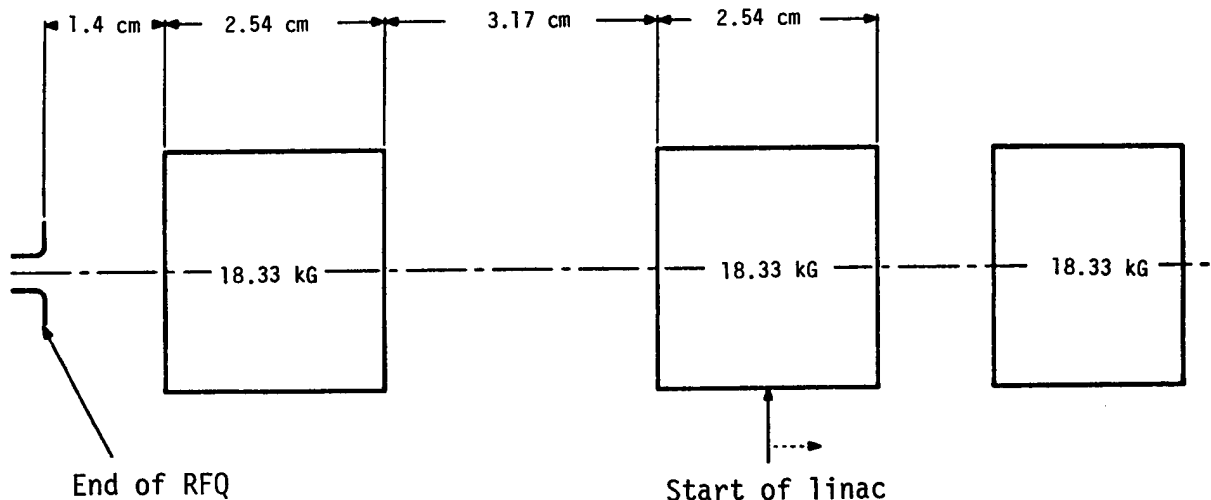


Fig. 59.  
Transport from RFQ to DTL.

#### IV. DYNAMICS SIMULATIONS

Output coordinates of the RFQ were used as input for the final dynamics calculations. Because the RFQ has a synchronous phase of  $-30^\circ$ , the phase of each particle is shifted by  $-10^\circ$  to adjust the bunch to the correct phase for the DTL. (Such a phase shift is possible in a laboratory situation.)

The rms emittances of x-x' and y-y' planes of the design beam are shown in Figs. 60 and 61. Figure 62 shows projections of x and y. Table VI gives values of normalized emittances at entrance and exit of the DTL.

Simulations through the RFQ and DTL of beams with higher and lower brightness have been made. Because of the initial effect of the RFQ, not much was learned about the limits of the DTL. Larger beams have reduced transmission through the RFQ but are accelerated by the DTL with no emittance growth.

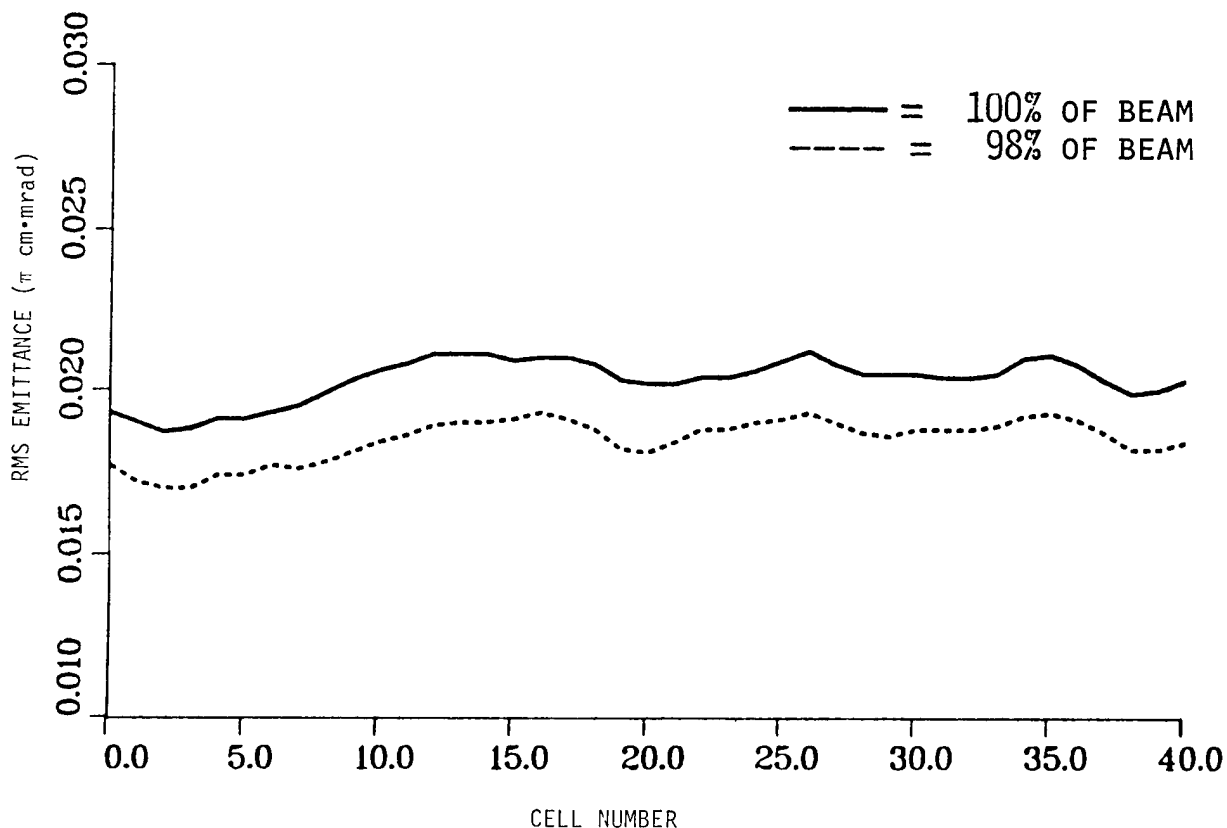


Fig. 60.  
The rms emittance of x-x' plane through the 2- to 5-MeV DTL.

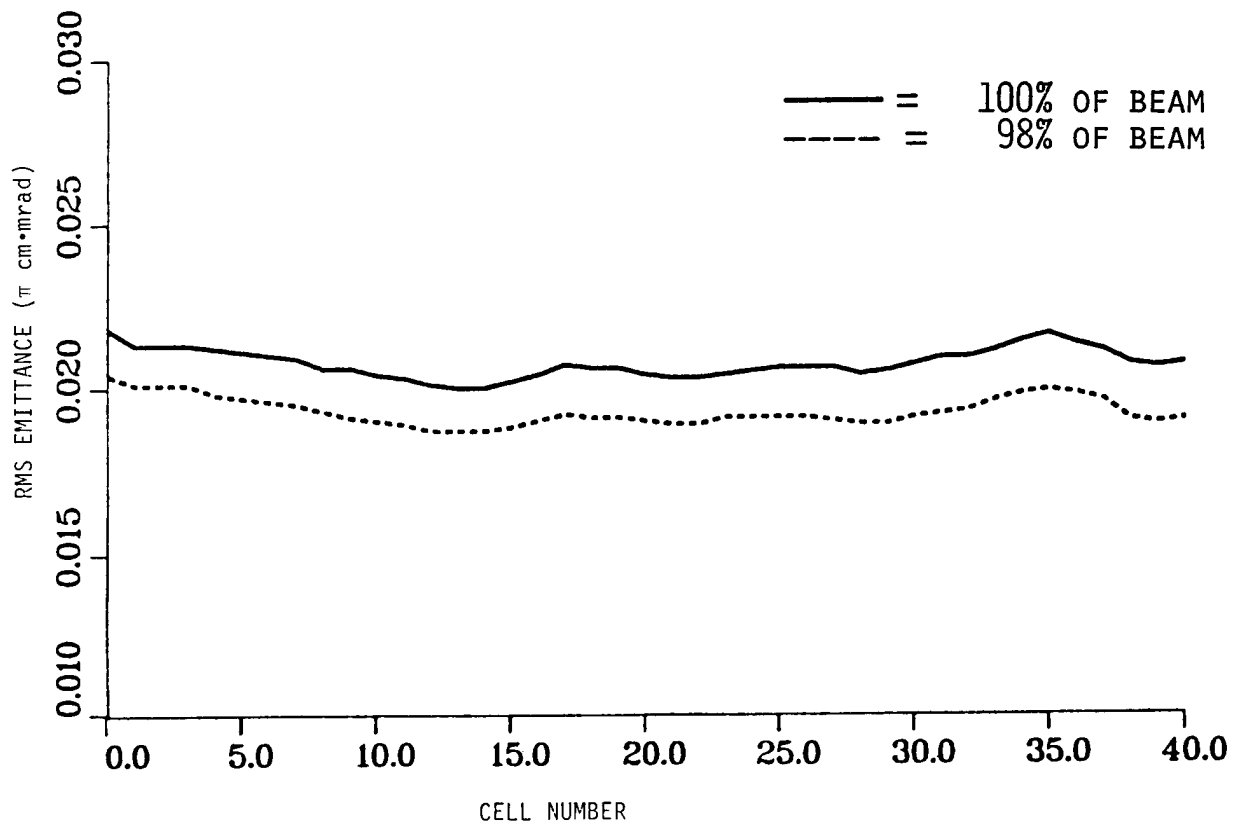


Fig. 61.  
The rms emittance of  $y$ - $y'$  plane through the 2- to 5-MeV DTL.

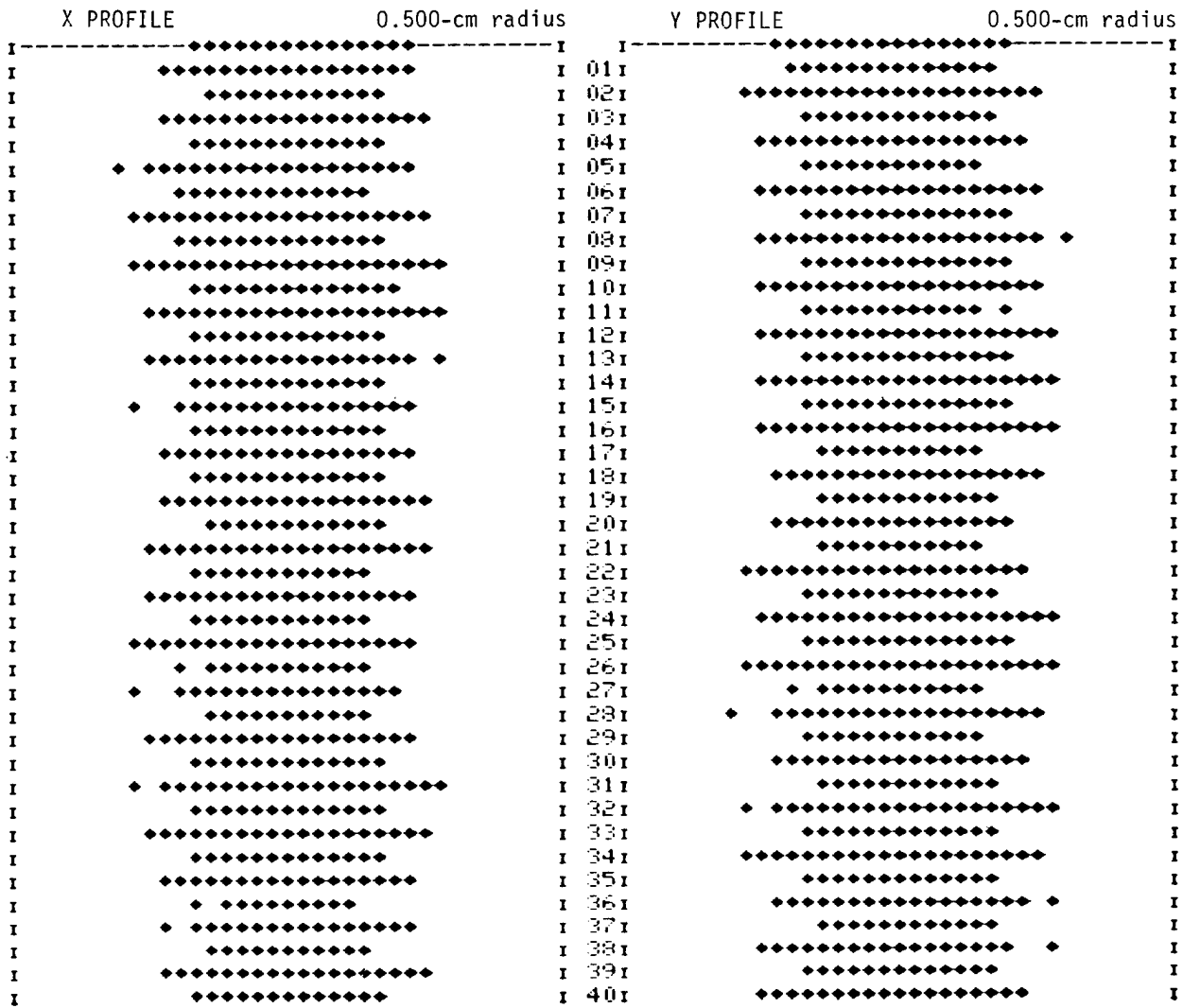


Fig. 62.  
Projections of x and y through the DTL.

Smaller beams into the RFQ have increased emittance growth so that the final beam size is almost the same as the design beam, and the DTL accelerates the beam with no average rms emittance growth.

Simulations made only through the DTL show that a matched beam of 140-mA current within the design emittance specification could be accelerated with no emittance growth.

TABLE VI

EMITTANCE VALUES AT ENTRANCE AND EXIT OF DTL  
( $\pi$  cm $\cdot$ mrad)

	<u>rms, n</u>	<u>E<sub>n</sub> 90%</u>
Input, x-x'	0.019	0.082
Output, x-x'	0.020	0.084
Input, y-y'	0.021	0.096
Output, y-y'	0.022	0.097

## REFERENCES

1. R. Mills and C. Williams, "Computer Design and Sensitivity Studies for a 2- to 5-MeV 425-MHz Drift-Tube Linac," Los Alamos National Laboratory, Accelerator Technology Division, Group AT-1 memorandum No. AT-1:82-92 (April 23, 1982).
2. R. Mills, "AT-2 Drift-Tube Linac and Low-Energy Transport Line," Los Alamos National Laboratory, Accelerator Technology Division, Group AT-1 memorandum No. AT-1:81-355 (Nov. 4, 1981).
3. Alex Harvey, "AT-2 DTL SUPERFISH Runs," Los Alamos National Laboratory, Accelerator Technology Division, Group AT-5 memorandum No. AT-5-81-493 (Sept. 17, 1981).

## ATS DRIFT-TUBE LINAC ENGINEERING DESIGN CONCEPTS

### I. INTRODUCTION

Engineering design of the ATS DTL was initiated in September 1981. A conceptual design, incorporating design parameters developed by the AT-Division Linac Technology Group, AT-1, was produced and has been submitted to peer review by AT-Division personnel. There is no current engineering design activity because of program priority and funding limitation. Some planning activity directed toward a prototype of the first cells of the DTL is being done on a time-available basis.

### II. ENGINEERING DESIGN CRITERIA

Design of the ATS DTL is based on parameters developed by AT-1. The parameters of principal importance to this accelerator are shown in Table VII. Detail design concepts use features of the LAMPF accelerator or that are being tested/evaluated in the FMIT project. Construction/fabrication processes used previously also are incorporated to the maximum degree practical. The conceptual design produced will be modified as necessary to accommodate the as-built characteristics of the ATS RFQ; physical, particle-dynamics, and electrical parameters are of principal importance.

### III. PRINCIPAL MECHANICAL FEATURES

The major mechanical features of this DTL configuration are (1) use of a single mounting beam for all drift-tube assemblies; (2) a mounting beam, used for aligning the drift tubes and for handling drift-tube assemblies for tank installation; (3) a drift-tube beam tank interface, which transfers the stiffness of the tank to the drift-tube mounting beam; (4) alignment of drift tubes on the mounting beam by using precision gauges while the beam is mounted on a precision assembly table-surface plate; (5) alignment accuracy transfer from

TABLE VII

## DTL DESIGN PARAMETERS

Frequency	425 MHz
Input energy	2.07 MeV
Output energy	5.03 MeV
Beam current	100 mA
Peak beam power	300 kW
Cells	40
Drift-tube assemblies	39
First-cell gap	0.996 cm
No. 1 Drift-Tube length	3.346 cm
Last-cell gap	1.991 cm
No. 39 Drift-Tube length	5.228 cm
Drift-tube bore	1.0 cm
Quadrupole magnet length	2.54 cm
Drift-tube-diam to tank-diam ratio (LAMPF 0.177 to 0.191)	0.1795
Quadrupole strength	18.33 kG/m
Accelerating gradient	2 MV/m
Drift-tube azimuthal tolerance	$\pm 0.0127$ cm
Radio-frequency power available	1.25 MW (max)

assembly table to tank, using precision alignment gauges; (6) drift-tube assemblies, using high-strength PM quadrupoles in a separable mount to permit calibration and positioning of the quadrupoles before installation in the drift tubes; (7) a drift-tube stem that provides cooling, rf joint, vacuum seal, and multi-axis drift-tube positioning for alignment; (8) rf, waveguide-window excitation; (9) two remote-control slug tuners; (10) two 10-in. cryopump vacuum-pump ports; (11) combination drift-tube mounting-beam and transport-dolly/lifting-insertion mechanism for installation of the drift-tube mounting-beam assembly into the tank.

#### IV. TANK-DRIFT ASSEMBLY

Figure 63 shows the overall arrangement of the DTL. Shown are the two 10 000- $\ell$ /s vacuum pumps, rf-waveguide transition, slug tuners, post couplers, and drift-tube mounting-beam assembly. The overall tank length shown, 250.8 cm, accommodates the linac drift-tube structure and the interface flanges. Figure 64 (longitudinal section), showing the RFQ DTL matching and Cells 1 through 4, illustrates the severe spacing constraint of the drift-tube-stem mounting in the mounting beam at the upstream end of the DTL. The vertical, inverted mounting of the drift-tube assemblies was chosen to permit the rf-waveguide transition to be at the tank top. Top entrance of rf is highly desirable because the highest radiation levels have been opposite the rf window in similar DTLs. This window allows the maximum radiation flux to be directed toward the floor, thus minimizing possible shielding requirements. The single mounting-beam feature shown previously (Fig. 63) is shown in greater detail in Fig. 65. This configuration was selected to permit all drift-tube assemblies to be mounted and aligned before installation in the tank. Although the mounting beam must provide sufficient stiffness to prevent permanent deflection during handling, the fully assembled tank is the stronger structure. The mounting beam, therefore, provides convenience of access during assembly and alignment, convenience of handling during installation in the tank, precision reference for monitoring of drift-tube position when assembled, and a high-integrity interface for all drift-tube tank penetrations and interfaces. Also shown in this figure is the grouping of drift-tube tank wall penetrations which allow circumferential webs to be left in the tank wall to provide tank resistance

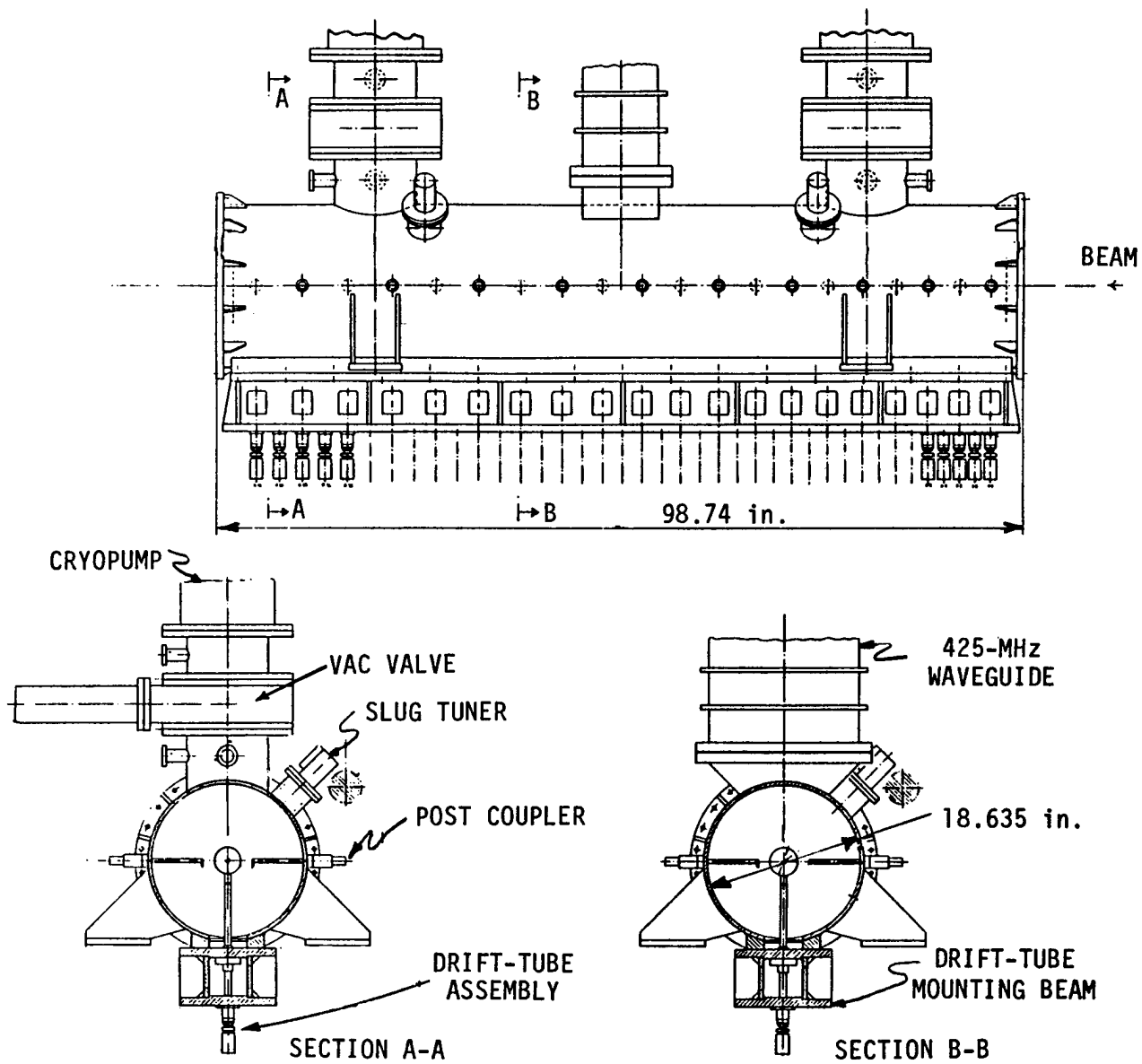


Fig. 63.  
The ATS DTL assembly initial design study.

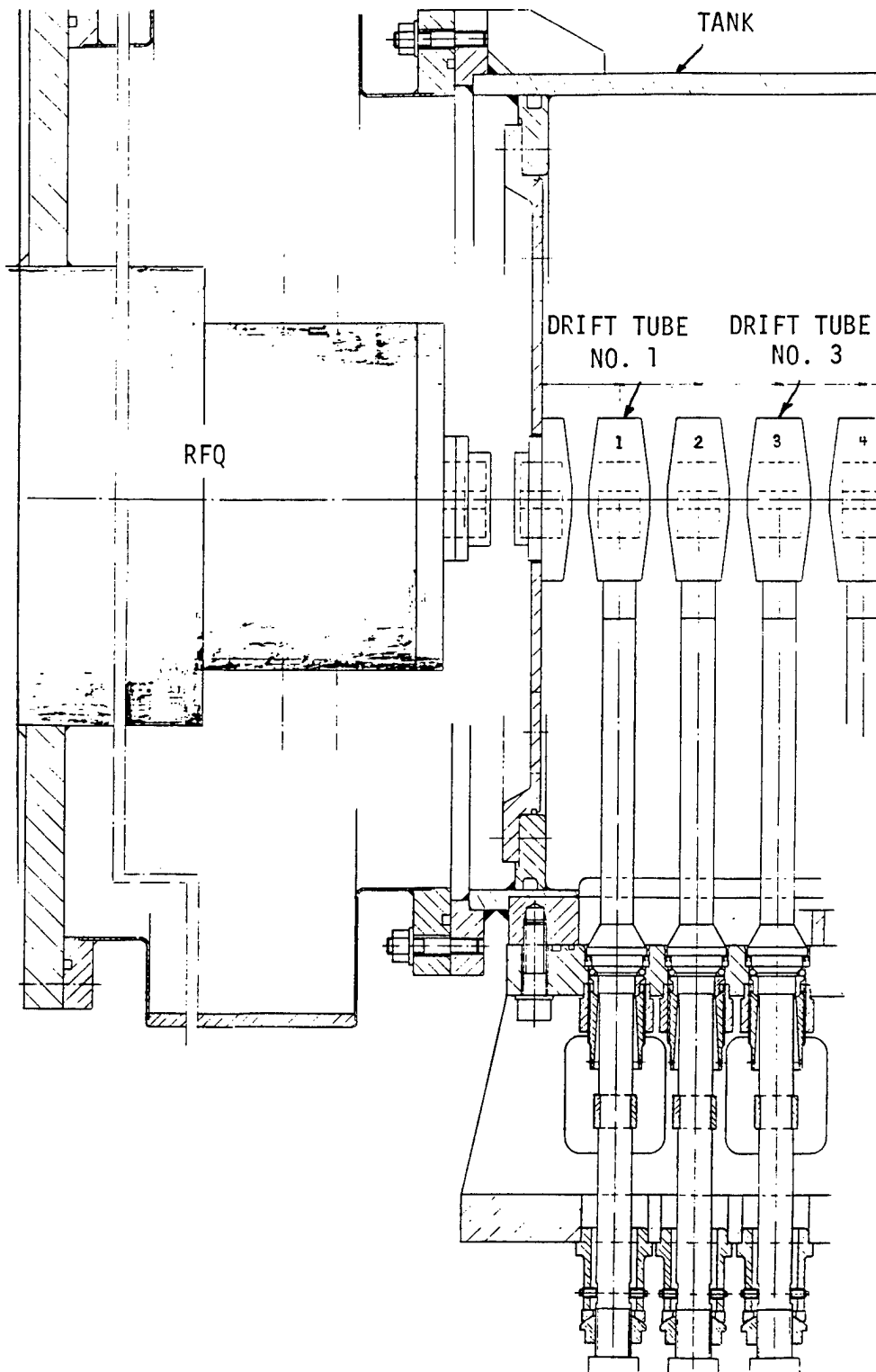


Fig. 64.  
The RFQ DTL initial design study.

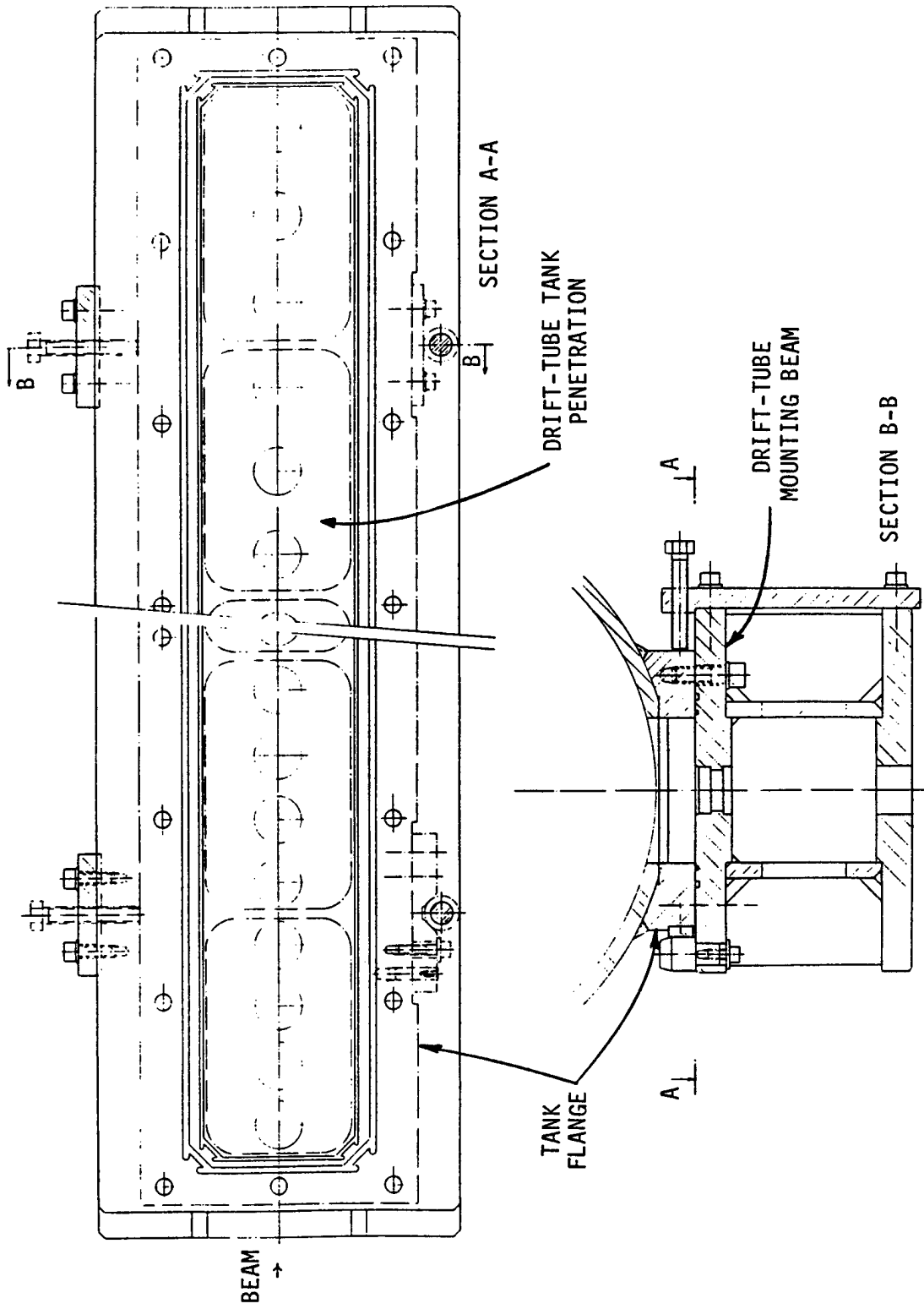


Fig. 65.  
The ATS DTL tank penetration and drift-tube mounting structure initial design study.

to distortion when evacuated. At the upstream end where drift tubes and spacing are small, four drift tubes are mounted per group, whereas at the downstream end, three drift-tube groupings are used.

## V. DRIFT-TUBE ASSEMBLIES

The tank cross section (Fig. 66) further details the features of the drift-tube mounting-beam interface, mounting-beam lifting rods, tank-support bearing blocks, and cooling channels on the tank and in the mounting-beam tank-interface flange. Adjustment of the drift-tube stem is provided by jacking screws and tensioning ball sockets that provide x, y, and z movement of the drift tube. The drift-tube stem, sealed at the tank with rf and vacuum seals, incorporates water-cooling channels for the drift-tube assembly. The stem is provided with rotation tooling (Fig. 67) to permit positioning of the drift-tube bore. Analysis of the inverted pendulum vibrational characteristics of the drift tube has shown that Drift Tube No. 1 has a 66-Hz natural resonance, whereas Drift Tube No. 39 has a 55-Hz natural resonance.

## VI. PERMANENT-MAGNET QUADRUPOLES

The detail design of the PM quadrupole assemblies will require considerable evolutionary development to provide the required magnetic-field accuracy and still maintain desirable fabrication and assembly simplicity. Figures 68 and 69, showing two potential arrangements of the 16 samarium-cobalt magnet segments, also illustrate the extremely confined space available in the upstream drift tubes. The 0.5-cm-radius drift-tube bore, with a 0.6-cm-i.r. magnet segment, permits the use of a bore tube. A bore tube is believed necessary to protect the magnet segments from possible beam impingement and to provide a positive reference for shimming the position of the magnet segments.

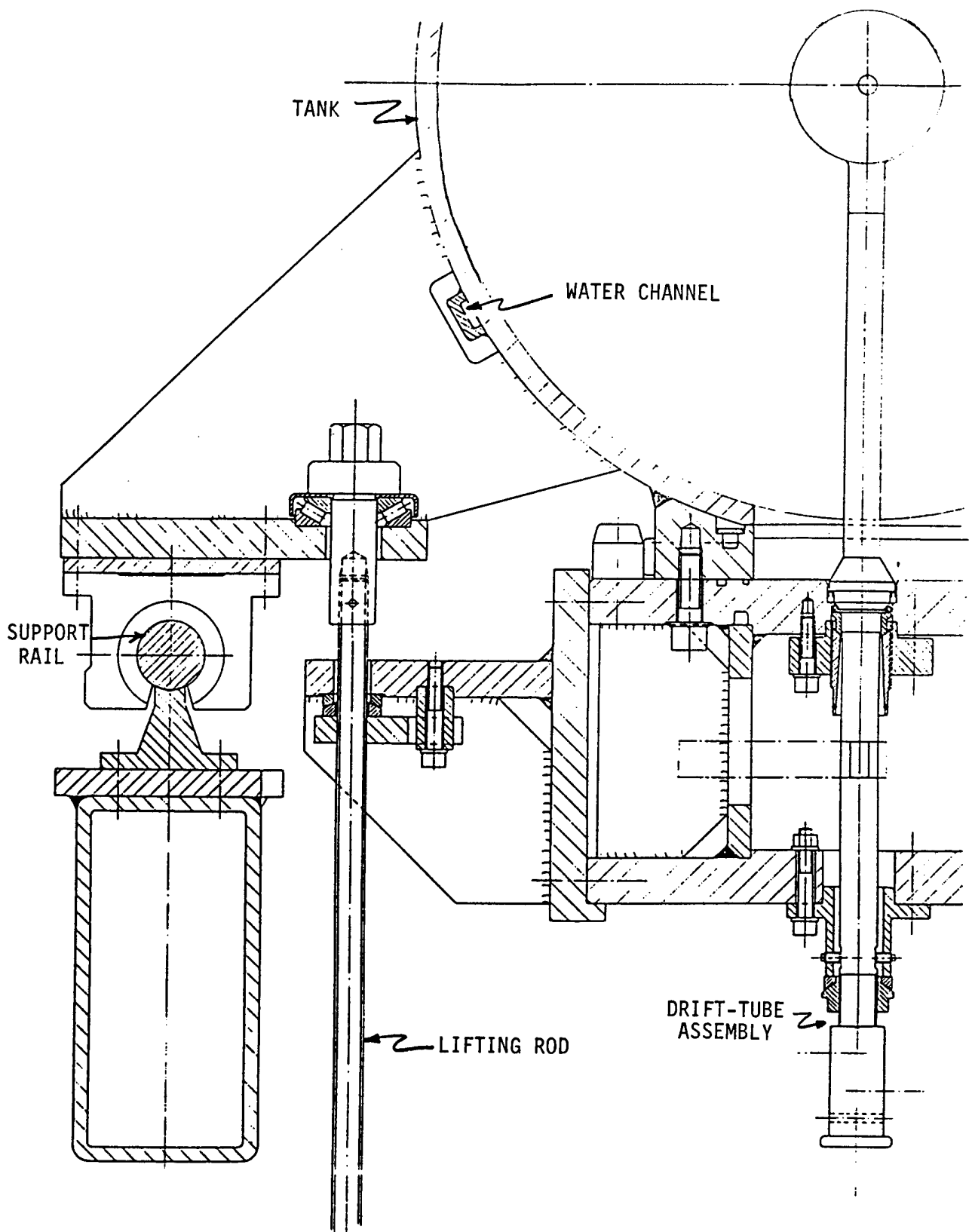


Fig. 66.  
 Drift-tube mounting beam and DTL mounting detail initial design study.

Outside checkpoints for drift-tube position

- 1 y-axis
- 2 x-axis
- 3a } z-axis (cell length)
- 3b }
- 4 rotation around y-axis

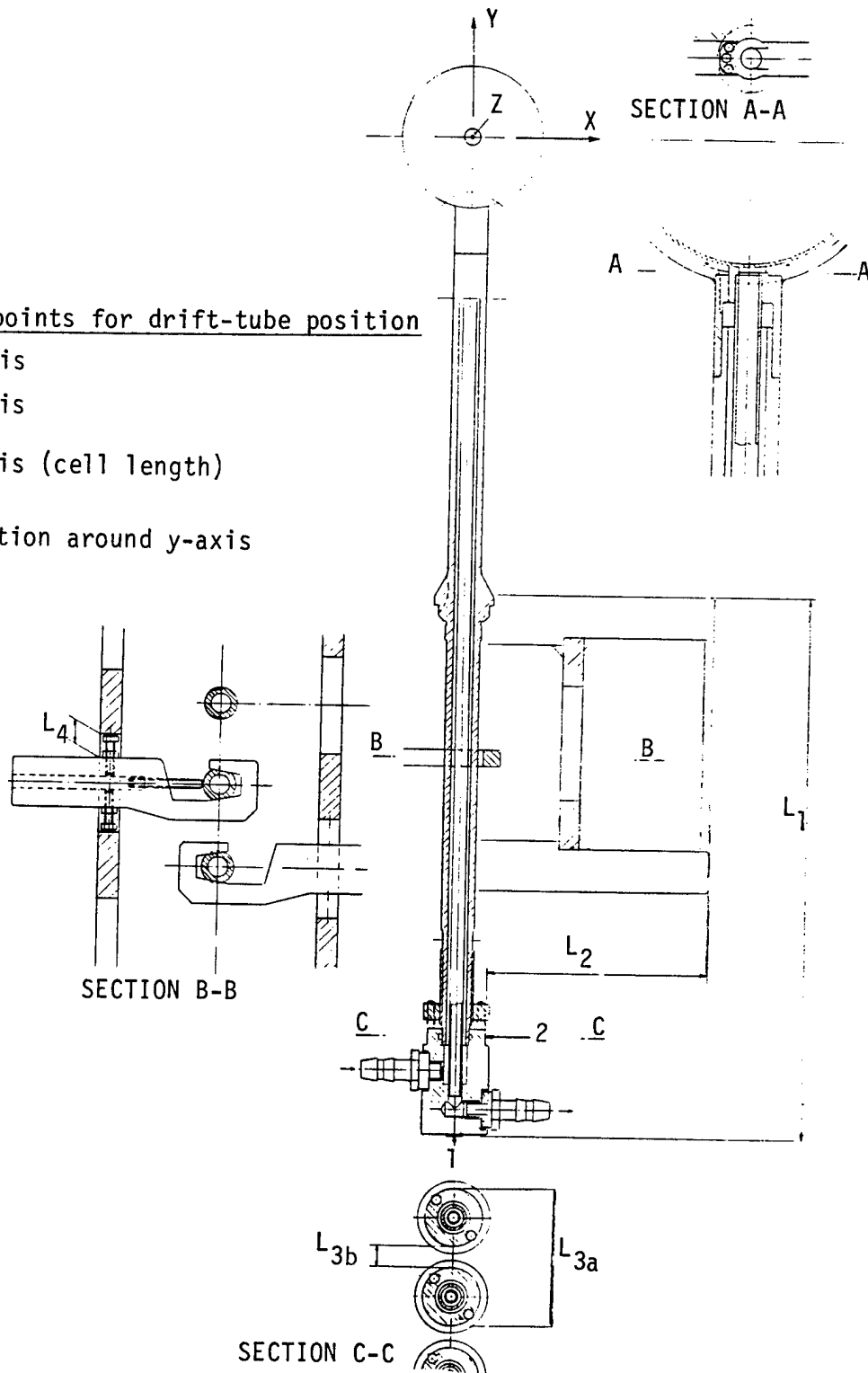


Fig. 67.  
Drift-tube-stem initial design study.

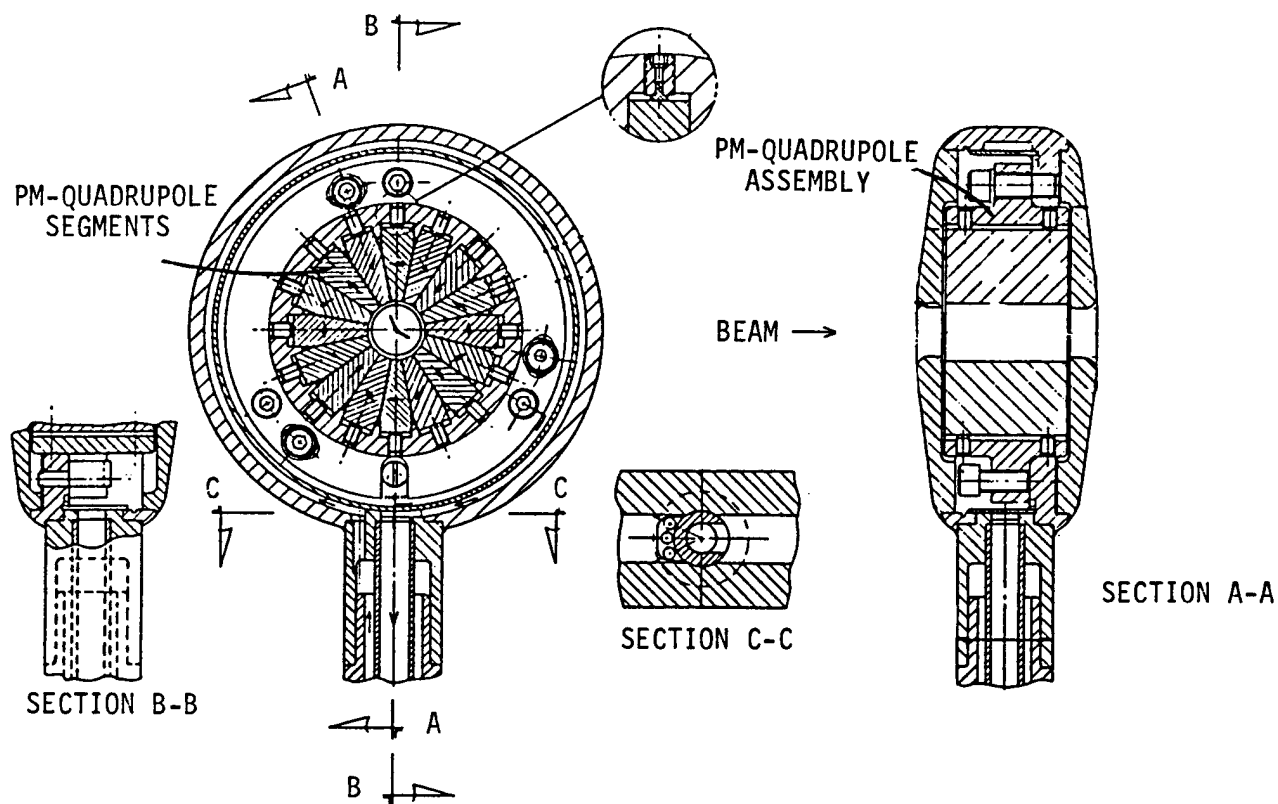


Fig. 68.  
 Drift-tube PM-quadrupole arrangement, Configuration No. 1, initial design study.

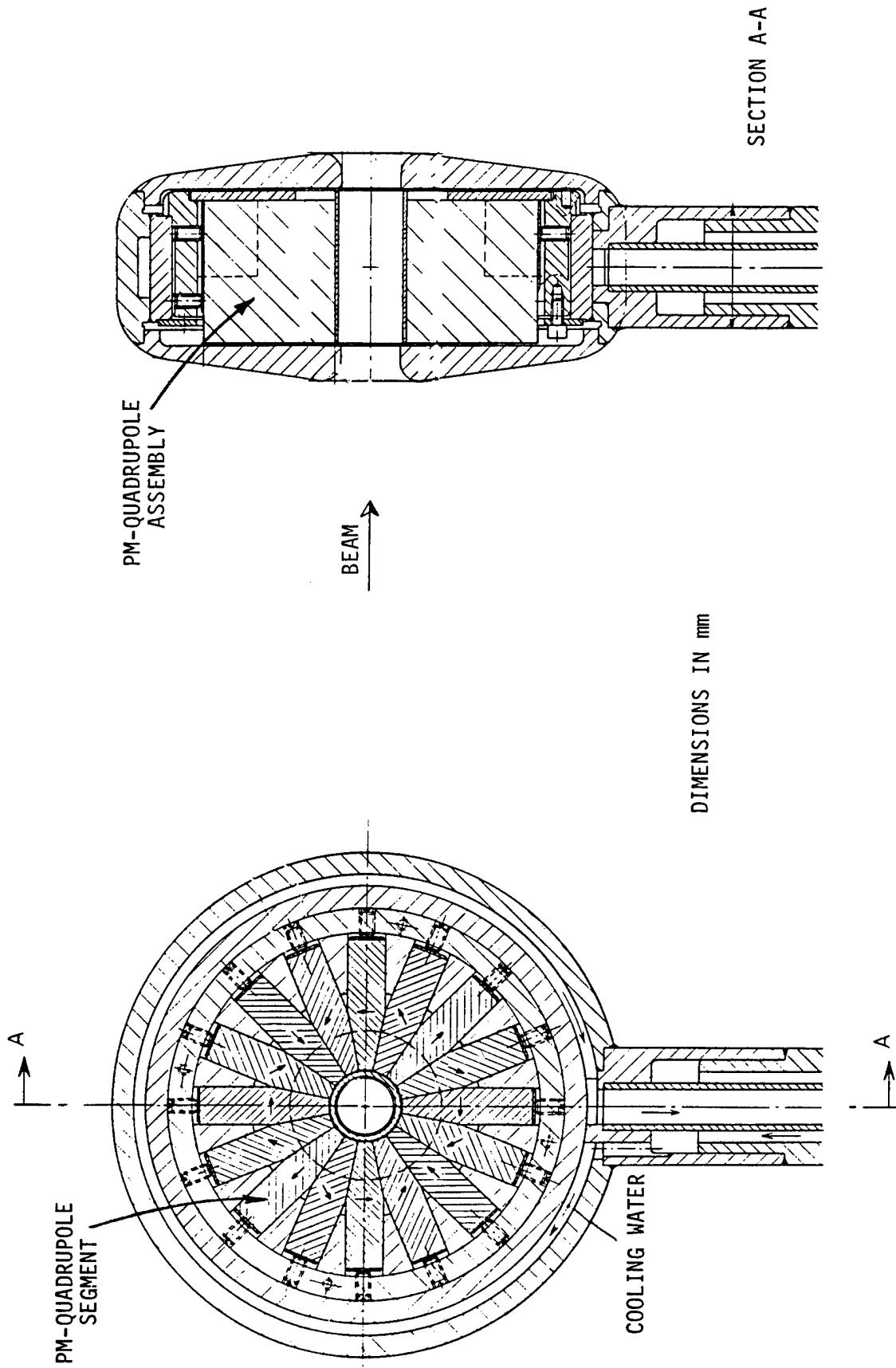


Fig. 69.  
Drift-tube PM-quadrupole arrangement, Configuration No. 2, initial design study.

## VII. SLUG TUNERS

Two slug tuners are used to tune the drift-tube tank. The slug-tuner design (Fig. 70) incorporates features of the 201-MHz LAMPF tuners and the 80-MHz FMIT tuners. The tuners have stepper-motor actuators to permit remote closed-loop tuning, if required. Water-cooling is provided through the tuner-actuator shaft.

## VIII. POST COUPLERS

Twenty post couplers, located on every other drift tube, are provided for stabilizing the rf electric field to the drift tube. The post-coupler stem provides water-cooling channels for the post shoe and stem. The post can be manually inserted, radially, and rotated by independent motions. The detailed design and shape (Fig. 71) are scaled from the LAMPF post coupler by the ratio of the LAMPF frequency to the ATS frequency.

## IX. ASSEMBLY, ALIGNMENT, AND HANDLING

The concept of using one mounting beam permits the alignment of the 39 drift tubes to be performed outside the tank, with precision optical and mechanical instrumentation. Optical tooling and fixtures will be used to position the end drift tubes. After completion of positioning and alignment, precision mechanical gauges will be used to determine the "as-aligned" position of each drift tube and the atmosphere side of the drift-tube stem. The drift-tube beam assembly then will be removed from the assembly dock and mounted on a transporter dolly, which will be used to position the beam assembly under the prepositioned and aligned DTL tank. The beam assembly will be lifted into position in the tank by four elevator assemblies, one on each end of the beam. Figure 72 illustrates the steps for alignment and assembly into the drift-tube tank.

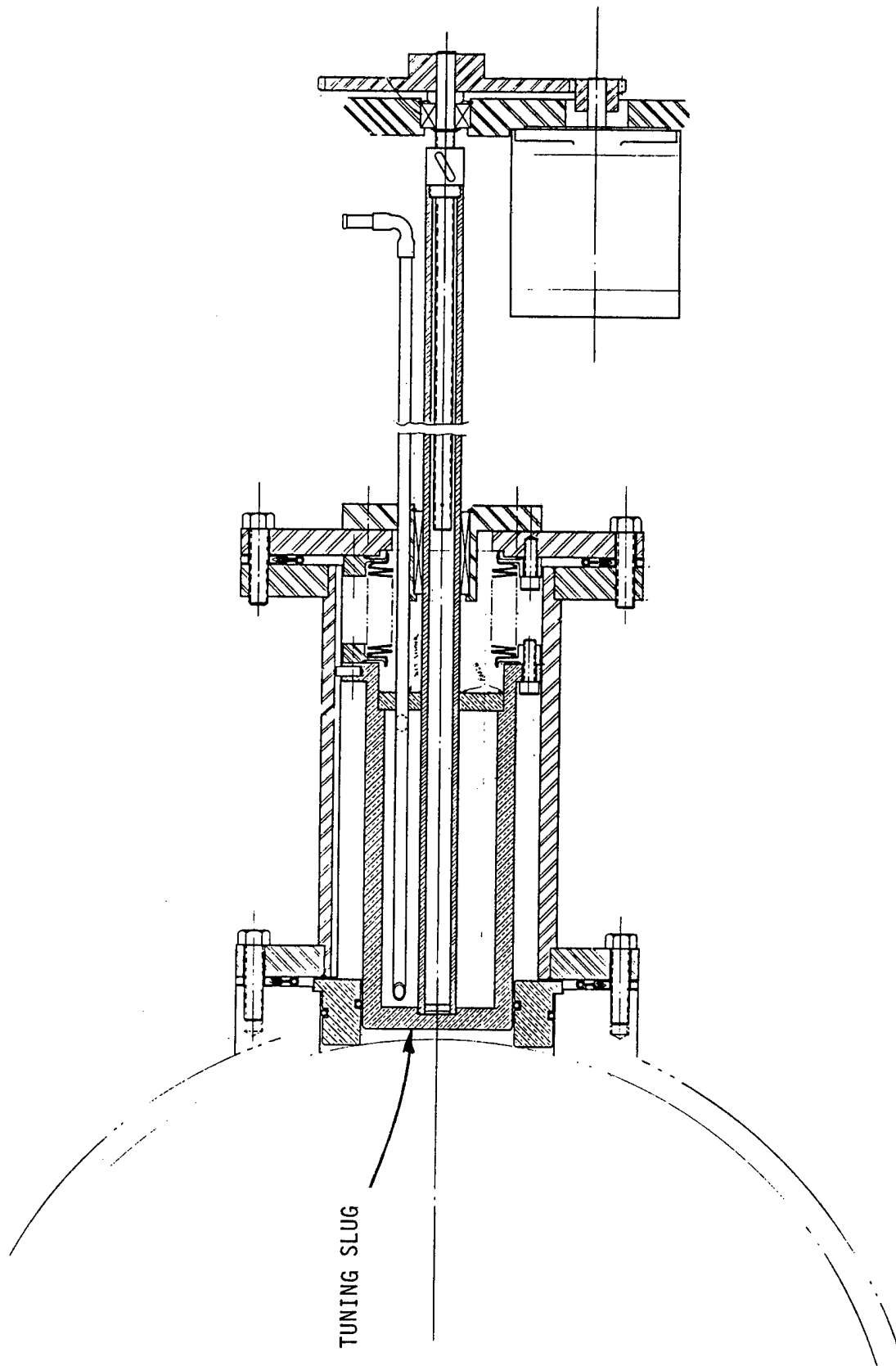


Fig. 70.  
The ATS DTL slug-tuner initial design study.

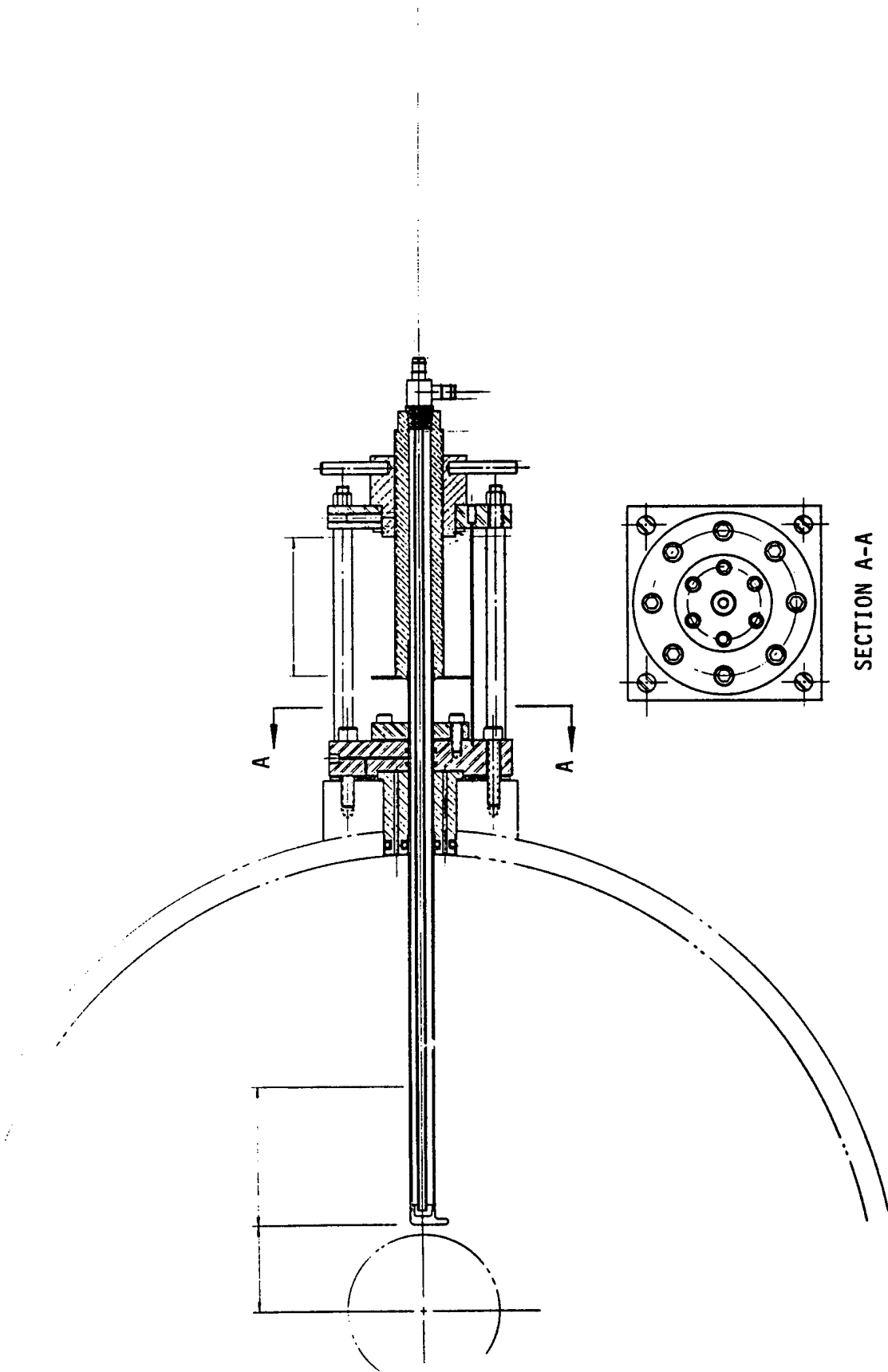


Fig. 71.  
The ATS DTL post-coupler initial design study.

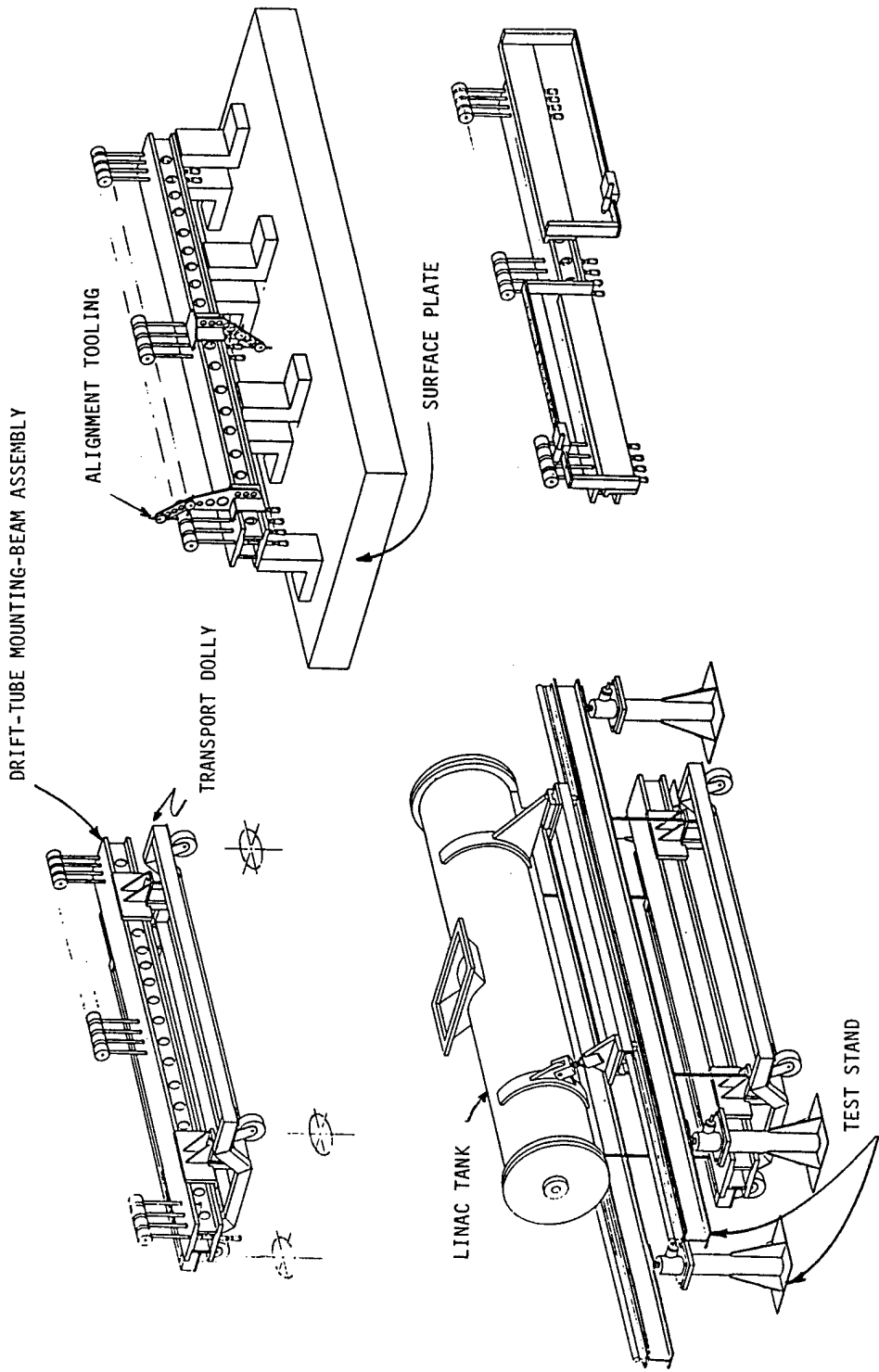


Fig. 72.  
The ATS DTL assembly, alignment, and handling concepts initial design study.

## RFQ DESIGN AND FABRICATION

### I. BACKGROUND

The construction and operation of the POP RFQ for the Pion Generator for Medical Irradiation (PIGMI) Project clearly demonstrated the utility of rf-manifold-driven vane structures. Application of fabrication and construction techniques, similar to previous rf accelerators at Los Alamos, was successfully employed in the POP, including those applications involving plating, brazing, welding, etc. The design of the ATS RFQ began with the intent to make maximum use of this foundation of earlier technology; however, several features of the ATS RFQ make important departures from the POP work: plated-steel structures, one-piece vane base/vane tips, demountable vane-base/vane-cavity-cylinder assembly, two-section cavity vane-base assembly, and reduced dependence on brazed assemblies. Detailed design activities were in progress by late 1980. Because of the previous work and the importance of timely progress and minimum cost, it was concluded that design of a working accelerator, omitting the intermediate step of constructing a full-scale prototype, was an acceptable risk. In short, it was accepted that the working ATS RFQ would be a working prototype.

ATS RFQ physics design parameters of particular importance to the RFQ engineering design are shown in Table VIII.

Detailed RFQ design is based on these characteristics and on AT-29 SUPERFISH calculations that validated the detailed shape of the vanes. A cold model of the rf-manifold vane-cavity assembly based on these parameters was constructed and tested in early 1981; results validated the design calculations and manifold-end-capacitor configuration.

### II. DETAIL DESIGN

Based on previous experience with the POP accelerator, a  $\pm 0.002$ -in. tolerance for alignment and fabrication of the vane assemblies was accepted as a primary design constraint. Using this tolerance and the approach to assembly

TABLE VIII

ATS RFQ DESIGN PARAMETERS  
(SUPERFISH RUN AT-29)

Frequency	425 MHz
Length	289.23 cm
Average radius( $r_o$ )	0.394 cm
Tip radius ( $r_s$ )	0.270 cm
Modulation ( $m_f$ )	1.830 cm
Number of cells	356
Vane voltage	111.34 kV
Maximum surface field	43.59 MV/m (2.06 Kilpatrick)
Peak structure power	551 kW
Peak-power manifold and structure losses	327 kW
Peak beam power at 100 mA	190 kW
Duty factor	1%
Repetition rate	10 to 12 Hz

being developed in the design process, dimensional component tolerances were chosen that were expected to produce the required positional accuracy. This parameter subsequently was observed to be of critical importance to this RFQ.

The rf characteristic of  $Q$ , a measure of circuit losses, also is of major importance to the successful operation of any rf device. In this device, an overall  $Q$  of at least 6000 is considered necessary to allow the RFQ to be driven adequately to produce the accelerating gradient required to provide the design beam dynamics. Surface conductivity (plating) and all current-carrying joint conductivities are important to achieve the  $Q$  required. A theoretical

vane-cavity Q of 8000 was calculated, using practical values of surface conductivities, etc. Previously, copper-plated steel had produced acceptable surface characteristics. Assembly joint designs were not well proven and, therefore, were subject to further design evolution for the ATS RFQ. In particular, the earlier use of brazed structures, successfully used in many assemblies, did not appear practical for the ATS RFQ structures; therefore, development of a different assembly method was necessary. Of particular importance in this regard was the strong desire to provide a demountable, adjustable joint between the vane base and the RFQ cavity cylinder that could provide high electrical conductivity to assure the required Q of 6000.

The RFQ's 289.23-cm length placed several limitations on the detail design because of available manufacturing capability inside and outside the Laboratory. Of particular significance were the conclusions that (1) brazing of a vane tip to the vane base was not practical, and (2) the vanes and vane-cavity cylinder should be in two sections because of length limitations in vane-tip machining and drilling capabilities. In the case of vane-tip machining, the computer-controlled milling machine's 48-in. table required repositioning each of the two vane sections on the machine's table.

Because of the lower duty factor (1%), cooling has been provided only for the RFQ vane-cavity assembly, which has cooling channels in each vane and in the wall of the cavity cylinder. Although evolution of the overall RFQ design is a continuing process, the evolution of the vane-base/vane-cavity-cylinder joint is of particular interest. The POP accelerator used brazed joints; therefore, this approach was explored first. Because of the RFQ's 289.23-cm length, the requirement for retaining alignment accuracy while inside a long furnace, and the desired ability to demount and/or move vanes, this assembly technique was not practical. Various approaches to a movable joint were investigated. The final choice was a commercially available metal seal that functions as a linear spring to provide a joining interface. Subsequent experience has shown this choice to be suitable but not without problems. Figure 73 shows a cross section of the ATS RFQ vane and cylindrical cavity. Figure 74 shows an overall view of the ATS RFQ assembly.

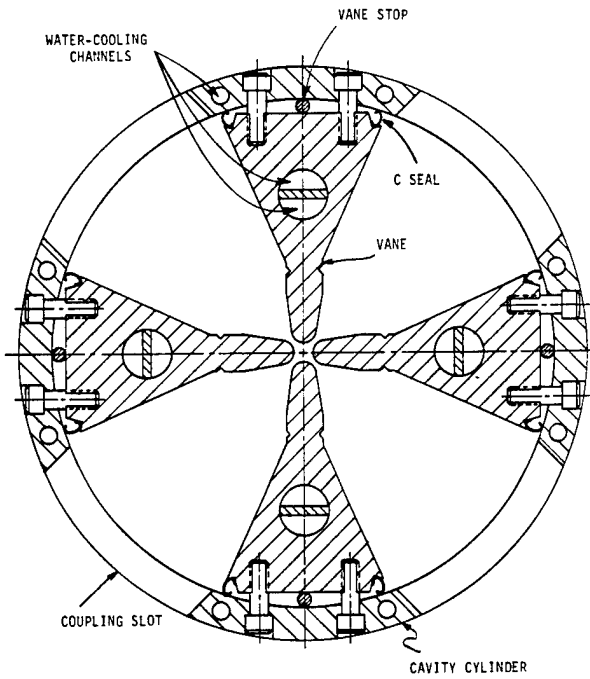


Fig. 73.  
The ATS RFQ cross section.

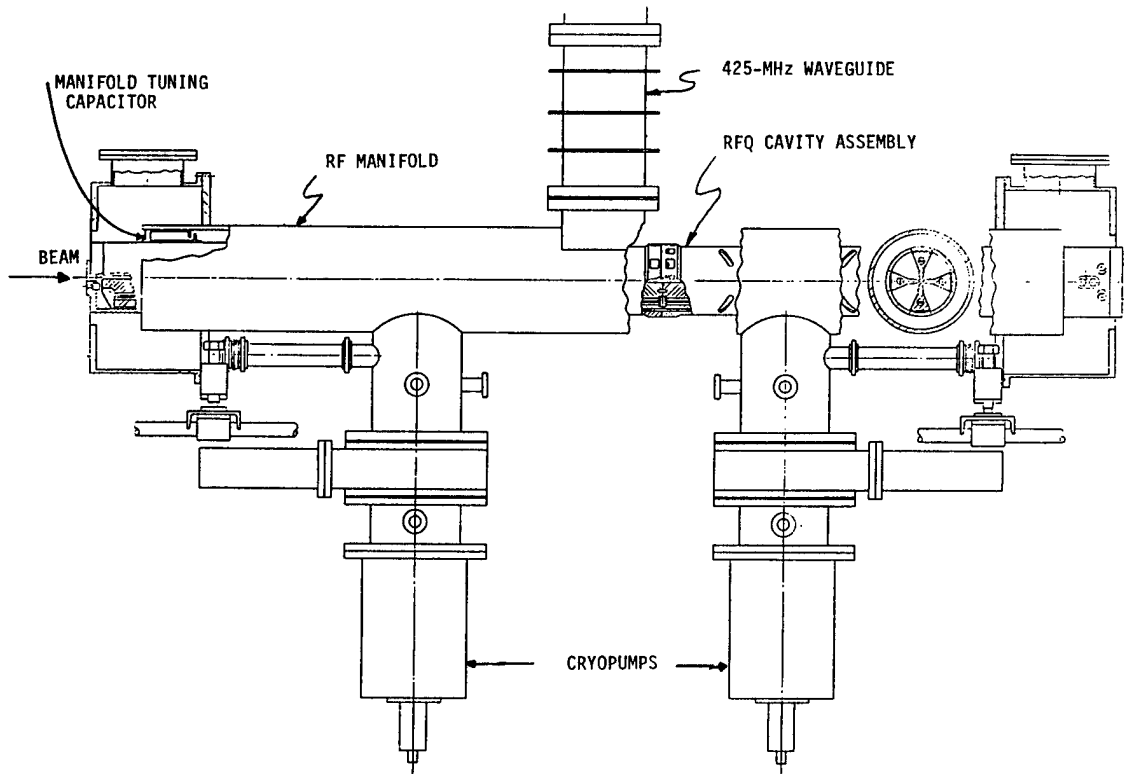


Fig. 74.  
The ATS RFQ assembly.

### III. FABRICATION

The fabrication of the RFQ's various components required the capabilities of several internal Los Alamos facilities, as well as several commercial organizations. The capabilities of each facility are not easily or conveniently available elsewhere. During the fabrication process, some development by the facility performing the work was necessary to meet the requirements. Those fabrication processes of principal importance are described in more detail below.

#### A. Vane Fabrication

Vane fabrication involved several facilities because of various production processes: conventional machining, computer-controlled machining, heat treating, electroplating, precision mechanical inspection, and plating-thickness measurements. The vane blanks were heat-treated at several points in the rough- and finish-machining sequence in various shops of the Laboratory's Mechanical Fabrication Division (MEC) where machine processes included all operations except vane-tip-modulation machining. Vane-tip machining was performed in the AT Division's Branch Shop by a computer-controlled milling machine under the supervision of AT-1. Actual machine operation and setup were performed by MEC personnel. After completion of machining, precision mechanical inspection was performed, followed by bright-acid copper plating in the Los Alamos Chemistry-Materials Science Division (CMB), Group CMB-6. Measurement of the plating thickness was performed by the Los Alamos Dynamic Testing (M) Division.

Vane production to an accuracy of  $\pm 0.002$  in. was used as the fabrication goal. The goal was met in most cases; however, the tip straightness on Vanes 3 and 5 exceeded this limit, as did plating-thickness variation. In both cases, process-development dry runs had been performed to assure accuracy of the parts fabricated. Both times, deviations occurred that will require additional process development to bring the vanes within specifications. The worst case of vane-straightness deviation occurred on Vane 3 and resulted in a 0.0055-in. error; the worst case of plating was a 0.0027-in.-thickness variation from the end to the center of Vane 1, upstream section.

## B. Vane-Cavity Cylinder

To achieve some lead time on fabrication of other RFQ components, the cavity cylinder was placed in fabrication before completion of the detail RFQ drawings. This decision was based on high confidence in preliminary design and layouts performed at the beginning of the detail-design process. The specific process of importance was the drilling of water-cooling channels in the cylinder walls by "deep drilling." These channels are shown in cross section in Fig. 73. Deep drilling was evaluated as the simplest, least costly, and fastest method of providing these cooling channels. The vendor selected to perform the work appeared to possess the required experience, equipment, and reputation, as well as providing the best response time and lowest cost. Difficulties were immediately encountered in producing the required parts; ultimately, incomplete parts were delivered in early June instead of finished parts in early March. Completion (including correction of errors) of the cylinder machining was performed in MEC, followed by honing of the inside diameter in July 1981. Final cavity-slot machining at Los Alamos in late July was followed by copper plating in late October 1981.

## C. The rf Manifold

Fabrication of the rf manifold was accomplished in MEC, followed by considerable surface finishing by AT-Division technicians before copper plating.

## D. C-Seals

The vane-base-to-cylinder interface C-seals are patented, linear-spring sealing devices fabricated of Inconel X-750 in a fully heat-treated condition. This seal, when fully loaded (a condition that requires yielding of the spring), exerts an  $\sim 375$ -lb force per linear inch. Providing these seals in a straight length (instead of circular as an O-ring) required some process development and tooling. Some additional development was necessary at Los Alamos and is continuing to provide better seal straightness. The seals were bright-acid copper-plated at Los Alamos before installation in the RFQ.

## E. Other Components

Of the remaining components, the RFQ cavity-support capacitor assemblies are the principal components of complexity. The assemblies (Fig. 74) provide support for the cavity inside the rf manifold and the tuning capacitor for the

rf manifold. The assemblies are fabricated of copper-plated carbon steel. After copper plating, the capacitor components are hydrogen-furnace-brazed with copper/silver eutectic filler material.

#### F. Vane Installation

In the vane installation, assembly jigs prepositioned the vanes for insertion into the cavity cylinder. After we placed the vanes in each of the two vane-cavity sections and loosely fastened them into position, we joined the two sections at the center mounting ring. The C-seals then were inserted into the notches in the vane bases. Next, the vanes were positioned in the cavity, using end-alignment fixtures to evaluate quadrature positioning and Kel-F pin gauges to determine intervane spacing. The initial C-seal installation and vane-positioning procedures revealed an unexpected "lock-up" condition of the seal in the locating notch. The lock-up condition caused overcompression of the seal and a loss of seal "spring-back," with a resultant inability to adjust the vanes as planned. Although these difficulties were encountered, the vanes were placed on mechanical quadrupole symmetry with an accuracy of 0.0015 in. In February, an initial effort to determine the tune of the RFQ cavity demonstrated the presence of quadrupole-mode excitation and a Q of  $\sim 6000$ , but with serious field-peaking asymmetry and dipole-mode mixing. The inability to adjust the vanes, necessary to level the field, and the inability to minimize the dipole modes prevented the tuning from proceeding at this time. A revised method of positioning the C-seal, where a locating wire was attached to the seal, permitted the seal to flex as planned. The revised seal configuration resulted in achieving the required quadrupole mode with a Q of greater than 7500 and a resonant frequency of  $\sim 424$  MHz. Subsequent tuning measurements and adjustment procedures revealed an extreme sensitivity to vane position, 0.0001 to 0.0002 in., and an inability to produce the desired flat field from the upstream-to-downstream end of the vanes. Also, it was observed that the vane's required radial position again resulted in overcompression of the C-seal. To limit C-seal compression and to provide positive mechanical position, a solid-rod "stop" (with shims tailored for each vane according to previous tuning-measurement data) was installed between the vane base and the cavity-cylinder wall. As thus assembled, a quadrupole/dipole-mode field distribution has been achieved that is expected to accelerate beam with a vane assembly Q of over 6000 at 423.44 MHz.

#### IV. RFQ INSTALLATION ON ATS

The RFQ as previously tuned was installed on the ATS on July 20. Installation of all cooling systems, vacuum systems, and RFQ systems was completed August 11. The rf power was applied for the first time August 12; tuning of the rf system, required to match the rf power supply to the RFQ, was completed with 1-kW power applied August 12. Power conditioning of the RFQ was accomplished in very short time with a 775-kW forward power and 700- $\mu$ s pulse width at 10 Hz achieved August 27. The RFQ, operating in this mode, demonstrated stable operation after advancement through a number of power levels, where fast discharges were observed followed by zones of stable operation. The RFQ vacuum levels observed throughout the conditioning process ranged from a minimum pressure of 3 to 4 x 10<sup>-8</sup> torr to a maximum of 5.8 x 10<sup>-7</sup> torr during rf structures discharge. The conditioned RFQ was integrated into the ATS beam transport and was placed in operation September 3. Integration of all rf, beam transport, ion source, and vacuum systems is in progress.

#### V. MANIFOLD/VANE-CAVITY INTEGRATION AND TUNING

Manifold/vane-cavity integration was performed after completing the vane alignment and tuning at the vane cavity. Tuning of the manifold with the vane-cavity-cylinder support-capacitor assembly was performed in the AT-Division rf structures laboratory. Adjustment of the capacitors required 5 wk to accommodate modification of the capacitor tuning plates, after it was concluded that a stronger-than-expected coupling between the vane-cavity assembly, manifold, and waveguide vacuum assembly resulted in lower-than-expected resonant frequency of the combined assembly. The modifications, although not difficult, were done with great care because of the very high electric fields and high currents that will exist in the capacitor. The final manifold and tuning resulted in a low-power, 424.644-MHz, resonant frequency with 12% stored energy in the manifold and 88% stored energy in the vane cavity.

## THE ACCELERATOR TEST STAND rf SYSTEM

An rf system consisting of an L-3694 klystron, its solenoid and modulator, a high-voltage power supply, a capacitor bank and crowbar, a waveguide system, a control and interlock system, and a deionized water system has been assembled and tested into a water load. Figure 75 shows the block diagram of the rf system that can produce 1.25 MW of rf power at any frequency between 400 and 450 MHz. The system is operational and routinely has produced 1.1 MW at 1000 ms into a water load at 86 kV. The average power is limited to  $\sim 25$  kW because the power supply is driven by a 90-A Variac, rather than a system rated for the full power of the supply. The high voltage also is limited to 86 kV because of corona in the capacitor room. Provisions have been made to pressurize the capacitor enclosure with sulfur hexafluoride so that higher voltages, up to 110 kV, may be supplied to the klystrons. This should raise the output power to 1.5 MW.

The entire system has been operated with a closed amplitude loop for hours at a time into a water load, and no problems are expected when the system is connected to the RFQ. The primary power system should be upgraded in FY 83 to include a larger, oil-filled, capacitor enclosure and a larger Variac to make the full-rated power of the klystron available for the RFQ.

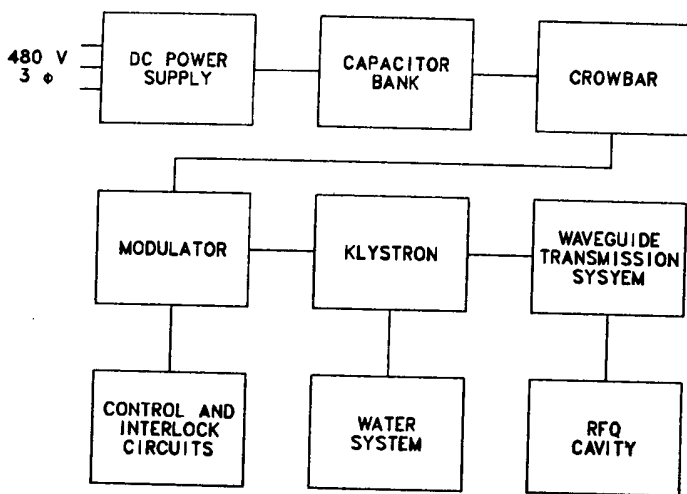


Fig. 75.  
ATS rf system block diagram.

## ATS COMPUTER CONTROL AND DATA-ACQUISITION SOFTWARE

### I. STATUS

We have created and implemented a software subroutine package to expedite activities on the ATS. The software package is a data-base-oriented system that stores all pertinent information required to run and acquire data from the ATS. So far we have spent 8 man-months on this effort.

The software goals include numerous requirements imposed by the individuals associated with the ATS. To be effective, the package must be easy to use, reliable, helpful in preventing mistakes and correcting errors, and must accomplish the desired tasks. In addition, the software must prevent conflicts among various experimenters, maximize the speed for performing experiments, and keep costs to a minimum. The data base itself has complete information about the system. The information serves for access as well as for modification. The future utility of the code is an important consideration and will be guaranteed. The software will be easy to modify and maintain as system requirements change. We expect that most change requests will be handled by modifying entries to the data base; but there will be requests that will require modifications to the code itself, and these requests must be honored and anticipated. Finally, the viability of the code does not depend on certain key personnel remaining with the Group.

To achieve a high-quality system in a minimum amount of time, additional constraints were placed on the system by its designers. A specification, given in this report, was written and followed, setting minimum standards for documentation and coding. The final result is a control and data-acquisition computer code that, structurally, is simple and easily understood. A large amount of testing and error checking has been done on this code, which has confirmed that the software is easily debugged and modified where necessary.

A preliminary version of this software package has been used to perform an emittance scan using an electrostatic deflection-plate device. The software performed as designed with almost no modification needed to take the system from the development computer (VAX with no CAMAC capability) to the ATS control computer. The complete system with the data base is now undergoing final acceptance testing before full implementation on the ATS.

Some of the commands available to the user are shown in Figs. 76 through 78. These routines are classified as data transfer (Fig. 76), device movement (Fig. 77), and general purpose (Fig. 78). Our next major task is to write a users' guide and a software-documentation manual. We will combine various test routines into a single test package for testing new and/or modified codes for correctness. Existing software soon will be modified to use the new subroutine library package.

## II. CODE DEVELOPMENT FOR BEAM-DYNAMICS CALCULATIONS

A subroutine (PERFLD) was written that calculates perturbation effects for two-dimensional symmetric multipoles (electric or magnetic).<sup>1</sup> The subroutine uses the algorithms and tasks from K. Halbach.<sup>2</sup> The perturbations considered are error excitation, pole displacement, and rotation. This subroutine will be used in the RFQ and DTL dynamics codes.

### **SUBROUTINE AREAD (DEVNAM, ARRAY, DIMEN, ERROR)**

**THIS SUBROUTINE READS AN ARRAY OF VALUES FROM THE DEVICE (DEVNAM) USING THE APPROPRIATE CAMAC DEVICE HANDLER. THESE VALUES ARE SCALED WITH THE APPROPRIATE FACTOR OBTAINED FROM THE DATA BASE, THEN OUTPUT AS (ARRAY)**

### **SUBROUTINE AWRT (DEVNAM, ARRAY, DIMEN, ERROR)**

**THIS SUBROUTINE WRITES AN ARRAY OF VALUES TO THE DEVICE (DEVNAM) USING THE APPROPRIATE CAMAC DEVICE HANDLER. THESE VALUES ARE SCALED WITH THE APPROPRIATE FACTOR OBTAINED FROM THE DATA BASE, THEN OUTPUT TO THE DEVICE**

### **SUBROUTINE WRECV (DEVNAM, WORD, ERROR)**

**THIS SUBROUTINE READS A VALUE FROM THE DEVICE (DEVNAM) USING THE APPROPRIATE CAMAC DEVICE HANDLER. THIS VALUE IS SCALED WITH THE APPROPRIATE FACTOR OBTAINED FROM THE DATA BASE, THEN OUTPUT AS (WORD)**

### **SUBROUTINE WSEND (DEVNAM, WORD, ERROR)**

**THIS SUBROUTINE WRITES A VALUE TO THE DEVICE (DEVNAM) USING THE APPROPRIATE CAMAC DEVICE HANDLER. THIS VALUE IS SCALED WITH THE APPROPRIATE FACTOR OBTAINED FROM THE DATA BASE, THEN OUTPUT TO THE DEVICE.**

Fig. 76.  
Data-transfer user commands.

**SUBROUTINE DVIN(DEVNAM, ERROR)**

THIS SUBROUTINE MOVES THE DEVICE (DEVNAM) TO THE IN-LIMIT LOCATION. THE CURRENT POSITION WORD IS UPDATED TO THE IN-LIMIT POSITION.

**SUBROUTINE DVOUT(DEVNAM, ERROR)**

THIS SUBROUTINE MOVES THE DEVICE (DEVNAM) TO THE OUT-LIMIT LOCATION. THE CURRENT POSITION WORD IS UPDATAED TO THE OUT-LIMIT POSITION.

**SUBROUTINE DVMOVE(DEVNAM, DISTANCE, ERROR)**

THIS SUBROUTINE MOVES A DEVICE A DISTANCE  $\pm$ (DISTANCE). A CALL TO (CONFLT) IS MADE TO CHECK FOR CONFLICTING DEVICES. THE CURRENT POSITION DATUM IS UPDATED.

**SUBROUTINE DVLOCA(DEVNAM, LOCATION, ERROR)**

THIS SUBROUTINE TAKES A DEVICE NAMED (DEVNAM) AND PLACES IT AT LOCATION (LOCATION). THE DEVICE IS MOVED FROM ITS CURRENT LOCATION DIRECTLY TO THE DESIRED LOCATION. THE CURRENT POSITION DATUM IS UPDATED.

Fig. 77.  
Device-movement user commands.

**SUBROUTINE DVINIT (DEVNAM, ERROR)**

LOAD THE APPROPRIATE COMMON BLOCKS FROM THE DATA BASE FOR THE GIVEN DEVICE (DEVNAM) AND INITIALIZE CAMAC.

**SUBROUTINE STATUS (MODE, DEVNAM, PARNAM, VALUE, ERROR)**

THIS SUBROUTINE UPDATES OR RETURNS A PARAMETER VALUE (VALUE) FOR A DEVICE (DEVNAM) AND PARAMETER (PARNAM).

Fig. 78.  
General-purpose user commands.

### III. FORTRAN PROGRAM AND SUBROUTINE SPECIFICATIONS

This section describes suggested rules to be followed in writing software for the ATS. The goals of this specification are to define a standard that is easy to implement and to achieve software that is easy to debug, use, understand, modify, and maintain. The software should be reliable, adaptable, structurally simple, portable, and so well documented that the Programmer's Golden Rule, "The demise of a programmer should not necessitate the death of his code," can be demonstrated.

The ANSI FORTRAN 77 standard has been adopted as the software implementation language on the ATS. This choice was made because in most cases it is the only language known to individual members associated with the ATS. We recognize that there may be more suitable languages for instrumentation and control but that currently the time investment needed to learn a new language is prohibitive. One major advantage of some languages is that they force programmers to write code that achieves the goals described earlier. The major weakness of many FORTRAN programs can be ascribed to a combination of lack of documentation, excessive cleverness in using complex logic, the use of COMMON, and unrestricted use of GO TO.

The next section contains rules to be followed in writing FORTRAN programs for the ATS. The list of rules is intentionally short and is meant to eliminate the most glaring deficiencies in FORTRAN programs. A hypothetical subroutine example is presented to highlight the desired level of documentation (Fig. 79). Several books dealing with the subject of writing structured FORTRAN (program code that achieves the goals listed in the section "Status") are available from various sources at Los Alamos.

```

1      SUBROUTINE BEMCUR( VARIABLES )
2      C
3      C WRITTEN BY E.A.WADLINGER, 30-DEC-81
4      C
5      C MODIFICATIONS
6      C
7      C     15-JAN-82 BY O.SANDER TO CORRECT
8      C     MISPELLING OF VARIABLE 'CURRENT'.
9      C
10     C     5-FEB-82 BY D.RUSTHOI TO ADD
11     C     PLOTTING FEATURE.
12     C
13     C PURPOSE
14     C
15     C     THIS SUBROUTINE CALCULATES THE PROTON
16     C     BEAM CURRENT WHICH APPEARS IN A
17     C     TRANSCENDENTAL EQUATION WHICH IS
18     C     SOLVED BY NEWTON'S METHOD.
19     C
20     C WARNINGS
21     C     NONE
22     C
23     C USAGE
24     C     CALL BEMCUR( VARIABLES )
25     C     INPUT(BIAS,FARDAY,...,UARN)
26     C     OUTPUT(UARN+1,...)
27     C     REAL PARAMETERS BIAS,SCALE,...
28     C     INTEGER PARAMETERS FARDAY,...
29     C
30     C VARIABLE DEFINITION
31     C
32     C     BIAS      ; BIAS VOLTAGE ON FARADAY CLIP.
33     C     FARDAY   ; CURRENT READ FROM FARADAY CLIP.
34     C     SCALE    ; SCALE FACTOR FROM CALIBRATION.
35     C     BEMCUR  ; CALCULATED BEAM CURRENT.
36     C
37     C SUBROUTINES REQUIRED
38     C     NONE
39     C
40     C LOCAL VARIABLE GLOSSARY
41     C
42     C     BEPMNEW  ; NEW ITERATED VALUE OF CURRENT.
43     C     BEPMOLD  ; OLD ITERATED VALUE OF CURRENT.
44     C     I,J,K    ; ITERATION INDICES.
45     C
46     C *****
47     C
48     C FORTRAN CODE
49     C     MIX SUFFICIENT COMMENTARY WITH THE SOURCE
50     C     CODE TO IDENTIFY THE PURPOSE OF EACH
51     C     FORTRAN STATEMENT.
52     C
53     C RETURN
54     C     END

```

Fig. 79.  
A hypothetical subroutine.

#### IV. FORTRAN RULES

1. Only ANSI standard FORTRAN-77 should be used. Compiler-specific extensions should be strictly avoided where possible.
2. A subroutine should perform one and only one conceptual task (for example, matrix inversion, matrix multiplication, calculate Courant-Snyder ellipse parameters, address a particular species of CAMAC module, etc.).
3. The subroutine's documentation should be included as part of the source code. The following should be included in the header (first few lines of code):
  - a. Author's name and program creation date.
  - b. Modification list (author's name, modification date, and purpose).
  - c. Purpose of the subroutine.
  - d. Warnings pertaining to the subroutine use: special hardware requirements, use of COMMON, other subroutines that must be called before usage, internal input/output (I/O).
  - e. Usage--how to call and use this program.
  - f. Definition of all variables issued through a call statement.
  - g. Definition of all COMMON variables. (Use of COMMON is discouraged.)
  - h. Definition of all local variables.
  - i. List of all subroutines required.
  - j. Mathematical properties (accuracy, convergence conditions...).
  - k. Computer memory requirements (only if the author feels that memory requirements will be large because of big internal storage arrays, etc.).

Comments in the code should state exactly what calculation is being performed. If a reference exists that describes details of a nonobvious calculation, the reference should be cited.

4. The use of multiple subroutine entry points or directed exits is strongly discouraged. Use of these techniques rapidly leads to a structural nightmare.

5. Blank COMMON should be strictly avoided. Each word in a COMMON block is a potential source of unexpected interaction between different parts of a program. This produces code that is very difficult to debug, modify, maintain, and understand.
6. Use of labeled COMMON is discouraged but might find use in small structural blocks of subroutines as a means of internal communication with variables that should be transparent to a user. (PLOT10 uses such a device for this purpose.)
7. Program code should be written so that it flows mostly monotonically from top to bottom.
8. DO loops and IF-THEN-ELSE constructs should be used in place of GO TOs where possible. GO TO statements, if improperly used, can greatly increase program complexity.

Example:

```
IF (I.EQ.0) THEN
  A = B + C
  D = A + E
ELSE
  A = 0.0
  D = 0.0
END IF
```

versus

```
IF (I.NE.0) GO TO 10
  A = B + C
  D = A + E
GO TO 20
10 A = 0.0
   D = 0.0
20 CONTINUE
```

Both sets of computer code in the example perform the same function. However, the code with GO TOs contains labels that could be addressed from other parts of a program. If someone later decides to modify the code with the GO TOs, he cannot be certain (without reading the entire program accessible to the labels) whether the original author intended the IF-THEN-ELSE construct or otherwise.

9. The following example demonstrates the only allowed use of a computed GO TO. The comments in the example must be included in the program. This emulates a structured CASE statement.

Example:

```
C THE FOLLOWING COMPUTED GO TO = CASE STATEMENT
GO TO (10, 20, 30, ...), I
C CASE STATEMENT LABEL, EXTERNAL ENTRY FORBIDDEN
10 A = B + C
GO TO 100
C CASE STATEMENT LABEL, EXTERNAL ENTRY FORBIDDEN
20 A = B * C
GO TO 100
C CASE STATEMENT LABEL, EXTERNAL ENTRY FORBIDDEN
30 A = B ** C
GO TO 100
*
*
*
C TERMINAL LABEL OF CASE STATEMENT
100 CONTINUE
```

The first comment identifies the computed GO TO as a CASE-statement structure. The labels used in the computed GO TO may be accessed only from this particular GO TO and nowhere else. Each case in the structure must end with a GO TO that goes to a common terminal point.

10. All input and output (READ or WRITE, etc.) for a program should be performed from a centralized location, that is, from subroutines written specifically for performing I/O. Documentation at the beginning of a subroutine must define clearly the I/O for those subroutines that perform these functions.
11. Checks for errors should be performed at appropriate locations in the subroutines. An error-flag variable in the subroutine call-list parameters, to indicate error conditions, should be implemented. The slight increase in execution time for error checking should result in a vastly decreased program debugging time and much more reliable software.

#### REFERENCES

1. E. Alan Wadlinger, "PERFLD: A FORTRAN Subroutine to Calculate First-Order Perturbations for Two-Dimensional Symmetric Multipoles," Los Alamos National Laboratory report LA-9501-MS (August 1982).
2. K. Halbach, "First Order Perturbation Effects in Iron-Dominated Two-Dimensional Symmetrical Multipoles," Nucl. Instrum. Methods 74, p. 147 (1969).

## ATS DATA BASE AND EDITOR

Figure 80 is a functional diagram of the ATS data-base system. The instrumentation, control, and data acquisition (ICA) software maintains a common area in the computer where parameters are stored. These parameters are necessary for the successful execution of the ICA routines. To load this storage area, the interpreter/processor is called and asked to supply specific information from the data-base file. The interpreter knows more about the data-base organization than the ICA software does; therefore, the interpreter knows specifically where to look for the requested information. The data are read from the data-base file in character format; then the interpreter re-formats the numerical data into floating-point values that the working software expects to receive. At execution time, the data in the file are fixed; at other times, however, the information it contains may be updated, augmented, or removed. This is the task of the data-base editor (DBE).

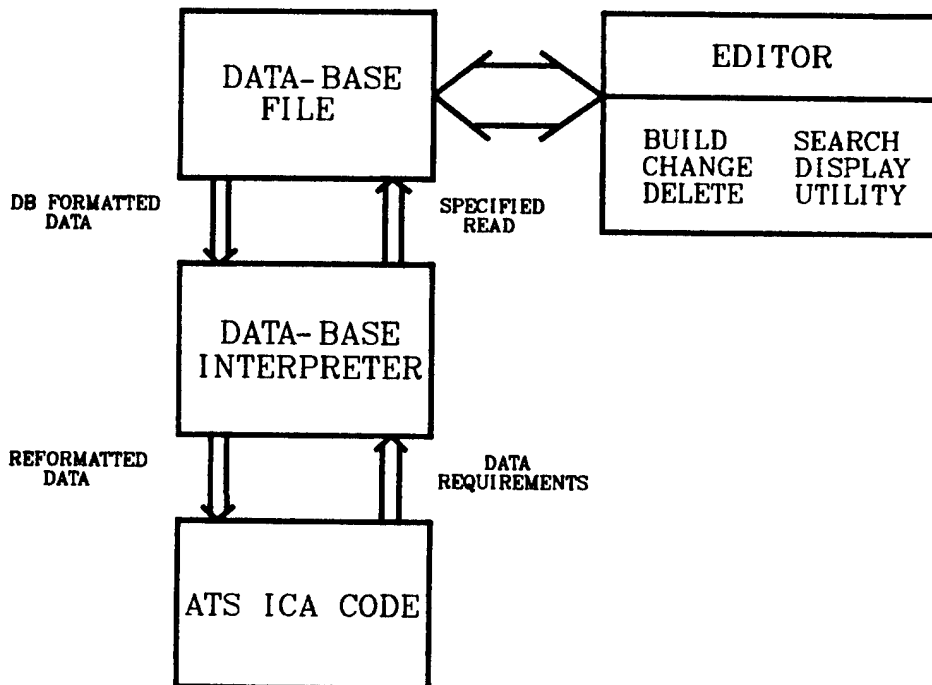


Fig. 80.  
Data-base function.

The DBE can add new records, change information, and delete records. It also is powerful enough to search and display information that is needed by a user. The editing package consists of five functional modules: BUILD, CHANGE, DELETE, SEARCH, and DISPLAY.

- BUILD prompts for field entries, edits, and finally writes the record into the data base.
- CHANGE locates the target record, edits it, and rewrites it back into the file.
- DELETE simply removes a record.
- SEARCH can locate records with single or multiple common entries and will find all occurrences of a CAMAC address.
- DISPLAY can type one or all records to the terminal or print the entire data-base file to the line printer.

A sixth module, UTILITY, will renumber the primary keys, copy files, or list explanations of I/O errors. An added feature is that the user may request a minimum amount of prompting or explanatory text if he is familiar with the DBE. The DBE's source code is ANSI FORTRAN 77, an accepted standard language, and makes the DBE modifiable by any FORTRAN user. The software is modular, making alterations or additions straightforward.

Currently, the DBE performs properly according to design; with the addition of several more capabilities, it will meet all of the specifications. Planned additions to the editing software include checks for a CAMAC module's existence or possible address conflicts, the ability to change addresses globally--handling crate swapping and module exchanges, and listing a crate's CAMAC hardware on all modules in the system. These additional capabilities will function as protective features and will not impede the DBE's application.

## ATS THEORETICAL SUPPORT

### I. ATS RFQ SIMULATION-CODE IMPROVEMENTS

The ATS RFQ simulation code, which has the three-dimensional space-charge calculation reported last year,<sup>1</sup> has been further improved. Because the space-charge calculation is so time consuming, a multistep procedure was incorporated in which space-charge information is stored for one period. This procedure makes it possible to compute space-charge forces approximately once per period yet take into account the variation, over a period, in these forces. What is neglected here is the change in the variation over the period, not the variation itself.

Integrators suitable for simulations of periodic systems were investigated. High-order methods that take advantage of the near-Floquet form of the solution were not successful because of stability problems. (Making such methods canonical is not easy.) We were, however, able to improve the simple semi-implicit formula by adding two free parameters. Accuracy is adequate for simulations up to  $\sim 200$  rf periods using only eight integration steps per period.

The problem of defining and measuring tunes in periodic nonlinear systems in simulations (and perhaps in experiments) was further considered, with still no satisfactory solution. For a time-constant linear system, there is only one parameter: the oscillation frequency. For a time-constant nonlinear system, the oscillation frequency is a function of the amplitude; this frequency depends on the initial conditions. For a time-periodic linear system, the solution is not periodic but is of the Floquet form. This means it can be factored into two periodic parts. One part contains the frequency of the driving force and its harmonics. The other part is sinusoidal (single frequency). It is this frequency that is called the tune, or betatron, or synchrotron frequency. We attempted to define an analogous tune for periodic nonlinear systems that would be a function of the amplitude or of the Courant-Snyder  $\beta$  function. The tune-amplitude diagram would provide a simple description of an accelerator and would relate tune spreads to particle distributions. For matched beams, space-charge forces would behave similarly so that tune depressions and tune spreads caused by space charge could be defined.

## II. RESULTS OF SIMULATIONS

RFQ phase-space acceptance was calculated by first producing a beam matched to the RFQ at a point where the beam is bunched. This match was accomplished by adiabatically deforming a beam matched to harmonic oscillator external forces. Then this beam was traced back through the buncher to the input of the RFQ; no particles were lost. This result is useful for several reasons. First, the momentum acceptance turned out to be  $\sim 3\%$ , which means several ion sources could be used to feed the RFQ simultaneously if an ion source of the required emittance could not produce enough current. The slight tilt of the axial phase-space ellipse indicates that the radial matching section could be improved slightly or that the input beam should be modified slightly to better match the RFQ acceptance parameters.

It is simpler to machine RFQ vanes with a constant pole-tip radius. Such geometry, however, introduces a dodecapole ( $n = 6$ ) term in the electric fields. An investigation revealed that the effect of the dodecapole term on the dynamics was negligible. (The effect on off-axis beams was not considered, however.)

## III. INVERSE-PROBLEM CALCULATIONS

Paul Channell's method<sup>2</sup> for solving the inverse problem in dynamics has been applied to the RFQ matching section. The problem is to determine the physical system required for transforming a beam matched to a space-dependent focusing system into a beam that is matched to a time-dependent focusing system. The theory is simple to apply, unless we also apply the constraint that the forces in the matching section are proportional to  $\cos(\omega t)$  so that the matching section really is part of the RFQ structure. The resultant nonlinear algebraic equations were solved with a nonlinear optimizer; however, because of the large number of nonlinear variables, good solutions were difficult to obtain. An improvement is being worked on to reduce the large number of nonlinear algebraic equations into a few one-dimensional boundary-value problems. In this way, the nonlinear optimizer still is needed to solve the boundary-value problems, but the number of nonlinear variables is reduced greatly.

#### IV. FAST RFQ SIMULATION CODE FOR DESIGN WORK

A new RFQ simulation code was created by inserting a simple space-charge algorithm into the ATS RFQ simulation code. The linear and cubic parts of the space-charge forces are calculated, at every time step, in terms of particle moments. Thus, the calculation is three-dimensional but only approximate. Both straight simulations and production of well-matched input distributions by adiabatic deformation can be performed. The simulations run quickly and are believed to be sufficiently accurate except in the bunching region where fifth-degree terms in the space-charge forces should be included. The new code produces plots of the rms beam sizes at fixed times in the rf phase; therefore, simulations with matched beams will have smooth graphs. (A mismatch shows up as an oscillation of the beam size with twice the betatron or synchrotron frequency.) New configurations in the parameter variation in an accelerator can be tested to see if they introduce a mismatch. Mismatches are to be avoided because they can lead to emittance growth and particle loss.

The design procedure is the following: start with a certain accelerator and produce a well-matched input beam with the new code by adiabatic deformation then vary the accelerator parameters as a function of distance along the machine, with the goal of improving some characteristic (such as reduced overall length) while making sure that such changes do not introduce a significant mismatch anywhere in the machine. Experience with adiabatic deformation matching has shown that simple adiabatic arguments are of no value in analyzing this situation because, even with a fixed tune, the exact nature of the parameter variation is very important.

#### REFERENCES

1. Accelerator Technology Division, "1981 White Horse Progress Report" (to be published as a Los Alamos National Laboratory LA-series report).
2. P. J. Channell, "Explicit Suspensions of Diffeomorphisms--an Inverse Problem in Classical Dynamics," Los Alamos National Laboratory document LA-UR-82-1658, submitted to J. Math. Phys.

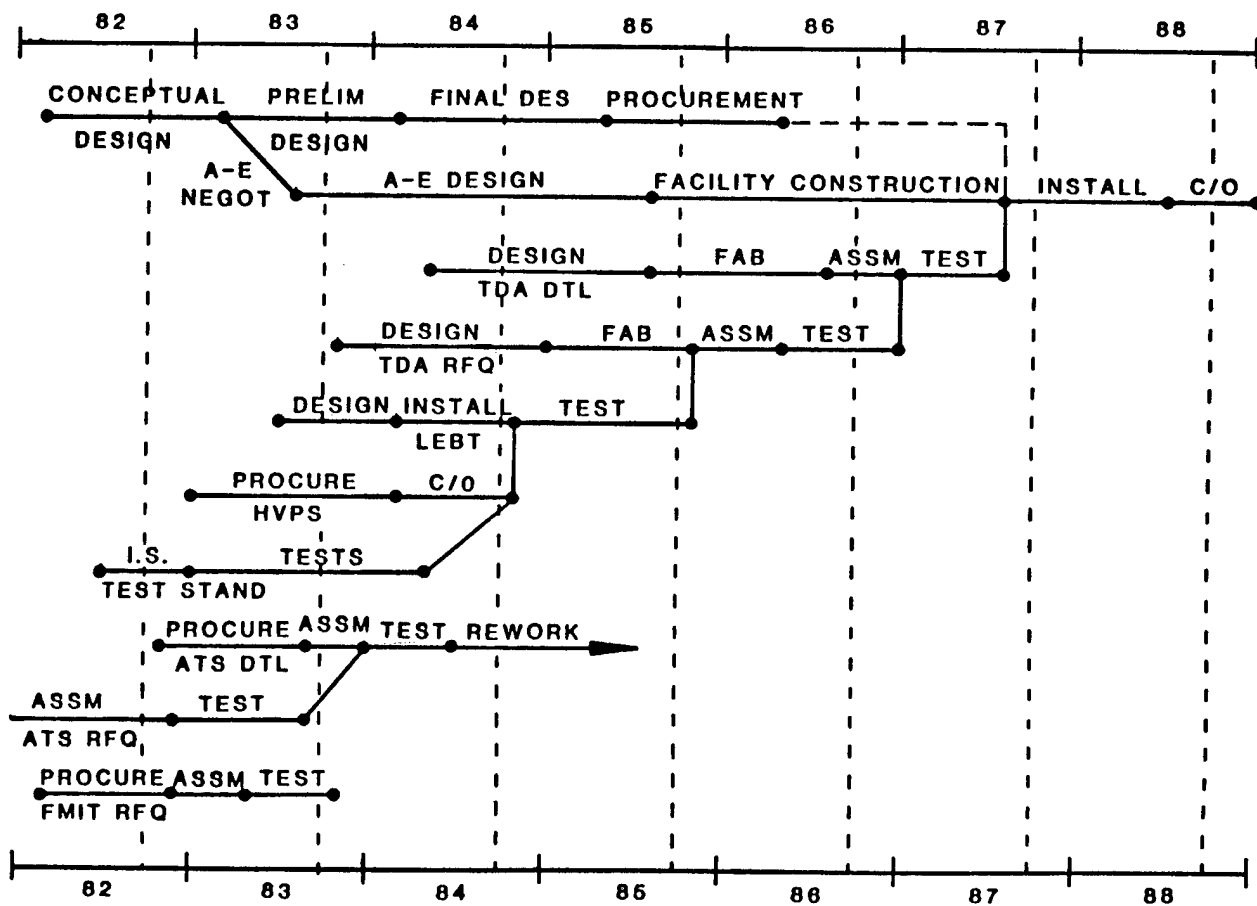
## TECHNOLOGY DEMONSTRATION ACCELERATOR

Several activities were planned for the TDA during 1982. Completion of these tasks was intended to lead to the submission of a proposal for a viable facility.

Early in the program, a proposed facility construction schedule was generated. Data for this schedule were taken from several recent projects of similar scope. It was apparent that if conventional procedures were followed, the construction of the TDA facility could be expected to have a duration of nearly 7 yr from beginning of conceptual design until TDA beam experiments begin. Likely it will be very difficult to decrease this time span because the critical path includes the Architect/Engineer design and facility construction. Failure to pursue aggressively the required supporting R&D could serve to lengthen or delay the schedule. A copy of this very preliminary schedule is included as Fig. 81. Note that this schedule is probably optimistic in that it assumes no manpower or funding limitations.

To initiate facility design, it is imperative that appropriate design criteria be established. To effect this, a workshop was held in mid-March at which the attendees were asked to list their requirements and interests. It was our intent to involve potential users at an early date so that the facility could be designed for maximum use.

The workshop agenda included several presentations of general interest, followed by more specific comments on intended uses of the facility; then, a straw-man design was presented by Los Alamos personnel to suggest a possible design and to stimulate discussion. Additional presentations included reviews on planned rocket experiments, ongoing pointing and tracking experiments, and output optics. One short session was devoted to a discussion of security guidelines for the facility. Late in the second day, the attendees were divided into three working teams with the charter of addressing the items on a workshop questionnaire. At the conclusion of the discussion period, each of the team leaders presented a summary of the group's recommendations. Many attendees also individually filled out questionnaires.



ABBREVIATIONS

PRELIM	Preliminary	C/O	Check out
DES	Design	ASSM	Assembly
A-E	Architect/Engineer	FAB	Fabrication
NEGOT	Negotiation	I.S.	Ion Source

Fig. 81.  
Proposed TDA schedule.

A summary of the workshop presentations and a compilation of the completed questionnaires have been combined into a TDA workshop summary report that has been sent to most of the attendees. A list of facility criteria was generated, with significant input from workshop comments.

Because every facility needs a home, we worked with long-range facilities planners and utilities people at Los Alamos to identify areas at the Los Alamos National Laboratory where the facility could be sited. At least one suitable

site on Two-Mile Mesa has been identified and the long-range planners are now aware of our general needs.

In conjunction with the site identification, we prepared a report and made a presentation to the Laboratory's Construction Projects Review Committee (CPRC). Even though TDA most likely will be funded by DoD, most Laboratory facilities are owned by DOE, and approval by the CPRC is necessary long before any construction may begin. We have been informed very recently that the CPRC has enthusiastically supported the TDA proposal and has recommended to the Laboratory Director that this proposal be given full Laboratory support. The committee did issue a comment that the funding arrangements between DoD and DOE must be better defined before DOE will provide any significant Laboratory support.

Although there are no known fundamental limitations to the assembly and operation of a TDA, substantial development will be required in several areas. As a general comment, the development of greatly improved computer codes seems mandatory to permit the generation and transport of ion beams of the required high quality. Table IX lists the R&D items that we consider essential.

The preconceptual design will include several important areas. Early work will address the expected problems with the RFQ design and will attempt to select an operating frequency. After removal of the RFQ and peak electric-field uncertainties, serious design may begin on the DTL, the rf power system, and detailed facility design.

In conjunction with this preconceptual technical work, a detailed WBS was generated; it will serve as the basis for identifying needed resources and will provide background for costing and schedule generation.

TABLE IX

R&D REQUIRED FOR TDA

Negative ion source development

Injector test stand

Ion extraction

Low-energy beam transport

RFQ matching

RFQ

Improved design codes

Sparking limits

Resolution of fabrication problems

The rf coupling and tuning

Emittance growth

Magnets

Permanent magnets for dipoles and quadrupoles

Solenoid transport

Magnet measurements

Magnet-tailoring techniques

Steering-magnet development

Beam-diagnostics development

The rf power-source development

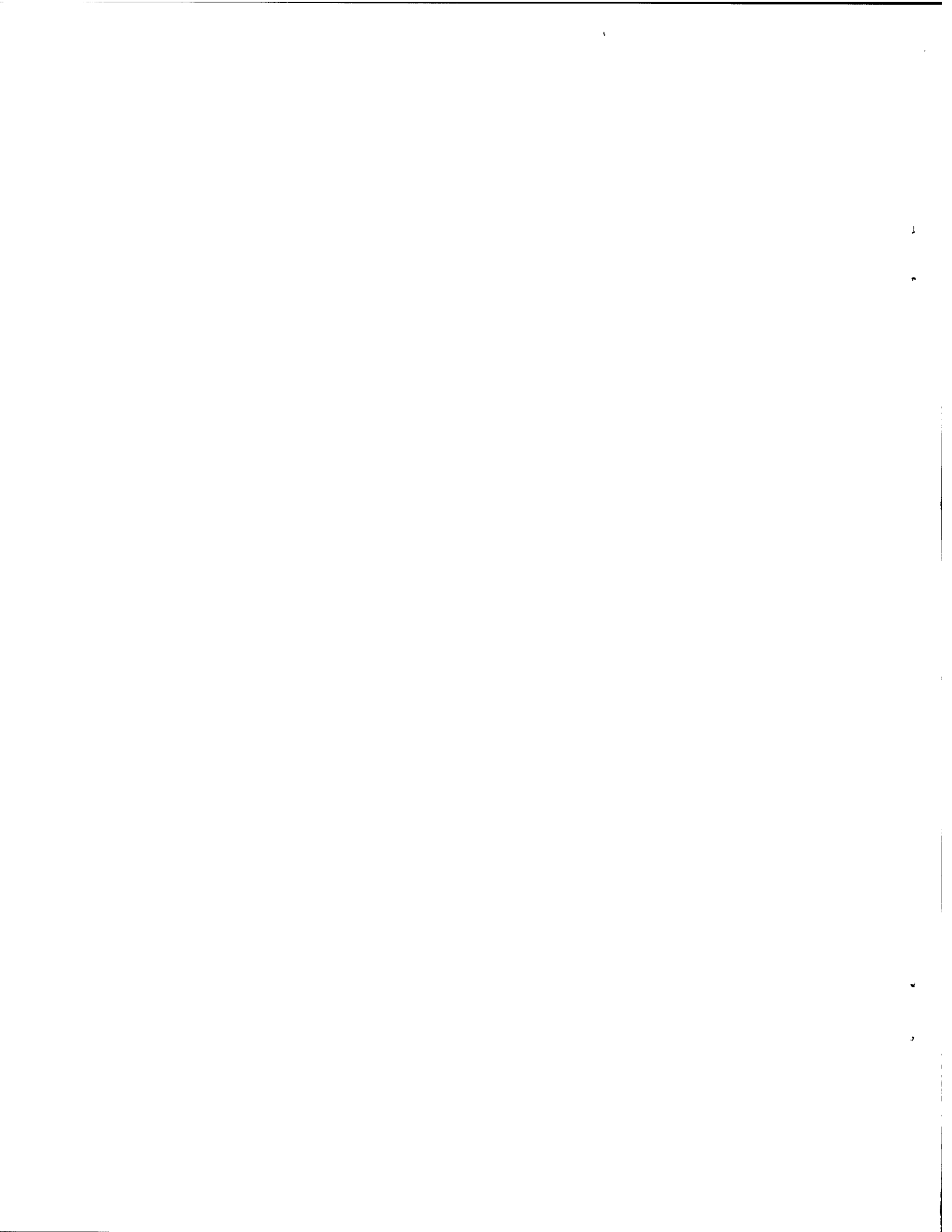
Determination of maximum accelerating gradient

Frequency trade-off studies

Ion-beam-code refinements

## GLOSSARY

ADC	analog digital converter
AT Division	Accelerator Technology Division
ATS	accelerator test stand
CFS	cusped-field source
CMB Division	Chemistry-Materials Science Division
CPRC	Construction Projects Review Committee
DBE	data-base editor
DoD	Department of Defense
DOE	Department of Energy
DTL	drift-tube linac
FMIT	Fusion Materials Irradiation Test
HCTS	high-current test stand
I/O	input/output
ICA	instrumentation, control, and data acquisition
ISTS	ion source test stand
LEBT	low-energy beam transport
M Division	Dynamic Testing Division
MEC Division	Mechanical Fabrication Division
PIGMI	<u>P</u> ion <u>G</u> enerator for <u>M</u> edical <u>I</u> rradiation
PM	permanent magnet
POP	proof-of-principle
RFQ	radio-frequency quadrupole
RIS	rotating ion source
TDA	technology demonstration accelerator
WBS	work-breakdown structure



Printed in the United States of America  
Available from  
National Technical Information Service  
US Department of Commerce  
5285 Port Royal Road  
Springfield, VA 22161

Microfiche (A01)

<u>Page Range</u>	<u>NTIS Price Code</u>						
001-025	A02	151-175	A08	301-325	A14	451-475	A20
026-050	A03	176-200	A09	326-350	A15	476-500	A21
051-075	A04	201-225	A10	351-375	A16	501-525	A22
076-100	A05	226-250	A11	376-400	A17	526-550	A23
101-125	A06	251-275	A12	401-425	A18	551-575	A24
126-150	A07	276-300	A13	426-450	A19	576-600	A25
						601-up*	A99

\*Contact NTIS for a price quote.